La borsa di dottorato è stata finanziata con le risorse del
Programma Operativo Complementare Ricerca e Innovazione 2014-2020,
Azione I.1 "Dottorati Innovativi con caratterizzazione industriale"

UNIONE EUROPEA
Fondo Sociale Europeo

Ministero dell'Università e della Ricerca

Innovative PhD with Industrial Characterization

P.O.C. Research and Innovation 2014-2020

Multimethod study of areas of mining interest: hyperspectral remote and proximal sensing for mineral exploration

Industrial Partner:

AltaMin Limited

External Partners:

CSIRO Mineral Resources

British Geological Survey

Rita Chirico

March 2023

Rita Chirico

UNIVERSITA DEGLI STUDI DI NAPOLI "FEDERICO II"

Department of Earth, Environmental and Resources Sciences

Ph.D. Thesis

XXXV Cycle

Multimethod study of areas of mining interest:

Hyperspectral remote and proximal sensing for mineral exploration

PhD Candidate

Rita Chirico

Tutor:

Prof. Nicola Mondillo

P.hD. Coordinator:

Prof. Rosa Di Maio

Co-tutor:

Prof. Diego Di Martire

Prof. Giuseppina Balassone

Dr. Carsten Laukamp (CSIRO Mineral Resources)

Foreigner Partner Advisor:

Dr. Alessandro Novellino (British Geological Survey)

“Piano piano” resta per me l'eredità che mi lascia e mi educa permettendomi così di saperla sempre più viva di prima.

Abstract

Delineating ore-related hydrothermal alteration zones and supergene caps is fundamental for mineral exploration in remote areas because it gives significant information to identify new mineral concentrations. When outcropping, such large-scale features can be detected through the application of satellite spectral remote sensing techniques. The present study aims to apply a series of innovative technological solutions for the study of areas of mining interest, both historical and newly discovered, combined with commonly adopted mineralogical and geochemical approaches, in order to develop new workflows for identifying mineralized areas (including Critical Raw Materials – CRMs –bearing ones) and characterizing both the ore mineralogy and the hosting country rocks. The study results are useful for targeting the exploration by mapping the alteration assemblages vectoring to the mineralized bodies at local and regional scales, based on their spectral responses in the Visible Near to the Shortwave Infrared (VNIR-SWIR) regions, and defining new exploration prospects which are potentially unknown or unreported so far. The overall strategy of the work included: (1) spectral mineral mapping of alteration patterns through a multi-scale approach, from field-based spectroscopy to spaceborne hyperspectral imaging, and (2) validation through the integration of data from diverse sources, such as mineralogical (XRPD, Optical Microscopy, SEM-EDS) and geochemical analyses. The main goal was to evaluate the capability of the Italian Space Agency (ASI) *Precursore IperSpettrale della Missione Applicativa* (PRISMA) satellite hyperspectral imagery for mineral exploration, by inspecting its performances in mineral mapping. The test sites include genetically different ore deposit types: (1) the Mississippi Valley Type Jabali Zn-Pb(-Ag) deposit in Yemen, (2) the Iron Oxide Copper Gold Marimaca ore and the Río Blanco-Los Bronces copper-molybdenum porphyry district in the northern and central Andes of Chile; (3) the Punta Corna Project in Italy.

Each test area was investigated through the PRISMA satellite hyperspectral images which have a 30m/pixel spatial resolution, a higher spectral resolution compared to multispectral sensors, and cover the mineral-diagnostic wavelength regions (such as

the 2100 nm to 2300 nm range) with a Signal to Noise Ratio (SNR) ≥100. The results for the Jabali Zn-Pb carbonate hosted ore deposit and the Punta Corna Co-Ni vein system were integrated with the use of VNIR-to-SWIR reflectance spectra collected from hand specimens, mineralogical (XRPD), geochemical (ICP-AES/ES/MS) analyses, as well as observation in thin section (Optical Microscopy and SEM-EDS microanalysis) on rock samples collected in the test areas, with the aim of validating the remote sensing-based results.

The study of the Zn-Pb Jabali deposit was aimed to apply a multi-scale workflow based on hyperspectral data to delineate hydrothermal dolomitization and supergene alteration associated with the Mississippi Valley-Type Zn-Pb(-Ag) deposit of Jabali (Western Yemen). We adopted a combined use of remote and proximal sources of hyperspectral data for defining features possibly able to target carbonate-hosted Zn-Pb ore deposits. The VNIR-SWIR reflectance spectra derived from the laboratory-based and PRISMA satellite data, that were interpreted with the support of analyses on ground samples (XRPD-QPA and ICP-MS/ES), allowed us to (1) delineate the distribution of the dolomitization in the Jabali area, and (2) identify the gossan outcrops overlying the mineralized areas. Spectral mineral maps were produced through the band ratios method using a combination of specific feature extraction indexes. The dolomites' footprint was mapped using a PRISMA Level 2C image, by enhancing the spectral differences between limestones and dolomites in the SWIR-2 region (major features centered at 2340 nm and 2320 nm, respectively). Gossans were detected due to the Fe^{3+} absorption band in the VNIR region at 900 nm (Crystal Field Absorption - CFA). The Zn-Pb mineralized area, extended for approximately 25 km^2, was thus identified by recognizing gossan occurrences in dolomites. The detailed evaluation of the reflectance spectra from mineralized samples, even if their distribution mapping is not achievable at the satellite spatial resolution, helped the definition of the spectral responses of Zn(-Pb)-bearing oxidation-related minerals. Since they are commonly associated with nonsulfide ores related to supergene alteration of sulfide ore bodies, they represent a useful tool for exploration surveys based on field spectroscopy. The results of this study illustrate the advantages of using feature extraction indexes applied to hyperspectral data for the recognition of

outcropping geology, which can be used as a powerful tool for mineral exploration in sedimentary environments at regional scale.

The purpose of the study concerning the application of both remote and proximal sensing to the study of the area of the Punta Corna Mining Complex (PCMC) was aimed to highlight the distribution of alteration minerals genetically related to hydrothermally driven metallogenetic processes occurred. The results are meant to be used as support for mineral exploration in the area. The PCMC is a brownfield exploration prospect owned by AltaMin Ltd., located in the Servin Valley in the Western Alps (Piedmont, Italy). It is characterized by hydrothermal polymetallic orebodies defined by zoned Fe^{2+}-rich carbonates and Co-Ni sulfide mineralization, hosted by E–W-trending sub-vertical post-metamorphic veins with a maximum thickness of 6–7 m. Laboratory hyperspectral IR spectroscopy and mineralogical (XRPD) and geochemical (ICP-AES/MS) analyses were carried out to define target alteration minerals and to validate the results obtained from the processing of satellite images. The heavily sericitized analyzed samples were characterized by the application of the 2200 nm feature intensity and wavelength indexes, as well as the Fe-oxy-hydroxides-bearing samples. The first ones are characterized by higher contents of Al-rich white mica, which directly alters albite. White mica can occur in close relationship with chlorite, where the latter seems to partially replace Ca-amphibole crystals. Fe(±As)-hydroxides are also present, forming concretions either surrounding white mica crystals or in the interstices between them. The results obtained for the metabasite country rock, both the spectral characterization and mineralogical-geochemical analysis, show that it is affected by intense sericite–quartz-carbonate alteration only in the immediate proximity of the ore-bearing veins. However, areas showing enrichments in Mg-rich chlorite abundances (semi-quantitative XRPD) are in spatial relationship with the known outcropping veins. This is displayed as a more prominent 2250 nm absorptions feature in the spectral dataset and it is associated also with higher bulk Al_2O_3 concentrations, suggesting a potential chloritization occurred at regional scale. The delineation of the alteration at the km scale was based on the mapping of mineral occurrences in terms of relative abundances using feature extraction spectral indexes applied to PRISMA

hyperspectral satellite. The heavy sericitization and the supergene contribution observed at hand specimens scale were mapped by means of satellite images, highlighting the presence of an alteration halo surrounding the main veins known in the area, as well as in zones where the mineralization occurrences, either reported in the literature or observed in the field, are still poorly known. The results of the study, partly validated through fieldwork, assess that a combined and multi-scale approach based on hyperspectral data represents an effective method for mapping alteration minerals associated with the Co-Ni mineralization, i.e., white mica, chlorite, and supergene goethite, by means of their diagnostic absorption features at around 2200 nm, 2250 nm, and 900 nm, respectively. The method can be used as an additional tool for guiding toward prospective areas where Co-Ni-bearing veins occur.

The objectives of the application of PRISMA hyperspectral imagery for the study of the areas centered on the "Marimaca Copper Project", in the Naguayán district in the Antofagasta Province, and the Río Blanco-Los Bronces copper-molybdenum porphyry district, in the Santiago Region of Chile were to identify and map minerals associated with the surface-exposed hydrothermal (sericitic, propylitic, advanced argillic) and supergene (leached caps) alteration zonation patterns related to Cu deposits in the Chilean Andes and widely affecting the rocks hosting the mineralization. The Naguayán district area is a well-known host for several copper, iron, and minor gold, silver, and zinc ore bodies of Late Jurassic to Early Cretaceous age. The Río Blanco-Los Bronces district is the host for several world-class copper-molybdenum porphyry systems, hosted in Late Miocene – Early Pliocene magmatic arc.

To map the relative abundances and compositions of specific supergene and hydrothermal alteration minerals such as Fe-oxides and hydroxides (hematite-goethite), di- and tri-octahedral phyllosilicates (e.g., micas-kaolinite-chlorite), hydroxyl-bearing sulfates (e.g., alunite) and epidote, a range of band ratios in the region around 900 nm, from 1480 nm to 1770 nm, and from 2100 nm to 2300 nm, were applied to PRISMA satellite imagery aimed at diagnostic absorption feature extraction and characterization. The results of this study show a close spatial relationship between the distribution of sulfates (alunite), Al-rich to Al-poor white

micas, and chlorite-epidote, as well as the Fe-bearing minerals associated with the supergene alteration, from proximal to distal to known Cu-deposits, supporting a causative association with the magmatic-hydrothermal activity-related alteration. The work supports the use of spaceborne hyperspectral imaging spectroscopy for assisting mineral exploration for other copper deposits worldwide, providing targeting information for follow-up sampling and surveys, which could improve the exploration strategies.

The study regarding the characterization of the area affected by the collapse of the tailing "Dam B1" of the Córrego do Feijão Mine (Brumadinho, Brazil) aimed to map the land area affected by the flood and the related environmental effects over time by using multispectral satellite images. The collapse of the tailing "Dam B1", which occurred in January 2019, is considered a large socio-environmental flood disaster, counting numerous people died and seriously affecting the local flora and fauna, as well as agricultural areas along the Paraopeba River. To pursue the aim, Level-2A multispectral images from the European Space Agency (ESA)'s Sentinel-2 sensor were acquired before and after the tailing dam collapse in the period 2019-2021. The pre- and post-failure event analysis allowed evidencing drastic changes in the vegetation rate, as well as in soils and surficial waters, based on the spectral signatures of the minerals composing the mining products, mainly Fe-oxides, i.e., hematite, characterized by the Crystal Field Absorption – CFA – feature at around 842 nm (in band 8 and 8A of Sentinel-2). By combining the information obtained with the study mentioned above, a work focused on the South-West Sardinia, one of the oldest mining districts in the world, and the Quadrilátero Ferrífero mining district was conducted, with the purpose of segmenting relevant imagery classes, for the automatic detection of mining areas using hyperspectral images of the PRISMA mission. The method is focused on a deep learning model - U-Net convolutional neural network. In order to avoid the typical problem of hyperspectral data redundancy and to improve the computational performances without losing accuracy, the Singular Value Decomposition (SVD) is applied to the hyperspectral data cube, taking only the first three singular values, thus projecting the multi-dimensional data cube to a three channels image. The two areas were analyzed to test the

transferability of the model to other mining areas worldwide. These techniques open the possibility for quickly classifying areas affected by floods, as well as obtaining significant information potentially useful for monitoring and planning the reclamation and restoration activities in similar cases worldwide, representing additional tools for evaluating the environmental issues related to mining operations in large areas at high temporal resolution.

To conclude, the PRISMA imagery evaluated in this Thesis demonstrates the capability of hyperspectral satellite data for mineral exploration and its advantage over previous hyperspectral and multispectral satellite sensors as regards accurate mineral mapping, which is a key factor for successful mineral exploration. However, additional studies are required to improve advanced machine learning techniques for dealing with spatial resolution problems of hyperspectral satellite imagery, while keeping constant the high spectral resolution and SNR, as well as data noise and sensor artifacts management, all impacting the quality of the mapping results. Moreover, the detailed evaluation of the reflectance spectra from both alteration and supergene mineralized samples commonly associated with the hypogene ore bodies, even if their distribution mapping is not achievable at the satellite spatial resolution, can help their definition in the field and represent a useful tool for exploration surveys based on ground-based hyperspectral analyses.

Chapter 1:

Introduction and aims

The growing concern about the "green transition" and Critical Raw Materials (CRMs) supply within the European Union and across the globe, as well as the rising metal demands for high-tech products and emerging innovations, combined with decreasing ore grades, have resulted in several initiatives and strategies that have been implemented to secure and improve access to raw materials (European Commission, 2018, 2020). In this scenario, there is a revival of interest in improving the state of knowledge on old mining sites where the CRMs' economic potential was not fully investigated, strengthening the sustainable and responsible Europe's domestic sourcing and processing of Co and Ni ore deposits (e.g., The Punta Corna Mining Complex, investigated in this Thesis). Moreover, the proposed actions also regard the implementation of additional cost-effective and time-saving tools and workflows for mineral exploration and efficient and less impacting extraction of CRMs from primary ores. The latter also include the deployment of Earth-observation programs and remote sensing for resource exploration (European Commission, 2020).

It is well known that a good understanding of deposit mineralogy and its heterogeneity has implications across the entire mineral value chain: from the exploration and project development stages to resource definition, production, and remediation phases. A good understanding of deposits mineralogy can be used as a tool for the detection and characterization of mineral alteration vectoring to ore concentrations and can support resource estimation and alteration modeling, as well as metallurgical, geotechnical, and waste rock characterization. A detailed understanding of ore mineralogy, therefore, makes a strong contribution to de-risking exploration projects and supporting more sustainable decisions.

Innovative technological solutions are constantly modifying the traditional mining industry and processing chain. Novel, faster, and less expensive methods for the characterization of both ore and alteration mineralogy are increasingly being applied. The latter include the Infrared (IR) Reflectance Spectroscopy technologies at

different scales of observation, from field-based to spaceborne imaging sensors. Several rock-forming and alteration minerals show diagnostic spectral absorptions in the Visible near IR (VNIR) to the Shortwave IR (SWIR) wavelength ranges (from 400 to 2600 nm). These wavelength ranges are suitable for geological spectral sensing applications as they provide mineralogical and geochemical information due to electronic transitions and vibrational processes in minerals (Clark et al., 1990). Characteristic spectral features can be used for defining the occurrence and relative abundance of mineral species and their physicochemical variations (Laukamp et al., 2021).

With particular reference to spectral remote sensing technology, it represents a tool that has been well-established in applied geology for over four decades (Bedini, 2017; Peyghambari and Zhang, 2021; and reference therein). The main aim of spectral sensing is to detect and quantitatively measure the earth's surface materials by using calibrated reflectance spectra acquired as images in hundreds of narrow and contiguous spectral bands, in most of the cases ranging from the VNIR (400 to 1300 nm) to SWIR (1300 to 2600 nm) regions of the electromagnetic spectrum (van der Meer et al., 2012). Since its advent, geological remote sensing has been used as a tool for the exploration of mineral deposits. Even though spectral remote sensing has been applied to the study and exploration of several ore deposit types through different scales of observation (e.g., Lampinen et al. 2017; Bedini 2017; Laukamp et al. 2022, and references therein), its potential remains still underexplored for the investigation of several ore minerals of notable economic importance, including, for instance, the Mississippi Valley Type base metal deposits (Chirico et al., 2023). At the same time, more advanced satellites are launched ever more frequently, making the available spectral data increasingly detailed in both the spatial and the spectral resolution (i.e., hyperspectral systems are characterized by a higher number of channels compared to multispectral sensors; Peyghambari and Zhang, 2021).

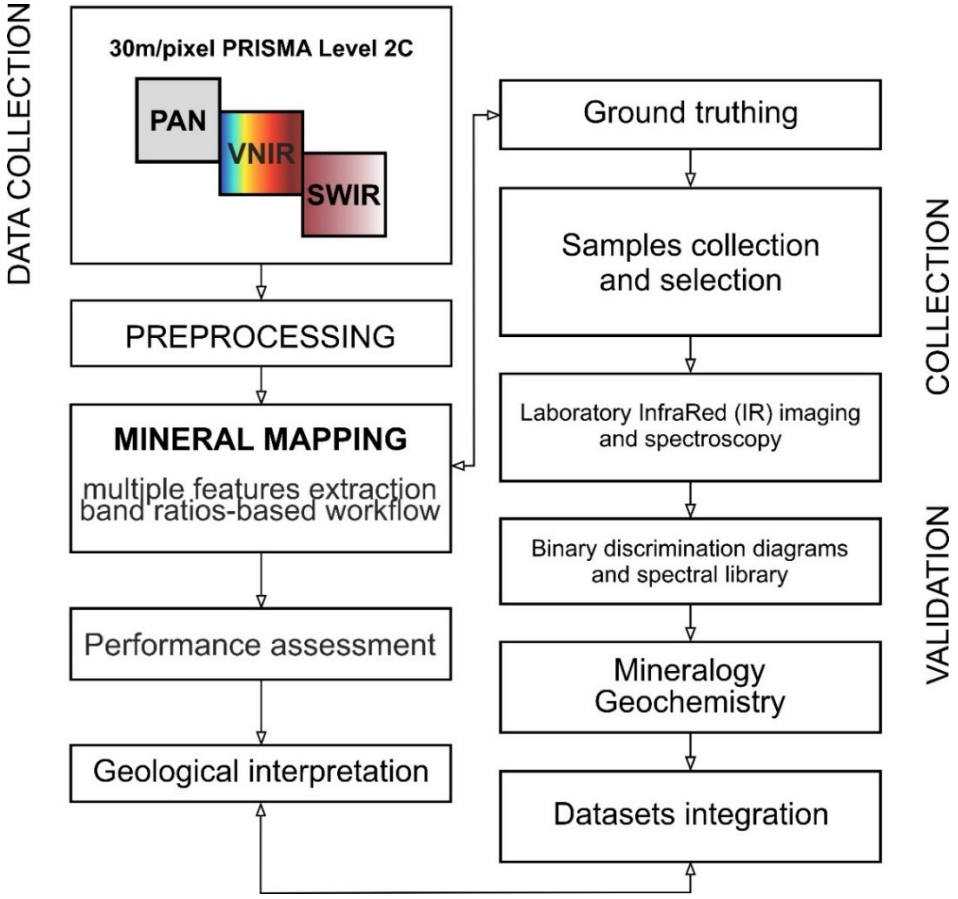

Fig. 1.1 Schematic multi-scale workflow used in this Thesis.

This PhD research project aims to apply a series of innovative technological solutions for the study of areas of mining interest, both historical and newly discovered, combined with commonly adopted mineralogical and geochemical approaches, in order to develop new workflows for identifying mineralized areas (including CRMs-bearing ones) and characterize both the ore mineralogy and the hosting country rocks. The study results are useful for targeting the exploration by mapping the alteration assemblages vectoring to the mineralized bodies at the local and regional scales and defining new exploration prospects which are potentially unknown or unreported so far. To achieve the project objectives, the overall strategy followed during the PhD included: (1) spectral mineral mapping of alteration patterns through a multi-scale approach, from field-based and laboratory-level spectroscopy to spaceborne hyperspectral imaging, and (2) validation through the integration of data from diverse sources, such as mineralogical (XRPD, Optical Microscopy, SEM-

EDS) and geochemical analyses (Fig. 1.1). The main goal was to evaluate the capability of the Italian Space Agency (ASI) *Precursore IperSpettrale della Missione Applicativa* (PRISMA) satellite hyperspectral imagery for mineral exploration, by inspecting its performances for mineral mapping. In addition, both multispectral and hyperspectral satellite imagery was used for the environmental monitoring of mining areas.

To pursue the aims of this study, a wide range of test areas were selected (Fig. 1.2): (1) the Mississippi Valley Type Jabali Zn-Pb(-Ag) deposit in Yemen, (2) the brownfield Co-Ni Punta Corna Project in Northern Italy, which is owned by AltaMin Limited mining company, that is the industrial partner of my PhD research, (3) the Iron Oxide Copper Gold Marimaca ore in the Coastal Cordillera of Northern Chile and the Porphyry Cu-Mo Río Blanco-Los Bronces district in Central Chile. Moreover, the Brumadinho (Minas Gerais, Brazil) and the South-West Sardinia Mining Districts were considered for remote sensing-based mineral mapping for environmental monitoring purposes.

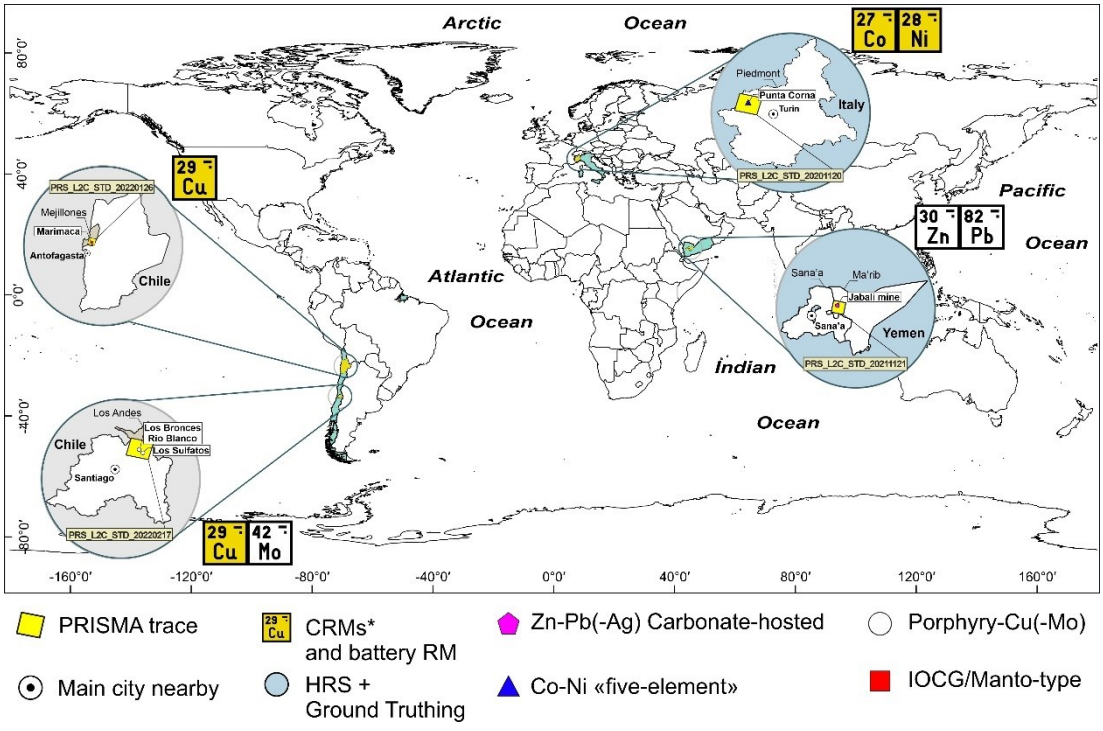

Fig. 1.2 Location and deposit types of the case studies. CRMs: Critical Raw Materials; HRS: Hyperspectral Remote Sensing.

The deposit types chosen as test sites are the hosts for metals like Cobalt (Co), Nickel (Ni), Copper (Cu), as well as base metals, being potential sources of CRMs. The latter are considered key commodities in a wide range of industrial and strategic technologically innovative applications and their demand is expected to increase dramatically by 2050 (Hund et al., 2020). For instance, Co is included in the European Union CRMs list (Blengini et al., 2017, European Commission, 2020); the most important use of Co is for lithium (Li)-ion battery production, and is widely employed in the automotive (especially for Electric Vehicles), aeronautic, and naval sectors. Even if Co and Li are the best-known metals used for energy storage, the overall increasing demand for minerals used in a wide range of energy technologies and industrial applications also includes metals like Ni (Ni alloys) and "cross-cutting" metals like Cu, Mo, and Zn (Hund et al., 2020), which are also needed for alloys to be used in the manufacture of tools used in other industrial applications, for instance, power generation facilities, in petroleum refineries, jet engines, etc. (USGS, 2020).

Thesis outline

The first part of this Thesis provides a basic overview of reflectance spectroscopy (Chapter 2) and Earth Observation (EO) remote sensing techniques (Chapter 3). Chapter 4 focuses on Optical Satellite Remote Sensing (hyperspectral and multispectral), including the most used Satellite Remote Sensing data and details on the technical specifications and applications of the PRISMA hyperspectral satellite mission so far. The selected study cases and the detailed description of the methods used for the investigation of each one of them are reported in the respective Chapters 5 to 9.

Respectively, Chapter 5 reports the results obtained for the Zn-Pb Jabali mining district. It focuses on delineating hydrothermal alteration and supergene caps for mineral exploration of base metals sulfide ores, by combining both satellite hyperspectral remote sensing and spectral characterization of ore minerals and the hosting country rocks. Chapter 6 reports on a mineralogical, geochemical, and spectral study of alteration minerals (related to sericitization and potential

chloritization) genetically associated with hydrothermally driven metallogenetic processes of Co-Ni vein-hosted ores. Chapter 7 concerns the application of satellite remote sensing for the distribution and compositional mapping of minerals associated with the surface-exposed hydrothermal (sericitic, propylitic, advanced argillic) and supergene (leached caps) alteration assemblages related to Cu deposits in the Chilean Andes. Chapters 8 and 9, instead, deal with the application of both satellite multispectral and hyperspectral imagery for the environmental monitoring of mining areas. Chapter 8 mainly focuses on the mapping of land areas affected by the flood related to the collapse of a tailing dam in the Brumadinho Mining District (Minas Gerais, Brazil). Chapter 9, instead, reports the results of a project conducted in collaboration with the Department of Physics of the University of Naples Federico II, aimed to pursue the automatic detection of mining areas within large areas using spaceborne hyperspectral image data, using deep learning model - U-Net convolutional neural network, in order to provide valuable information useful in planning reclamation and restoration activities.

The discussion is focused on the comparison between the investigated deposits and the PRISMA capabilities in mineral mapping.

Several parts of this PhD thesis correspond to the content of the following papers, either published, in press, or in preparation:

- **Chapter 5: Mapping hydrothermal and supergene alteration zones associated with carbonate-hosted Zn-Pb deposits by using an integrated approach of mineralogical, geochemical, field-based and satellite hyperspectral methods.** Published in "Ore Geology Reviews"

Reference: **Chirico, R.**, Mondillo, N., Laukamp, C., Mormone, A., Di Martire, D., Novellino, A., & Balassone, G. (2023). Mapping hydrothermal and supergene alteration zones associated with carbonate-hosted Zn-Pb deposits by using PRISMA satellite imagery supported by field-based hyperspectral data, mineralogical and geochemical analysis. Ore Geology Reviews, 105244. DOI: https://doi.org/10.1016/j.oregeorev.2022.105244

Contributions of R. Chirico to the paper: formal analysis, spectral, geochemical, and mineralogical data curation and interpretation, Software, Visualization, and Validation. R. Chirico implemented the conceptualization of the paper and carried out the writing of the first version of the manuscript, which was then reviewed, supervised, and approved by co-authors.

- Chapter 6: The use of Hyperspectral Remote and Proximal Sensing for Mineral Exploration in Italy: the Punta Corna Co-Ni vein system (Piedmont, Italy).

Reference: **Chirico, R.***, Laukamp, C., Mondillo, N. – in prep.

Contributions of R. Chirico to the paper: formal analysis, spectral, geochemical, and mineralogical data curation and interpretation, Software, Visualization, and Validation. R. Chirico implemented the conceptualization of the paper and carried out the writing of the first version of the manuscript, which was then reviewed, supervised, and approved by co-authors.

- Chapter 7: The application of PRISMA hyperspectral satellite imagery for mapping distinct hydrothermal alteration zones in the Chilean Andes: the Marimaca IOCG and the Río Blanco-Los Bronces Cu-Mo porphyry districts.

Reference: Sorrentino, A., **Chirico, R.***, Corrado, F., Laukamp, C., Di Martire, D., and Mondillo N. – in prep.

Contributions of R. Chirico to the paper: formal analysis, spectral data curation and interpretation, Software, Visualization, and Validation. R. Chirico will be the corresponding author of the paper. She implemented the paper conceptualization and made the greatest contribution to the writing of the first version of the manuscript, which was then reviewed, supervised, and approved by co-authors.

- Chapter 8: **Application of Multispectral Remote Sensing for Mapping Flood-Affected Zones in the Brumadinho Mining District (Minas Gerais, Brazil).** Published in “Remote Sensing”.

Reference: Ammirati, L., **Chirico, R.***, Di Martire, D., & Mondillo, N. (2022). Application of Multispectral Remote Sensing for Mapping Flood-Affected Zones in the Brumadinho Mining District (Minas Gerais, Brazil). Remote Sensing, 14(6), 1501.

Contributions of R. Chirico to the paper: conceptualization, validation. R. Chirico is the corresponding author of the paper. She collaborated on the paper conceptualization and method validation, as well as participated in the writing of the first version of the manuscript, which was then reviewed, supervised, and approved by co-authors.

- **Chapter 9**: **PRISMA Hyperspectral Image Segmentation with U-Net Convolutional Neural Network using Singular Value Decomposition for Mapping Mining Areas: preliminary results.** Conference paper to be published in Applied Intelligence and Informatics (Springer).

Reference: Dosi, A., Pesce, M., Di Nardo, A., Pafundi, V., **Chirico, R.**, Ammirati, L., Delli Veneri, M., Mondillo, N., Longo, G. (2023). PRISMA Hyperspectral Image Segmentation with U-Net Convolutional Neural Network using Singular Value Decomposition for Mapping Mining Areas. Applied Intelligence and Informatics - Springer | Second International Conference, AII 2022, Reggio Calabria, Italy proceedings. (In press).

Contribution of R. Chirico to the paper: training dataset collection and validation of the results based on geological and mineralogical knowledge. R. Chirico participated in the writing of the first version of the manuscript, which was then reviewed, supervised, and approved by co-authors.

The currently available version of the Thesis is only partial and does not include the entire content. The complete version of the Thesis will be available only one year after the initial publication date due to an embargo (i.e., a period of time during which access to the full Thesis content is limited).

Chapter 2:

Fundamentals of Infrared (IR) Reflectance Spectroscopy for geological applications

2.1 Introduction

Infrared (IR) reflectance spectroscopy is an analytical methodology based on the interaction between electromagnetic radiation and the matter in the IR region. It is referred as vibrational spectroscopy since it is based on energy variations between different vibrational levels of molecules induced by their interaction with the IR radiation. The IR radiation comprehends the portion of the electromagnetic spectrum between the Visible and the Microwaves (Fig. 2.1).

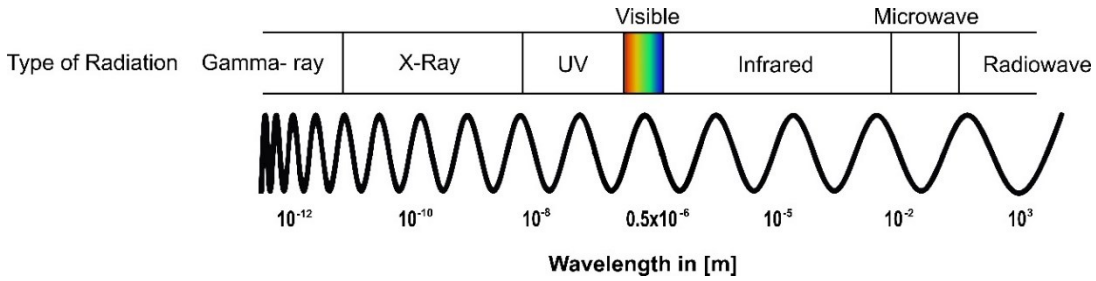

Fig. 2.1 The electromagnetic spectrum and characteristic wavelengths.

The theoretical and technical aspects of IR spectroscopy are treated in detail in the scientific literature in numerous specialized texts (Wokaun, 1996; Griffiths and Chalmers, 2002; Stuart, 2004; Henderson et al., 2014, and references therein), to which I suggest referring for in-depth study of the technique. However, some fundamental notions useful for understanding the theoretical basis of the method proposed in this Thesis are reported as follows.

In simple terms, when the IR radiation interacts with a molecule, it can be absorbed, reflected, or diffused. The IR spectroscopy is based on the former process: the energy released by the radiation is absorbed and converted into vibrational energy. As a result, molecules and atomic groups in minerals can vibrate in different modes when interacting with the IR electromagnetic radiation.

Depending on the type of molecular deformation occurring during vibration, the main normal vibrational modes of interest can be classified in (Fig. 2.2):

- *stretching* - stretching and contraction along the axis of the bond (abbreviated as ν)
- *bending* - a variation of the bond angle (abbreviated as δ)

In turn, they can be distinguished as symmetrical or asymmetrical (commonly abbreviated as ν_s/δ_s or ν_{as}/δ_{as}) with respect to the symmetry of the molecule and therefore, with respect to the plane which contains the bond angle (Balassone and Bellatreccia., 2019).

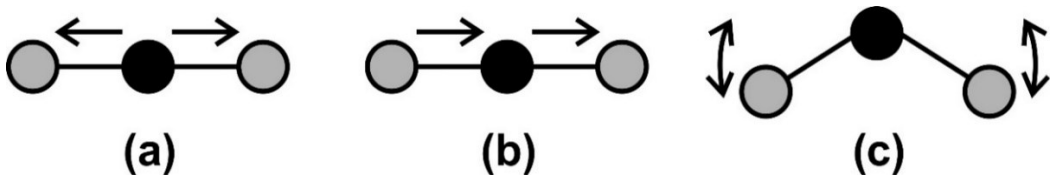

Fig. 2.2 Normal vibrational modes for linear triatomic molecules. (a) symmetrical and (b) asymmetrical stretching; and (c) bending.

Based on the molecules and bonds present, the energy is absorbed at diagnostic wavelengths (Fig. 2.3). The resulting spectra (i.e., the full arrangement of absorption features) measured from geological materials, including rocks and soils, from a wide range of commonly used spectral proximal and remote sensing instruments, can be defined as spectral signatures or "fingerprints" of the minerals and the other components within them (Fig. 2.3). Spectral absorption signatures can be linked to specific physicochemical properties of the minerals investigated, from which information like mineral species and groups, relative abundance, chemistry, and crystallinity can be obtained.

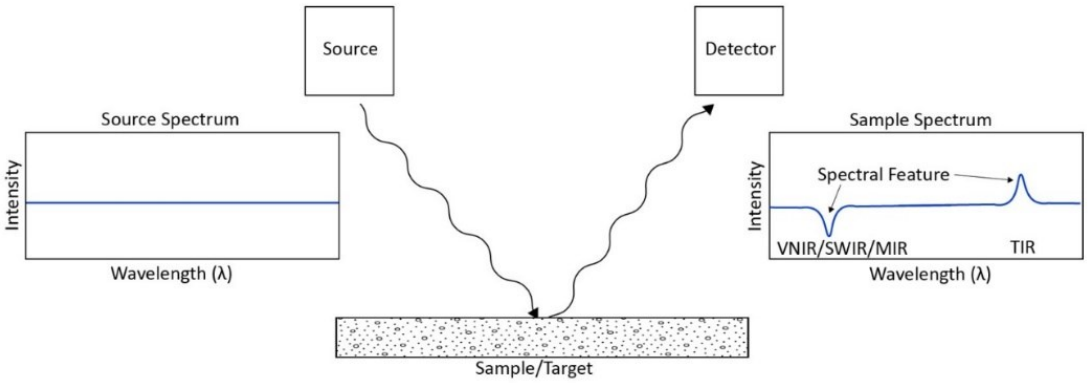

Fig. 2.3 Simplified scheme of the IR Reflectance spectroscopy concept (image credits: Stromberg J. – CSIRO Mineral Resources)

Several mineral species and groups can produce diagnostic absorption features over the Visible and IR portion of the electromagnetic spectrum. The IR region of the spectrum can in turn be classified based on the clusters of vibrational modes associated with the physicochemical properties of minerals (Fig. 2.4; from Laukamp et al., 2021):

- The Visible Near IR (VNIR): between 325 and 1300 nm
- The Shortwave IR (SWIR): between 1300 and 2600 nm, which can be in turn divided into SWIR 1 (1300 to 1850 nm) and SWIR 2 (1850 to 2600 nm)
- Middle IR (MIR): between 2600 and 5500 nm
- The Thermal IR (TIR): between 5500 and 15000 nm

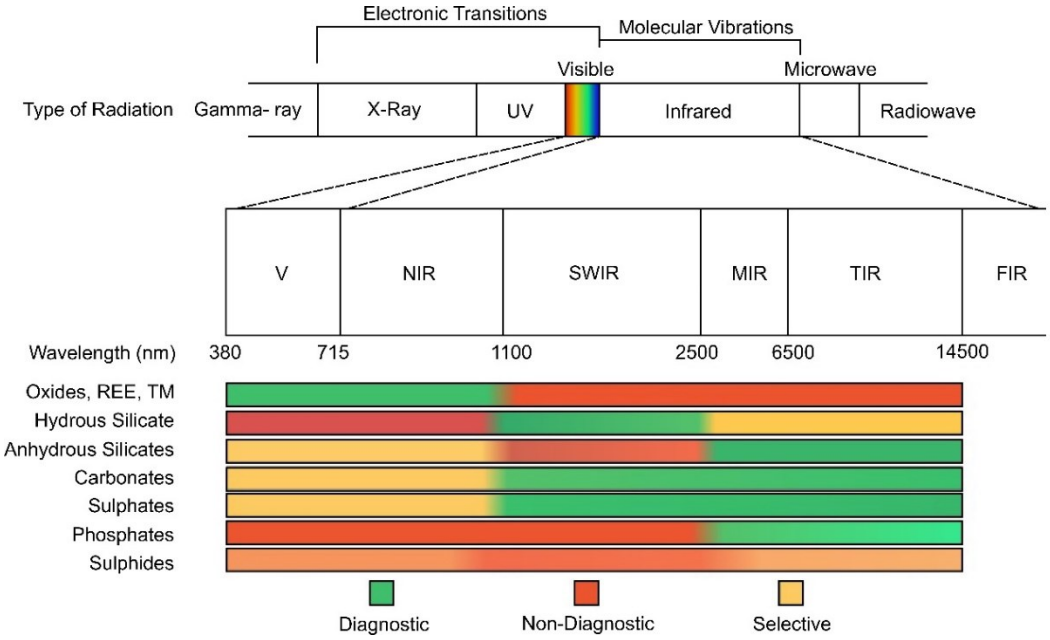

Fig. 2.4 Geologically relevant spectral regions and the respective mineral groups that can be investigated (image modified from Stromberg J. – CSIRO Mineral Resources)

2.2 Diagnostic spectral features of rock-forming and alteration minerals

Both electronic and vibrational processes at the base of the spectral properties of IR-active rock-forming minerals (Figs. 2.4 and 2.5) have been comprehensively studied by several authors (Hunt, 1971; Hunt and Salisbury, 1971; Gaffey, 1985, 1986; Crowley, 1986; Clark et al., 1990; Burns, 1993; van der Meer, 1995; Kurz et al., 2012; Zaini et al., 2012; Green and Schodlok, 2016; Laukamp et al., 2021). They are summarized below and within the specific Chapters (from Chapters 5 to 8) of this Thesis dealing with the specific case study analyzed.

The VNIR region of the electromagnetic spectrum is characterized by significant absorption bands caused by electronic modes involving mainly the transfer of electrons of transition metals from lower to higher energy levels (i.e., CFA – Crystal Field Absorption) or the bonded ligands to the cation (i.e., CTS – Charge Transfer), for instance, oxygen (e.g., hematite α-Fe_2O_3) or oxygen and hydroxyl (e.g., goethite – α-FeO(OH)) (Hunt and Ashley, 1979; Sherman and Waite, 1985; Burns, 1993; Cudahy and Ramanaidou, 1997).

Vibrational modes of mineral phases which contain different oxygen species can be observed in different domains of the SWIR to TIR wavelength regions (for instance, quartz (SiO_2), albite ($NaAlSi_3O_8$), kaolinite ($Al_2O_32SiO_2 \cdot H_2O$), dolomite ($CaMg(CO_3)_2$) and hematite (Fe_2O_3), Fig. 2.5).

The main types of vibrational modes (i.e., infrared-active functional groups) in these rock-forming and alteration minerals are due to fundamental stretching and bending vibrations (ν and δ, respectively) of O-H, N-H, C-O, B-O, S-O, P-O and Si-O bonds (Laukamp et al., 2021; Moenke, 1974), and their overtones (abbreviated, for example, as 2ν for the first overtone of a stretching fundamental) and combinations of fundamental stretching and bending vibrations (ν + δ).

The SWIR 1 wavelength range active functional groups are dominated by the first overtones of hydroxyl-related stretching fundamentals (2νOH). Two main processes cause the mineral-related absorption features in the SWIR 2 range (Laukamp et al., 2021): (1) combinations (ν + δOH) of hydroxyl-related fundamental stretching (νOH) and bending vibrations (δOH), and (2) combinations (e.g., 2ν3 + ν1 CO_3) or overtones (e.g., 3ν3CO3) of carbonate-related fundamental stretching vibrations.

The MIR wavelength region, instead, comprises the fundamental stretching vibrations of O-H bonds (νOH), which occur in hydroxylated mineral groups (e.g., di- and tri-octahedral sheet silicates, like micas, smectites, kaolin group, chlorite; amphiboles, tourmalines, and metal oxides/hydroxides, like gibbsite, goethite).

The TIR range represents the largest wavelength region of IR active functional groups. It is defined by combinations of many fundamental vibrational modes, including Si-O-related vibrational modes as well as other important TIR-active anions (e.g., BO_3^{3-}, CO_3^{2-}, SO_4^{2-}, PO_4^{3-}) and hydroxyl-related stretching fundamentals.

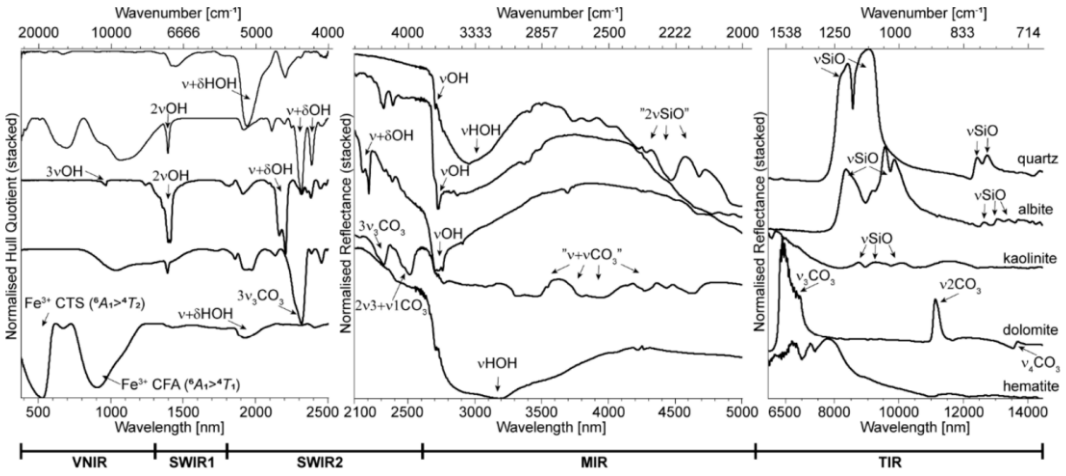

Fig. 2.5 Spectral signatures of the major rock-forming minerals from the VNIR to the TIR wavelength range (from Laukamp et al., 2021)

In this frame, some consideration regarding the physicochemical properties described by each spectral absorption feature can be made, which are useful for interpreting and describing the mineral phases and their compositional variations. The spectral mineralogy can provide insights into (1) the presence/absence of minerals; (2) mineral (cation) composition; (3) relative mineral abundances; (4) crystallinity; (5) water content, as well as (5) grain size and orientation.

Since the relative intensity of a given absorption feature increases with the relative abundance of the respective bond causing the vibrational mode, the absorption band depth (relative to the background continuum) can be assumed to be proportional to the mineral's relative abundance (Clark et al., 1990). It must be underlined that the latter represents a simplistic assumption, since the correlation between the relative intensity and the amount of the related vibrational mode is not necessarily linear, as it depends on several parameters, such as the packing fraction, the intrinsic index of refraction and the absorption coefficient of the particulate medium, as well as the scattering coefficient of the particulate medium and the average grain size (Laukamp et al., 2021; Vincent and Hunt, 1968).

The wavelength position of the spectral features in the SWIR to TIR is associated with the chemical composition of a given mineral (Vedder and McDonald, 1963). It follows that displacements of the absorption feature to either longer or shorter

wavelengths can highlight either mineral compositional variations or mineral mixing. While the Full Width at Half Minimum or Maximum (FWHM) of an absorption feature increases with decreasing crystallinity of minerals, as the bond lengths vary more in poorly ordered crystal structures (e.g., applicable for the characterization of kaolin group minerals; Murray and Lyons, 1955).

Chapter 3:

Remote Sensing for Earth Observation (EO)

3.1 Introduction to satellite-based remote sensing

Remote sensing is the procedure of acquiring, processing, and interpreting images and associated data that record the interaction between objects and electromagnetic energy (Bedini, 2017; Sabins, 1999), and therefore, it allows to obtain information about objects on the Earth's surface without coming into direct contact with them (Pettorelli et al., 2014).

A remote sensor is an instrument that detects electromagnetic energy, quantifies it, and usually records it, in an analogic or digital way. Remote sensors used in Earth Observation (EO) can be operated either at a small distance above the ground (ground-based), using field instruments, or mounted on aircraft (air-borne), as well as far beyond the atmosphere on satellite platforms (space-borne). Ground-based sensors range from hand-held spectrometers to cameras on tripods. Airborne sensors are deployed on aircraft or drones to gather remote sensing data with high spatial, spectral, and/or temporal resolution, but their use is normally restricted over relatively small areas.

Satellite Remote Sensing (SRS), instead, is an EO technique allowing to acquisition of qualitative and quantitative information from a sensor placed on a platform (satellite-based) orbiting the Earth at heights of 500 to 800 km. The technology permits gathering information over large geographic areas, providing a valuable tool for accurate mapping, and monitoring large-scale phenomena over time. SRS sensors can work either passively or actively. Active remote sensors are characterized by emitting/transmitting the radiation themselves in the direction of the target to be examined and then measuring the scattered returning signal for deriving information about the Earth's surface. On the contrary, passive remote sensors measure the radiation that is reflected, emitted, or scattered by either the object or the scene being observed (Campbell and Wynne, 2011). The sources of the radiation (i.e., illumination) are external and can be both natural (e.g., the Sun) or artificial.

The varying characteristics of both active and passive remote sensors include:

1. The *spatial resolution*, meaning the size of the smallest object that can be identified by a given sensor and corresponds to the size of an individual pixel. A high spatial resolution corresponds to a smaller pixel size. It mainly depends on both sensor technical features and the distance of the sensor from the Earth's surface (Latty et al., 1985).
2. The *spectral resolution* is defined by the minimum value range in wavelength that can be distinguished by a sensor. It is indicated by the number of channels (individual spectral bands) and their width.
3. The *temporal resolution* refers to the time between two successive images acquired for the same scene. It depends on the orbit re-visit time of a satellite, which means how often a satellite passes over the same area.
4. The *radiometric resolution* is based on the minimum value in the intensity of radiation that can be distinguished by the sensor.

Some of the characteristics of the most used SRS sensors currently operating are reported in Figure 3.1.

The remote sensors mentioned above can measure radiation through the Visible to the Thermal infrared (VNIR to TIR) wavelength range of the electromagnetic spectrum (from 400 nm to 1 mm), but also at longer wavelengths in the microwave region (1 mm – 1 m) (Fig. 3.2).

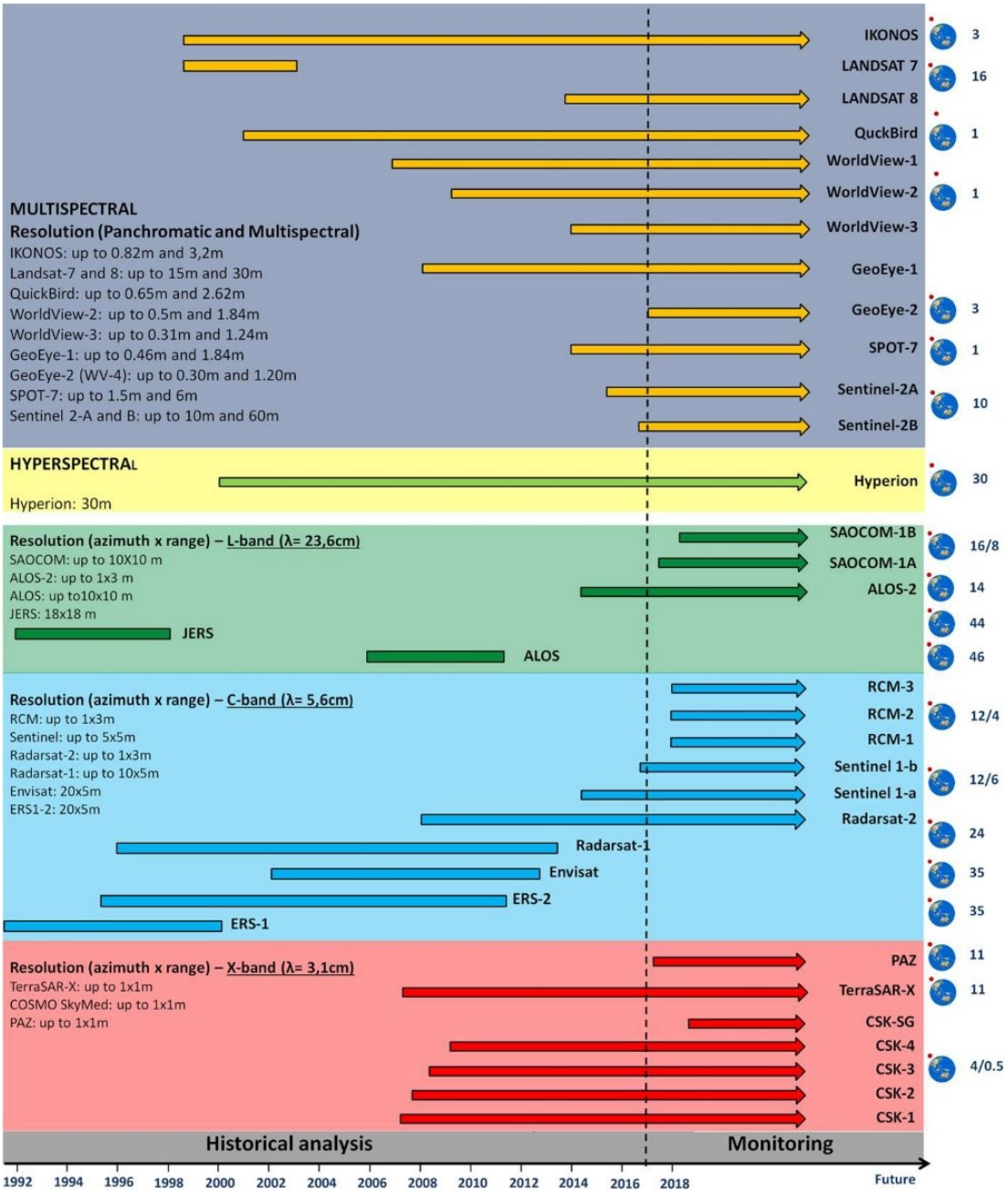

Fig. 3.1 Operating optical and SAR satellites until 2018, on the right is reported the orbit re-visit time for each satellite. RCM: Radarsat constellation mission, CSK: COSMO-Skymed, CSK–SG: COSMO-Skymed Second Generation (Casagli et al., 2017).

Most of the active sensors operate at longer wavelengths of the electromagnetic spectrum from the microwave and the radio wave regions, for instance, the Radio Detection and Ranging (Radar) remote sensing, making them able to penetrate the

atmosphere under the most variable atmospheric conditions since the atmospheric absorption is typically very low.

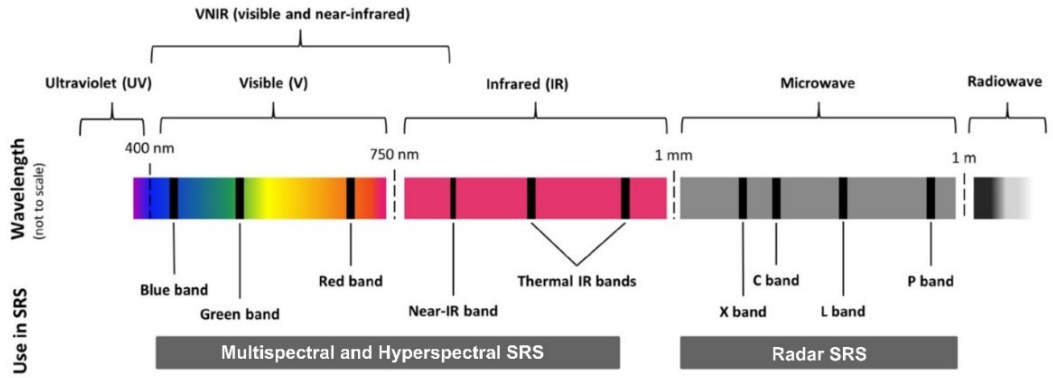

Fig. 3.2 Schematic representation of the electromagnetic spectrum with bands used in passive and active satellite remote sensing (SRS) applications (modified from (Pettorelli et al., 2014).

The radar sensors are generally used for the Synthetic Aperture Radar (SAR) interferometric technique applications (e.g., monitoring of natural hazards, subsidence, and structural stability of infrastructures), for which radar images are processed to generate maps of surface deformation over time (up to mm scale) or digital elevation, using differences in the phase of the signal returning to the satellite or aircraft (Casagli et al., 2017). Other active systems and techniques include the Light Detection And Ranging (LiDAR), which are designed for emitting a laser beam, and then detecting the returning signal in order to measure the distance between the sensor and the object.

Differently from the systems mentioned above, the SRS passive sensors can acquire images over the VNIR-TIR, and in some isolated cases, the microwave regions of the electromagnetic spectrum. The passive sensors category includes mainly Optical Spaceborne Spectrometers, such as multispectral and hyperspectral sensors, which are described in detail in Chapter 4.

Chapter 4:

Optical Satellite Remote Sensing

4.1 Introduction

The main aim of Optical SRS is to measure quantitatively the components exposed on the Earth's surface from calibrated (radiance, reflectance, or emissivity) spectra acquired as images of the investigated scene. The Optical SRS instruments combine two sensing modalities: imaging and spectroscopy. An imaging system captures a picture of a remote scene related to the spatial distribution of the energy of reflected and/or emitted electromagnetic radiation. On the other hand, spectroscopy measures its variation with the wavelength or frequency of light, capturing information related to the chemical composition of the materials measured (Fig. 4.1). The instrumentation used to capture such spectral information is called an imaging spectrometer.

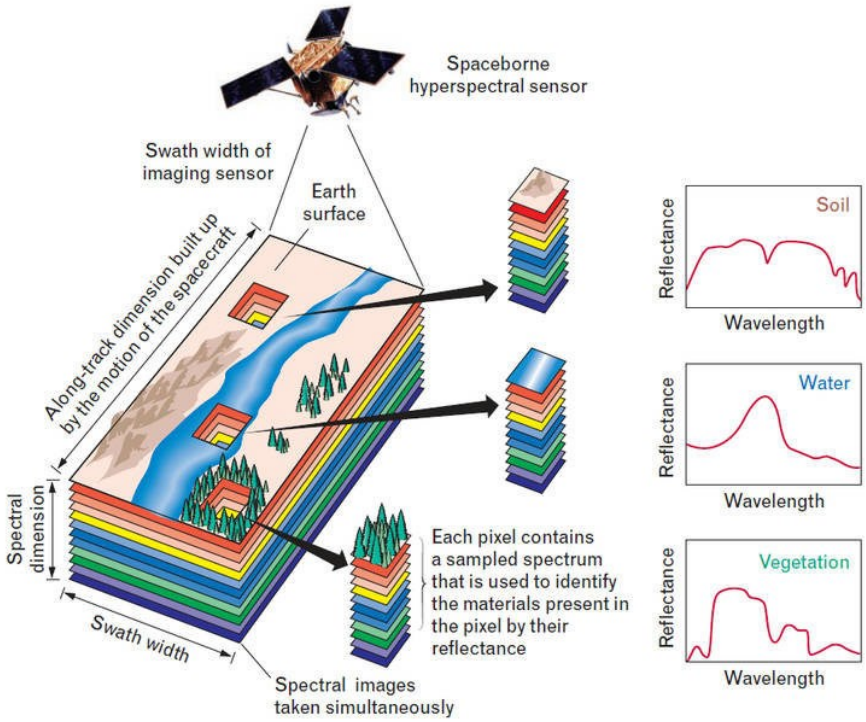

Fig. 4.1 Optical Satellite Remote Sensing (SRS) schematic concept. The reflectance spectral signature for soil, water, and vegetation are shown. Notes: swath=standard size of a single image (from Shaw and Burke, 2003).

The physical parameter measured by optical sensors is the radiance, which is the amount of radiation reflected from a given surface per unit solid angle per unit projected area, measured in watt per steradian per square meter ($W \cdot sr^{-1} \cdot m^{-2}$).

However, the sensor does not automatically measure the radiances of reflected electromagnetic energy: an electronic sensor measures the intensity by detecting photons, which in turn are converted to electrons and the collected charge to an electrical signal. Then, the analogic electrical signal is sampled and converted into a digital signal, recorded in matrix form, and known as a *Digital Number (DN)* (Tempfli et al., 2009), which defines each pixel of the acquired image. The process of transforming *DNs* into radiances is called "radiometric calibration".

Optical SRS sensors measure the radiances of reflected electromagnetic energy (and, therefore, reflectance) of a given target area in discrete spectral bands. A spectral band or wavelength band is defined as the interval of the electromagnetic spectrum for which the average radiance is measured. A spectra acquisition can be represented as a cube of data in which the spatial information is collected on the X-Y plane, while the spectral information is represented along the Z axis, the so-called *datacube* (*hypercube* for hyperspectral acquisitions, Shaw and Burke, 2003). The *datacubes* are generally composed of as many bands as the sensor can acquire (Fig. 4.2; Shaw and Burke, 2003).

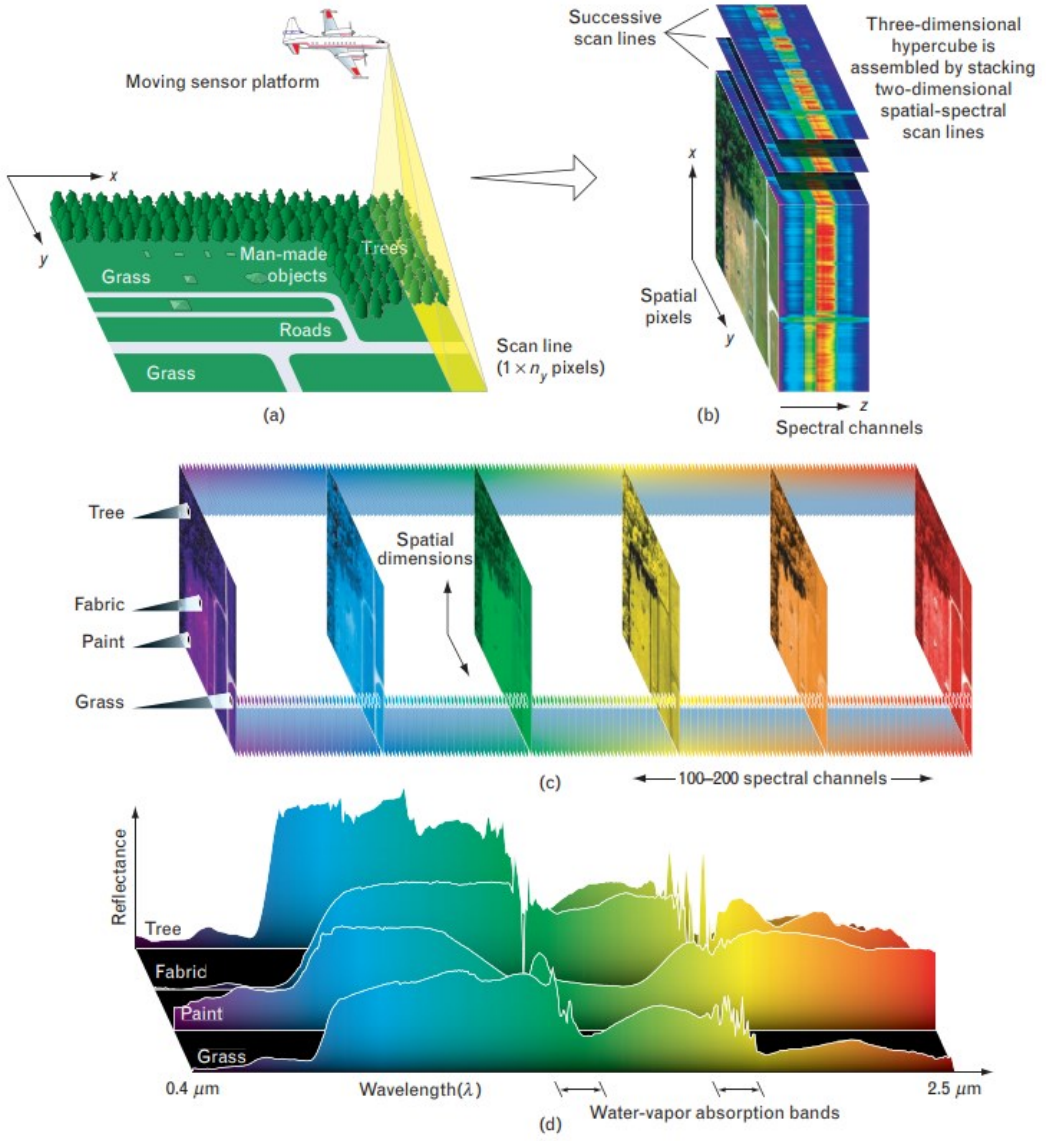

Fig. 4.2 Schematic representation of the hyperspectral data cube (*hypercube*). (a) A push-broom airborne or spaceborne hyperspectral sensor collects spectral information for a one-dimensional row of cross-track pixels (*scan line);* (b) Scan lines in succession compose the spectra for each row of cross-track pixels. Their stacking composes the three-dimensional *hypercube*. (c) The three-dimensional *hypercube* can be treated as a stack of two-dimensional spatial images, each corresponding to a narrow band at a different wavelength. (d) the spectra can be displayed for each pixel or each class of material (from Shaw and Burke, 2003).

The electromagnetic energy passing through the atmosphere can be partly absorbed by various molecules. Ozone (O_3), water vapor (H_2O), and carbon dioxide (CO_2)

represent the most efficient absorbers of solar radiation in the atmosphere (Shaw and Burke, 2003). Consequently, some wavelength intervals are not useful for SRS of the Earth's surface, because the energy is not able to penetrate the atmosphere. Therefore, only the spectrum regions outside the main absorption intervals of absorption by the atmospheric gases are available for Optical SRS. For this reason, such intervals are called "atmospheric transmission windows".

The atmospheric windows of acquisition in which the currently commercially available Optical SRS instruments operate include:

1. The window from 400 to 2500 nm: The radiation in this range (Visible, NIR, SWIR) is mainly reflected energy. Since this type of radiation follows the laws of optics, remote sensors operating in this range are often referred to as "optical" *sensu stricto* (Living Textbook, ITC-University of Twente). The absorption of solar radiation by atmospheric gases in these transmission windows is restricted to narrow wavelength ranges at around 1400 and 1900 nm.
2. Three windows in the TIR range, including two narrow windows around 3000 and 5000 nm, and a third, relatively broad window extending from approximately 8000 to 14000 nm.

Since the Optical SRS relies on the concept of comparison, an instrument for comparing the energy measured in different conditions is needed: the reflectance (Vaccaro, 2017).

Reflectance is defined as the relationship between energy reflected from a given surface and the energy incident on it. The reflectance is a dimensionless quantity and can be expressed as (Vaccaro, 2017):

$$\rho = \frac{\pi Lr}{I} \tag{1}$$

Where Lr is the reflected radiance, and I is the incident irradiance.

The reflectance extended to the full IR spectrum, and therefore the spectral signature, allows to completely break free from the atmospheric conditions at the time of acquisition making comparable measurements conducted at different times. For this

reason, the atmospheric correction of the data is needed for retrieving spectral reflectance from the radiance images. In simple terms, if we know the acquisition time of an image, the atmospheric conditions at that time (e.g., in scene water vapor estimation), as well as the position of the satellite, we can work out the illumination conditions, and then derive the Bottom Of Atmosphere (BOA) reflectance (at surface reflectance) for each pixel composing the image. Scattering, absorption, and emission effects of the atmosphere within the acquired scenes can affect the production of mapping products (i.e., mineral mapping), producing artifacts within the acquired spectral signatures.

However, the data used in this Thesis were downloaded as already atmospherically corrected hypercubes, following the standard data processing chain developed by the Italian Space Agency (ASI - Agenzia Spaziale Italiana) and the European Space Agency (ESA).

4.2 Multispectral (MS) and Hyperspectral (HS) imagery and satellites

Optical SRS instruments include both multispectral (MS) and hyperspectral (HS) remote imaging spectrometers. The main difference between the MS and the HS remote sensors relies on the number of images acquired in each spectral band of the same scene and at the same time. HS Instruments (HSIs) are designed for acquiring images in many, narrow and contiguous intervals of wavelengths (i.e., spectral bands) (Fig. 4.3). On the contrary, MS sensors measure the radiance in a small number of well-defined spectral bands (Fig. 4.3).

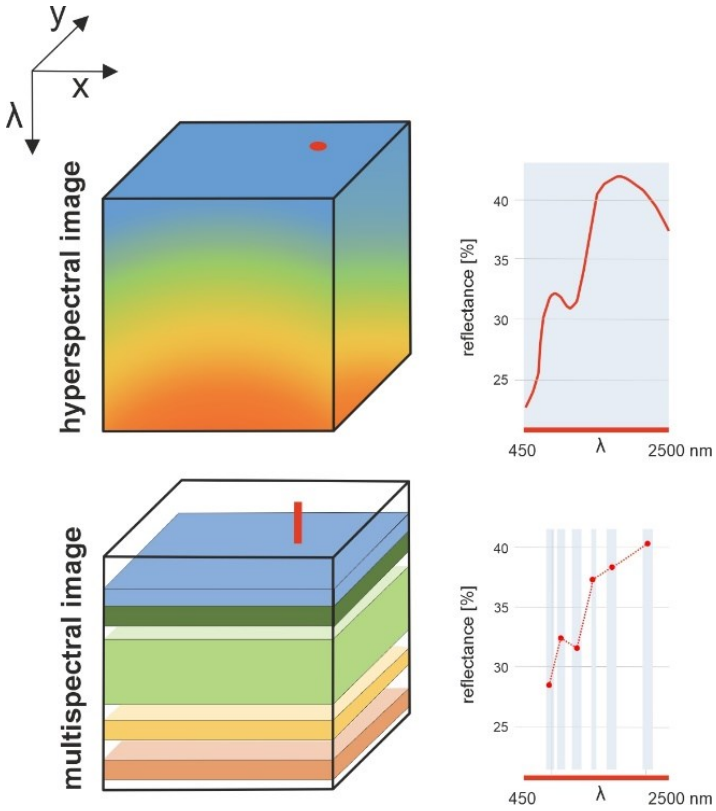

Fig. 4.3 Comparison between HSIs (above) and MSIs (below) *datacubes* and the respective differences in terms of spectral signatures which can be collected.

Open-access MS data are probably the most widely used type of satellite data for environmental, geological, and ecological applications, especially when dealing with large geographic areas (Hansen and Loveland, 2012). Open-access MSIs include, among others (see Fig. 4.4), the United States Geological Survey's (USGS) Landsat satellites, which include eight satellites in total, two of them (i.e., Landsat 7 ETM+ and Landsat 8 OLI/TIRS) are currently in orbit. Other important spaceborne MSIs for geological mapping and mineral detection applications are the ESA's Sentinel-2 and the Japanese spaceborne ASTER mission ("LP DAAC - ASTER Overview,") on board the US TERRA platform (http://terra.nasa.gov/) (e.g., Cudahy et al., 2008; van der Werff and van der Meer, 2015, and references therein). Sentinel-2 provides imagery with a maximum spatial resolution of 10m/pixel (4 bands in the VNIR region), while the remaining bands have a spatial resolution of 20 m and 60 m, (ESA 2015, Fig. 4.3). It consists of two distinct satellites (Sentinel-2A and 2B), respectively launched in 2015 and 2017. They are in the same orbit but phased 180°

from each other. Therefore, even if each twin passes a given area every 10 days, the acquisition frequency is of 5 days over the Equator if considering both Sentinel-2A and 2B, while lower at higher latitudes. Since 2000, ASTER has provided multispectral imagery completely covering the Earth's surface with a spectral resolution of 14 spectral bands over the VNIR (3 bands at 15m/pixel resolution), the SWIR (6 bands at 30m/pixel resolution) and the TIR (5 bands at 90m/pixel resolution) regions.

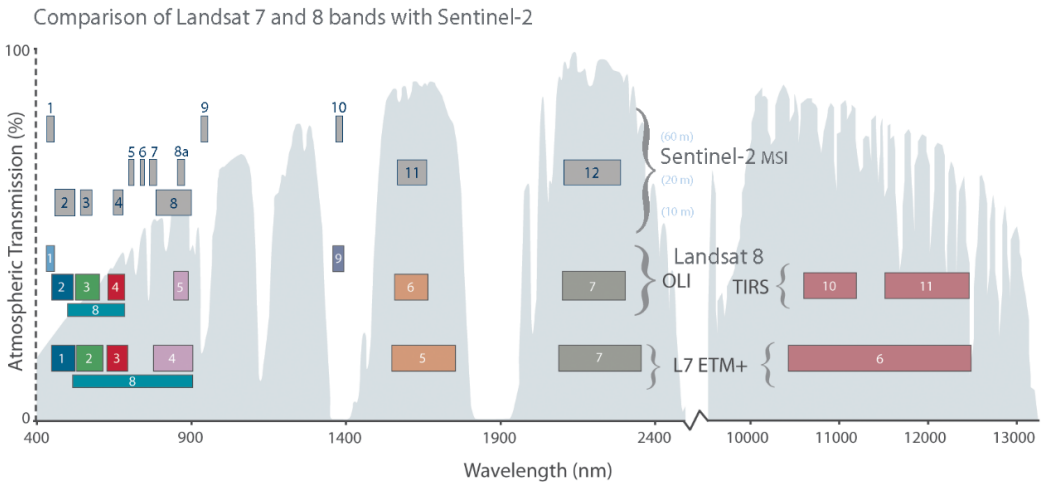

Fig. 4.4 Comparison between the spectral bands of Landsat 7, 8, and Sentinel-2 MSIs (image credits: "Landsat Science")

Hyperspectral remote sensing was born in the 80s with the main purpose of remote mineral detection and lithological mapping. The technique is also known as "imaging spectroscopy" due to the intrinsic characteristic of HSIs: the availability of hundreds (over 200) of spectral bands, which allows obtaining a proximally continuous radiometric distribution (spectral signature) over the spectral ranges covered by the spectrometer, compared to multispectral data that give only "snapshots" of reflectance at discrete points (Fig. 4.2). Both the strength and the weakness of the hyperspectral techniques lay in the high spectral resolution (van der Meer et al., 2012). The technique brings several advantages: (1) the high spectral resolution of the HS sensors permits mimicking reflectance or radiance spectra acquired by field-based instruments, therefore, (2) it allows direct cross-comparison to field data; (3) the range of different applications, including the geological SRS, is wider compared

to MS sensors. However, the disadvantages are: (1) the engineering challenge to acquire such data at a sufficient quality (mainly in terms of SNR), which represents the main problem for spaceborne acquisition, (2) the complexity of the methods for calibration and pre- and postprocessing of the data, (3) the data redundancy due to bands overlap, and (4) the data redundancy related to the acquisition in spectral ranges that are of little user interest.

Over the last four decades, the most used HS systems included mainly airborne sensors (e.g., AVIRIS, HYDICE, DAIS, and HyMAP, van der Meer et al., 2012). At the same time, the availability of spaceborne HSIs makes this technology more available for research purposes.

The National Aeronautics Space Administration's (NASA) pioneering hyperspectral sensor, Hyperion, aboard the Earth Observing-1 satellite (EO-1) was launched in early 2000 (Folkman et al., 2001; Middleton et al., 2017) and decommissioned by the end of March 2017. It acquired images over 242 spectral bands in the VNIR-to-SWIR range. Several further spaceborne hyperspectral sensors have also been launched with the main purposes of scientific research for EO applications, e.g., natural resources and atmosphere monitoring, which include, among others, the German hyperspectral satellite mission “Environmental Mapping and Analysis Program” (“ EnMAP Mission” n.d.), and PRISMA (used in this Thesis). However, there are plans for the future development of hyperspectral satellite sensors (e.g., HypXIM and HyspIRI; Peyghambari and Zhang, 2021).

The majority of the spaceborne HSI have a moderate spatial resolution (generally, 30m/pixel). Some of the hyperspectral sensors such as PRISMA and forthcoming HypXIM use the advantages of co-registered panchromatic cameras with a resolution of 5 and 2m/pixel, respectively.

4.3 The PRISMA hyperspectral mission

PRISMA, the acronym for *Precursore Iperspettrale della Missione Applicativa*, is one of the most recently launched imaging spectroscopy satellites and represents a follow-up of NASA’s satellite Hyperion. PRISMA is a small-size satellite mission with an expected operational mission lifetime of 5 years, built for ASI by OHB Italia

Spa as the main contractor (Cogliati et al., 2021). The payload instruments were developed by Leonardo Space & Airborne Systems (Coppo et al., 2020). PRISMA was launched on March 22nd, 2019, by ASI aboard the Vega Flight VV14 from Europe's Spaceport in Kourou, French Guiana. The PRISMA mission is targeted to offer spaceborne imaging spectroscopy data at an unprecedented high spectral resolution across the full VNIR and SWIR spectral range (Loizzo et al., 2018), in order to promote novel processing methods and to support the development of new applications based on high spectral resolution images (Pignatti et al., 2013), including resource exploration and management and environmental monitoring.

Fig. 4.5 Artist's rendition of the PRISMA satellite (image credits: ASI)

The satellite (Fig. 4.5) is flying in a frozen Sun-Synchronous Low Earth Orbit at an altitude of 614.8 km with an inclination of 97.851° (Cogliati et al., 2021; Loizzo et al., 2018). The orbit re-visit time is of 29 days (from nadir) with a re-look capacity for a requested specific target of 7 days with off-nadir viewing. The geographic coverage is between 70°S – 70°N latitude (at equinoxes) and 180°W – 180°E longitude (ASI, 2020). However, imagery acquisition at higher latitudes is also possible, with the only limitation related to low solar zenith angle.

The standard size of a single image (swath) is 30 × 30 km, but full-resolution payload data up to 1800 km × 30 km, as the maximum length of a single acquisition,

can also be acquired. The push broom scanning hyperspectral camera (Fig. 4.6), based on prism technology, acquires a continuum of 234 spectral bands in the spectral range between 400 nm to 2500 nm (VNIR to SWIR), with a spectral resolution ranging from 11 to 15 nm subdivided as follows: 66 VNIR (30 m/pixel), 171 SWIR (30 m/pixel) (ASI, 2020; Loizzo et al., 2018; Cogliati et al., 2021).

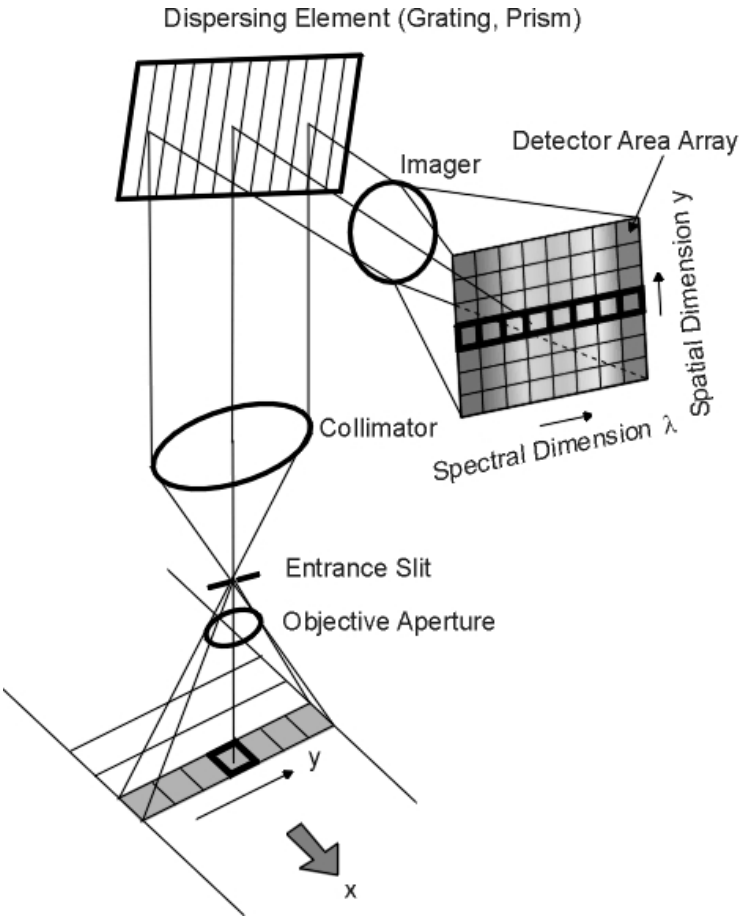

Fig. 4.6 Scheme of a push broom scanning hyperspectral instrument. (from He et al., 2012)

The hyperspectral datum is filed in HDF-EOS5 format (Hierarchical Data Format – Earth Observing System). A co-registered 5.1 m/pixel panchromatic image (PAN) acquiring the same area is also provided (Cogliati et al., 2021), useful for a better interpretation of the hyperspectral data (Fig. 4.7).

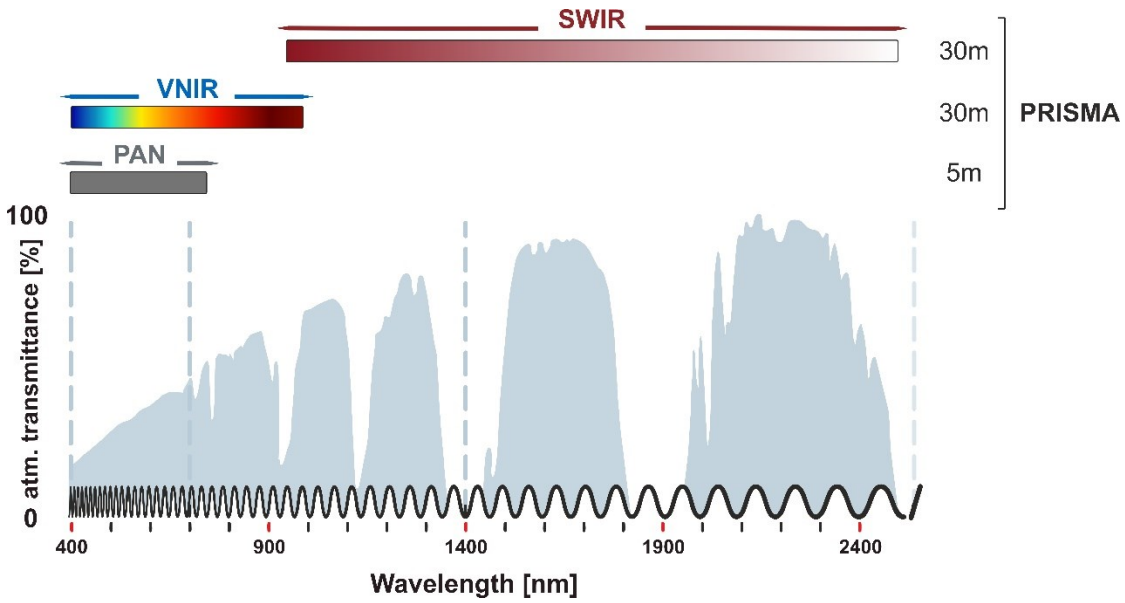

Fig. 4.7 PRISMA hyperspectral sensor coverage over the VNIR-to-SWIR wavelength range and the products respective Ground Sampling Distance.

The standard processing products available to users and systematically produced by the PRISMA ground processor are as follows:

- Level 1 Top of Atmosphere (TOA) radiometrically and geometrically calibrated radiance images;
- Level 2 geolocated and geocoded atmospherically corrected (Bottom Of Atmosphere - BOA) images.

Details and documentation about each product can be found within the PRISMA Products Specification (ASI, 2020).

Alongside several papers focusing on the ASI's PRISMA hyperspectral sensor mission's development, capabilities, performance analysis and potential uses, and application fields (Amato et al., 2013; Cogliati et al., 2021; De Bonis et al., 2015; Loizzo et al., 2018; Pignatti et al., 2013, and references therein), recent works using PRISMA images mainly focused on the first assessment of the potential of PRISMA for detecting and classifying vegetation, forest types, agricultural application, as well as land-use monitoring and hazard management (Casa et al., 2020; Pepe et al., 2020; Vangi et al., 2021). Other successful recent applications include water monitoring, as well as inland/coastal water quality assessment (Giardino et al., 2020; Niroumand-

Jadidi et al., 2020). Other expected benefits cover several fields of application including mapping of raw materials and lithologies (Bedini and Chen, 2020; Chirico et al., 2023; Heller Pearlshtien et al., 2021; Laukamp, 2022) PRISMA, in fact, covers the mineral-diagnostic wavelength regions at hyperspectral resolution and signal-to-noise ratio (SNR) from ≥ 200:1 (VNIR) to >100:1 (SWIR 2), and it has the potential to recognize and map the Earth's surface materials, discriminating between different geological targets according to their diagnostic spectral responses.

Chapter 5:

Mapping hydrothermal and supergene alteration zones associated with carbonate hosted Zn-Pb deposits by using an integrated approach of mineralogical, geochemical, field-based and satellite hyperspectral methods

5.1 Introduction

Spectral remote sensing technology represents a tool that has been well-established in applied geology for over four decades (Bedini, 2017; Peyghambari and Zhang, 2021; and reference therein). The main aim of spectral remote sensing is to detect and quantitatively measure the earth's surface materials, by using calibrated reflectance spectra acquired as images in hundreds of narrow and contiguous spectral bands, generally ranging from the Visible Near InfraRed (VNIR; 400 to 1300 nm) to Short Wave InfraRed (SWIR; 1300 to 2600 nm) regions of the electromagnetic spectrum (van der Meer et al., 2012). Several rock-forming and alteration minerals show diagnostic spectral absorptions in the VNIR, SWIR 1 (1300 to 1850 nm), and SWIR 2 (1850 to 2600 nm) wavelength ranges. These wavelength ranges are suitable for geological spectral sensing applications as they provide mineralogical and geochemical information due to electronic transitions and vibrational processes in minerals (Clark et al., 1990b). Characteristic spectral features can be used for defining the occurrence and relative abundance of mineral species and their physicochemical variations (Laukamp et al., 2021). Since its advent, geological remote sensing has been used as a tool for the exploration of mineral deposits. Even though spectral sensing has been applied to the study and exploration of several ore deposit types through different scales of observation (e.g., Lampinen et al., 2017; Bedini, 2017; Laukamp et al., 2022, and references therein), its potential still remains underexplored for the investigation of several ore minerals of notable economic importance. At the same time, more advanced satellites are launched ever more frequently, making the available spectral data increasingly detailed in both the spatial and the spectral resolution (i.e., hyperspectral systems are characterized by a higher

number of channels compared to multispectral sensors; Peyghambari et al., 2021). The present study aims to test the effectiveness of the newly launched Italian Space Agency's (ASI) PRISMA (Precursore IperSpettrale della Missione Applicativa) hyperspectral satellite for the exploration of carbonate-hosted base metal deposits. The application of hyperspectral remote sensing technology in the exploration of carbonate-hosted base-metal and Mississippi Valley-type (MVT) deposits is challenging for two main reasons: (1) the limited wavelength range needed for distinguishing the carbonate minerals and, (2) the limited availability of hyperspectral imagery covering longer wavelength regions where the carbonate minerals are active (Bedini, 2017). Large-scale features potentially allow the application of spectral remote sensing techniques to the exploration of carbonate-hosted ore deposits. They include, firstly, the hydrothermally derived dolomites, which in most cases are spatially and temporally associated with base-metal mineralization (Ridley, 2013). Secondly, gossans, which are mostly composed of high amounts of Fe-oxides and hydroxides and associated with the supergene weathering of the buried sulfide orebodies (Taylor, 2011). In this study, we propose a methodology based on remote and proximal spectral sensing to infer the relative abundances and spatial distribution of specific minerals associated with the surface-exposed alteration products typically found together with the Zn-Pb mineralization in carbonate-hosted and MVT systems. Several methods are proposed in order to determine the respective absorption feature characteristics from hyperspectral reflectance spectra (see the review by Laukamp et al., 2021). Nevertheless, the classification of hyperspectral images can be very challenging for several reasons, including data noise, high data dimensionality, and redundancy, as well as the presence of mixed pixels and limited availability of training samples (Kale et al., 2017). The feature-based band ratio approach (Laukamp, 2022), instead, has several advantages. Firstly, it involves a small number of spectral bands, with the result that it is not computationally intensive. Secondly, it can be implemented following a transferable workflow for mapping lithology in almost all geological settings, and can be applied to all types of hyperspectral reflectance spectra that are collected by most of the imaging systems and sensors at different scales of observation, such as

field spectrometers, drill core sensors, airborne sensors (e.g., HyMap, HyVista Corporation; AVIRIS, NASA/JPL) available on the market, and even some non-commercial spaceborne instruments (e.g., PRISMA, ASI; Hyperion), as in the present study.

Only limited studies using PRISMA data focus on lithological mapping (e.g., Bedini and Chen, 2020; Heller Pearlshtien et al., 2021, Laukamp, 2022). Geological applications of PRISMA images include till now: (1) the mapping of hydrothermal alteration assemblages; (2) the definition of the spatial distribution of alteration minerals, for example, white micas associated with hydrothermal systems in the Cuprite area in Nevada, USA (Bedini and Chen, 2020); (3) detecting CO_2 emissions (Romaniello et al. 2021, 2022); as well as (4) mapping methane emission points at upstream facilities of the oil and gas industry (Guanter et al., 2021). Heller Pearlshtien et al. (2021), instead, proposed a very detailed study based on the spectral performances of both Level 1 (L1 -radiance) and Level 2 (L2 - reflectance) PRISMA products over well-known geological features in the Makhtesh Ramon national park area in Israel. Specifically, the latter authors proceed by comparing hyperspectral PRISMA data to both AisaFENIX airborne hyperspectral and USGS spectral libraries data, demonstrating that PRISMA L1 products provide an accurate spectral-based mapping of minerals over the Makhtesh Ramon area. Heller Pearlshtien et al., (2021) produced good results especially for Fe oxy-hydroxides (goethite and hematite), gypsum, and clay minerals, while L2D products showed inaccuracies due to noise and reflectance interference across the SWIR-2 long-wavelengths region. However, on the latest specific point, by using the mineral absorption feature-based band ratios method, Laukamp (2022) could successfully use the L2D PRISMA products, being able to map bedrock geology and regolith in Rocklea Dome, Western Australia, considering SWIR-2-active minerals, like: chlorite, epidote, and other minerals.

The main aims of this study are: (a) to test the effectiveness of PRISMA as a tool for mineral exploration, and (b) to develop new workflows for identifying Zn-Pb mineralized areas. Specifically, we provide a new method for the extraction of

mineralogical-chemical features related to carbonate-hosted and MVT ore deposits and related supergene alteration using PRISMA-derived data, in part interpreted by referencing field-based hyperspectral data. The method is focused on the depth of specific features, for the identification of ferric oxides- and carbonate-bearing rocks, which can be spectrally separated due to the main Fe^{3+}- and CO_3 ion-related absorption features in the VNIR and SWIR-2, respectively. Despite previous studies (e.g., Heller Pearlshtien et al., 2021) encountering problems in mapping carbonate phases using L2 PRISMA scenes, the method proposed in this study shows satisfactory results in mapping both limestones and dolomites.

The test area selected for this study is the Jabali district in Yemen. The district is situated about 110 km to the north-east of the capital city Sana'a, on the northwestern margin of the Sab'atayn sedimentary basin which hosts the main hydrocarbon resources in Yemen (Al Ganad et al., 1994; Christmann et al., 1989) (Fig. 5.1a). The district also includes the Jabali Zn-Pb deposit, which is one of the most important Zn-Pb-(Ag) deposit of the Arabian shield (Mondillo et al., 2014). The entire district was already field mapped by the Yemen Geological Survey (Christmann et al., 1989 and references therein). In addition, local spectral maps were produced using Landsat (MSS, TM, ETM+), QuickBird, and ALOS AVNIR-2 multispectral satellite data (Deroin et al., 2011, 2012), with satisfactory results in characterizing gossans and less accuracy with carbonate rocks. This information makes possible the validation of the PRISMA-derived maps at the district scale. For this study, a PRISMA level 2C (Bottom-Of-Atmosphere reflectance) datum was used for the detailed discrimination between distinct geological targets, since it covers at hyperspectral resolution at a sufficiently high signal-to-noise (SNR) ratio (Loizzo et al., 2018) for the wavelength regions diagnostic of the target minerals. Several ground samples from the Jabali deposit were characterized through the use of field reflectance spectroscopy, X-ray powder diffraction (XRPD) with Quantitative phase analysis (QPA), and whole-rock geochemical analyses (ICP-MS/ES), for better interpretation of the satellite hyperspectral data.

5.2 Geological setting

5.2.1 Regional Geology

The Jabali ore deposit is located on the eastern flank of a local uplifted block, known as the Jabali-Majnah paleohorst, situated on the northwestern edge of the Late Jurassic-Early Cretaceous Marib-Al-Jawf/Sab'atayn basin (Fig. 5.1b). The Sab'atayn basin has a NW-SE orientation resulting from the development of extensional faults along the pre-existing Precambrian basement wrench-faults. It is mainly characterized by Mesozoic pre-, syn- and post-rift sedimentary sequences, represented by fluviatile red beds of the Kuhlan Formation and shallow marine carbonate sequences of the Amran Group, transgressive over the Precambrian metavolcanic and metasedimentary basement rocks, consisting of schists and quartzites intruded by granite and pegmatite (Al Ganad et al. 1994) (Figs. 5.1b, c).

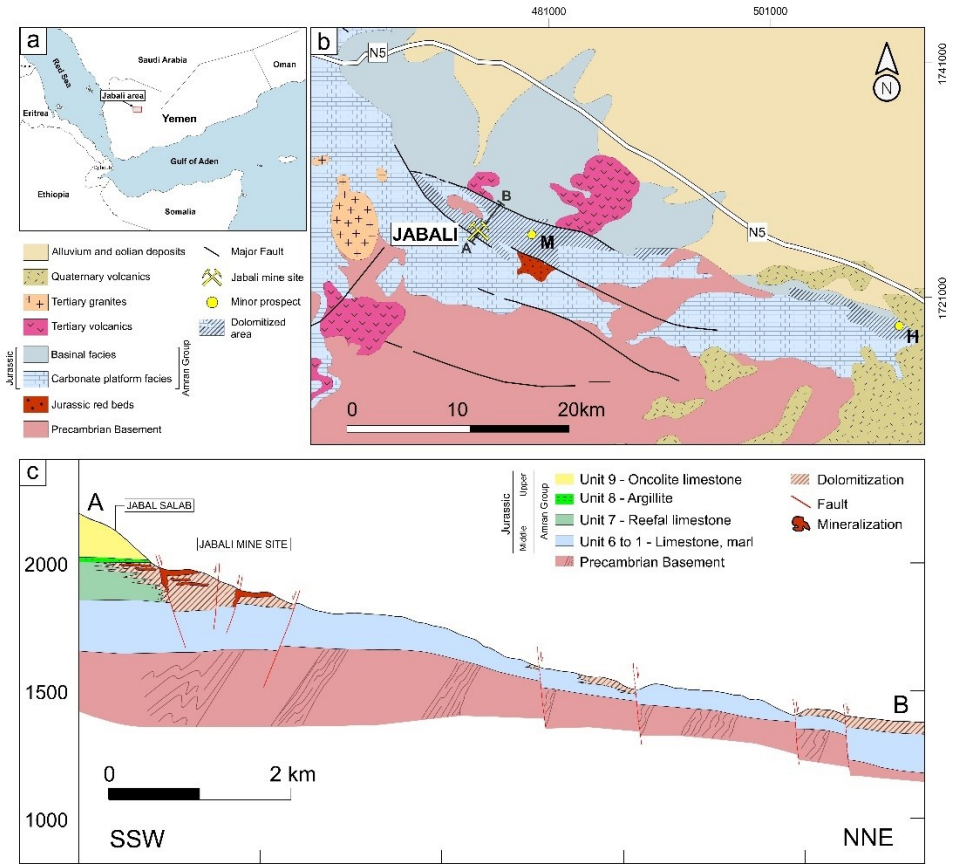

Fig. 5.1 (a) Location of the Jabali mine site; (b) Simplified geological map of the western portion of the Sab'atayn basin. The known Zn-Pb occurrences are highlighted. M: Majnah

Ba, Pb, Zn mineralized zone; H: Jabal Haylan gossans. Modified from (Christmann et al., 1989). (c) Schematic NNE cross-section showing the mineralization and the Jurassic sequence in the study area (section trace is shown in Fig. 1B). Modified from (Christmann et al., 1989).

Tertiary alkaline granite bodies are present at Jabal as Saad, 15 km to the west of the Jabali mine site (Mondillo et al., 2014) (Fig. 5.1b). The Zn-Pb(-Ag) ores are mainly hosted by strongly dolomitized platform carbonates of the pre- to syn-rift Shuqra Formation (Amran Group, Jurassic) (As-Saruri et al., 2010; Mondillo et al., 2014; Santoro et al., 2015) (Fig. 5.1b, c; Fig. 5.2). Locally, the Shuqra Formation is subdivided into seven units (members), based on different sedimentological features (Al Ganad et al., 1994; Mondillo et al., 2014). Units from 1 to 6 are neither mineralized nor dolomitized. Unit 7 appears almost completely dolomitized and is the main host for the Zn ores. The overlying Madbi Formation (0-30 m), locally called Unit 8, consists of organic-rich mudstones with gypsum and dolomite intercalations. The topmost Sab'atayn Formation, locally known as Unit 9, is characterized by biomicrites with oncolites and bio-oocalcarenites, as well as intercalations of gypsum lenses (Christmann et al., 1989) (Fig. 5.2).

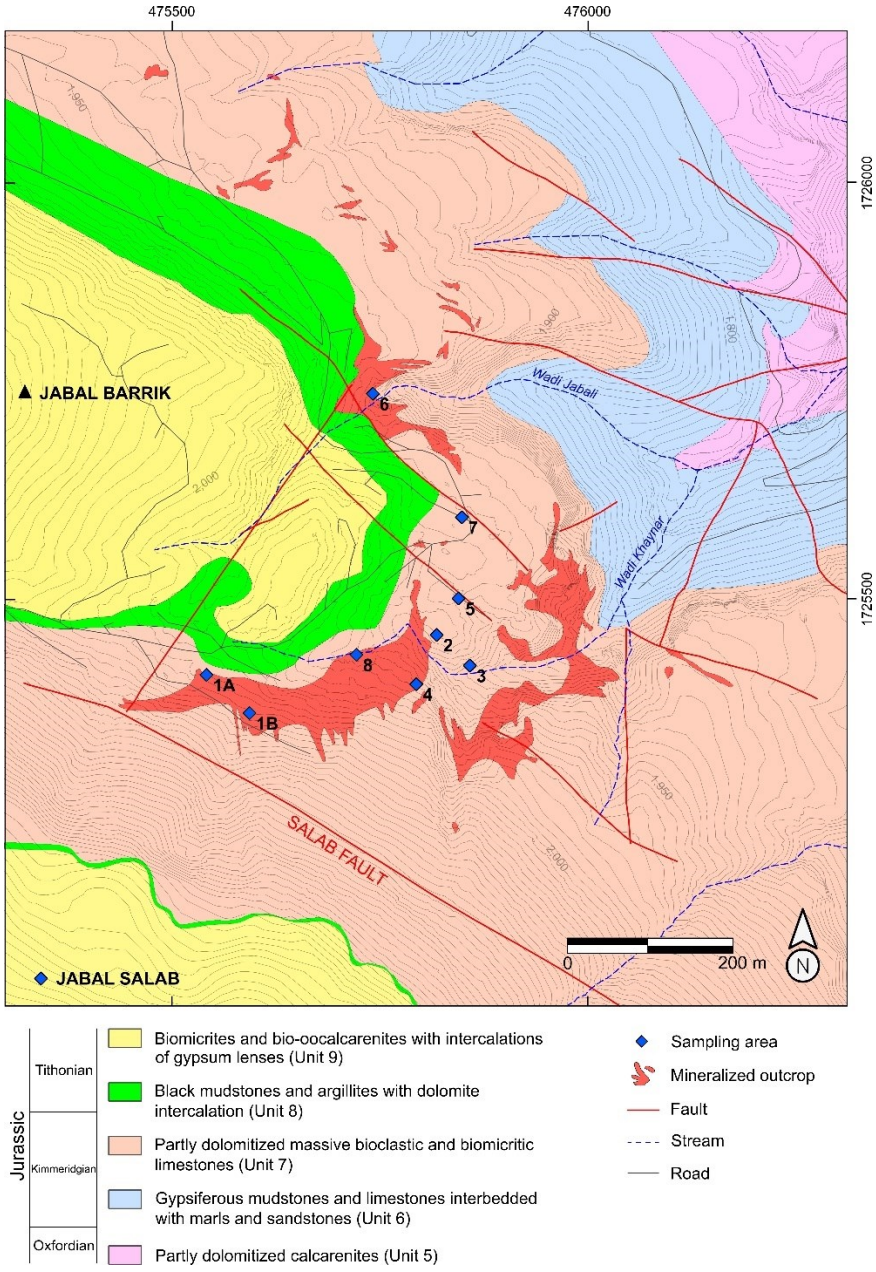

Fig. 5.2 Geological map of the Jabali mining site with the location of the analyzed samples (modified from Mondillo et al. 2014; Santoro et al. 2015; SRK Consulting, 2005).

The sedimentary succession at Jabali is sub-horizontal, with just a few areas showing W-dipping strata. It is characterized mainly by brittle deformation related to extensional rift tectonics. The main normal fault system shows a NW-SE-strike (120° to 140°), dipping to the northeast, and can be observed bordering the plateau's southern side, below the Jabal Salab peak. Further sets of normal faults have 65° to

80° and 0° to 5° trends, while a minor fracture trend varies between 25° and 40° (Mondillo et al. 2014; SRK Consulting, 2005) (Fig. 5.2). Faults dip angles generally range between 60° and 80°.

5.2.2 Zn-Pb mineralization

The Jabali deposit represents the most prominent example of carbonate-hosted hydrothermal Ag-rich Zn-Pb mineralization of the Sab´atayn Basin (Christmann et al., 1989; McCombe et al., 1994; Ostendorf et al., 2015). The estimated resources of 12.6 Mt at 8.9% Zn, 1.2% Pb, and 68 mg/kg Ag (SRK Consulting, 2005) are characterized by Zn-oxidized minerals (also called "nonsulfides"), derived from the alteration of preexisting Zn sulfides (Mondillo et al. 2011, 2014; Ostendorf et al. 2015). The orebodies in part outcrop at the surface in the form of Fe-oxy-hydroxides-rich gossans and nonsulfides derived from supergene alteration (Figs. 5.1c and 5.2), with many more present in the subsurface below Jabal Barrik (Mondillo et al., 2014; Santoro et al., 2015). The orebodies are either stratabound following the dolostone layering or structurally controlled along vertical fractures, faults, and fault intersections (Al Ganad et al., 1994; Mondillo et al., 2014). Primary sulfide mineralization, consisting of sphalerite, galena, and pyrite, has been preserved locally in intervals underlying the Madbi Formation (Unit 8; Fig. 5.1c) and corresponds to a Late Jurassic extensional MVT (Al Ganad et al., 1994; Mondillo et al., 2014; Ostendorf et al., 2015). Two distinct dolomite generations have been observed within the study area (Al Ganad et al., 1994; Mondillo et al., 2014): (1) an early diagenetic dolomite at district-scale and, (2) a hydrothermal dolomite, genetically associated with Zn-Pb sulfide deposition. The latest consists of Fe-Mn-bearing saddle crystals (FeO up to 6 wt % and MnO up to 2 wt %) (Mondillo et al., 2014) occurring in geodes, veins, and replacing the former diagenetic generation. The ore-related hydrothermal dolomite bodies are mainly controlled by porosity and fractures, following the main N120° to N140° structural trend observed in the area (Christmann et al., 1989) (Figs. 5.1c and 5.2). Both the dolomite generations are affected by two different alteration/replacement processes: (1) de-dolomitization, occurring as calcite formation by replacement of the former dolomite crystals, as

well as Fe^{2+} altered to Fe^{3+} reprecipitating in form of Fe^{3+}-oxy-hydroxides in the interstices of the crystals and pores; (2) dolomite replacement by Zn-bearing dolomite (17–22 wt.% ZnO) (Mondillo et al., 2014, 2011; Santoro et al., 2015), where Zn^{2+} replaces Mg^{2+} in the dolomite as a consequence of interaction with Zn-enriched groundwaters after sulfides alteration processes, and formation of Fe- oxy-hydroxides due to the release of Mn^{2+} and Fe^{2+} after oxidation. The oxidized mineralization at Jabali consists of massive to semi-massive and disseminated orebodies of nonsulfide mineral aggregates (Mondillo et al., 2014, 2011; Santoro et al., 2015). Smithsonite represents the main economic mineral and is associated with minor hemimorphite and hydrozincite, with disseminated Ag-sulfides. Smithsonite replaces both sphalerite and all the dolomite phases described above (Mondillo et al., 2014). It is suggested that the oxidized mineralization formed since the early Miocene (~17 Ma) after the alteration of preexisting sulfides due to the action of supergene waters mixed with low-temperature hydrothermal fluids (Mondillo et al., 2014).

5.3 VNIR and SWIR absorption features of minerals investigated in carbonate-hosted Zn-Pb deposits

The spectral range between 400 nm to 2500 nm (VNIR to SWIR) characterizes many hydrothermal and supergene minerals in terms of spectral responses, allowing their identification when they are considered target minerals. Displacements of the absorption feature to either longer or shorter wavelengths can highlight either mineral compositional variations or mineral mixing, whereas absorption band depth (relative to the background continuum) can be assumed to be proportional to the mineral relative abundance (Clark et al., 1990b). Reference spectral reflectance features of the main host-rock and supergene alteration minerals observed in the Jabali samples are shown in Tab. 5.1. Two main processes cause the mineral-related absorption features in the SWIR 2 range (Laukamp et al. 2021): (1) combinations ($\nu + \delta OH$) of hydroxyl-related fundamental stretching (νOH) and bending vibrations (δOH), and (2) combinations (e.g., $2\nu_3 + \nu_1$ CO_3) or overtones (e.g., $3\nu_3 CO_3$) of carbonate-related fundamental stretching vibrations. Several authors have

comprehensively studied the spectral properties of carbonates (Clark et al., 1990b; Crowley, 1986; Gaffey, 1986, 1985; Green and Schodlok, 2016; Hunt and Salisbury, 1971; Kurz et al., 2012; Laukamp et al., 2021; van der Meer, 1995; Zaini et al., 2012).

Tab. 5.1 Reference spectral reflectance features of the main host-rock and supergene alteration minerals observed in the Jabali samples

Mineral	Formula	Characteristic spectral features in VNIR	Characteristic spectral features in SWIR	References
Dolomite	$CaMg(CO_3)_2$	Fe^{2+} broad double absorption band centered at 1200 nm (only for ferroan dolomites)	CO_3 at 2320 nm (major). Shifted to longer wavelengths for ferroan dolomites.	Gaffey (1986)
Calcite	$CaCO_3$	Fe^{2+} broad double absorption band centered at 1300 nm (only for ferroan calcites)	CO_3 at 1750 nm and 2160 nm (min); 2335 nm (major). Shifted to longer wavelengths for ferroan calcite.	Gaffey (1986)
Smithsonite	$ZnCO_3$	Red peak; broad depression at 800–1200 nm	CO_3 at 2320 nm (min) and 2360 nm (major)	McConachy et al. (2007)
Hydrozincite	$Zn_5(CO_3)_2(OH)_6$	Peak at 600 nm	OH at 1430 nm and 1500 nm; CO_3 at 2300 nm and 2390 nm (major); min unknown at 1800 nm, 1850 nm, 1970 nm and 2025 nm	McConachy et al. (2007)
Goethite	α-FeO(OH)	Peak at 764 nm; CTF at 480 nm and 670 nm (min), and CFA at 940 nm (major)	OH and H_2O at 1451 nm and 1935 nm	Crowley et al. (2003); Cudahy et al. (1997)
Hematite	α-Fe_2O_3	Peak at 749 nm; CFA at 880 nm		Crowley et al. (2003); Cudahy et al. (1997)
Hemimorphite	$Zn_4Si_2O_7(OH)_2H_2O$		OH and H_2O at 975 nm, 1160 nm, 1400 nm and 1940 nm; weak Zn–OH (?) at 2210 nm	McConachy et al. (2007)
Sauconite	$Na_{0.3}Zn_3(Si,Al)_4O_{10}(OH)_2(H_2O)$		H_2O at 1,910 nm and OH at 1420 nm; possible Zn–OH at 2305 nm	McConachy et al. (2007)
Jarosite	$KFe_3(SO_4)_2(OH)_6$	Peak at 717 nm; CFT at 437 nm and CFA at 911 nm (major)	OH (and adsorbed H_2O) at 1467 nm, 1849 nm and 1936 nm; Fe-OH at 2264	Crowley et al. (2003); Cudahy et al. (1997)

As a general rule, carbonate minerals can be distinguished in the SWIR by the presence of two main spectral absorption features in the wavelength regions around 2300- 2350 nm and 2500–2550 nm (Clark et al., 1990b; Gaffey, 1986; Hunt and Salisbury, 1971; Zaini et al., 2012), the latter of which is generally placed at the boundary of the wavelength ranges acquired by the most common hyperspectral instruments. In this context, the main absorption feature considered ($3\nu_3CO_3$) for calcite occurs in the 2335-2340 nm wavelength region. Several factors control the position of carbonate absorption bands at the atomic level (e.g., cation mass, cation

radius, cation, and anion valences, cation coordinate number, the gap between cation and anion, and site symmetry), as well as physical and chemical properties (i.e., grain size, texture, packing or porosity, carbonate mineral content, chemical composition). The grain size has effects on the absolute reflectance values (band absolute depth), but absorption feature position, width and asymmetry are not significantly affected either by grain size or packing in the SWIR wavelength region (Gaffey 1986; Zaini et al. 2012). The quantity of metal cation (Mg, Fe, and Mn replacing Ca) bonded to the CO_3^{2-} in the crystal lattice and the relative amounts of carbonate phases composing the samples, instead, can control the wavelength position and the geometry of such absorption features (Gaffey, 1986; Hunt and Ashley, 1979; Laukamp et al., 2021), therefore positions of the main carbonate absorption features can shift with changes in chemical composition, proportionally with the amount of metal cation replacing Ca (Gaffey, 1986, 1985). Thus, the main CO_3^{2-} absorption appears shifted to shorter wavelengths for dolomites, with the main feature occurring at 2320 nm. The latter property is generally used as a diagnostic feature to make a distinction between limestone and dolomite (Clark et al. 1990b; Kurz et al. 2012; van der Meer, 1995; Windeler and Lyon, 1991). Moreover, the main absorptions appear asymmetric with a shoulder on the short-wavelength side (Gaffey, 1986, 1985), pointing to a secondary weaker absorption probably centered in the 2230-2275 nm range (Laukamp et al. 2021). Increasing Fe content can cause carbonate bands in dolomite and calcite spectra to shift to longer wavelengths, associated with broad double bands centered near 1200 nm and 1300 nm, respectively, attributed to electronic transitions of the Fe^{2+} ion (Crystal Field Absorption band - CFA). Furthermore, an increase in the intensity of this feature was observed in association with increasing iron content in dolomites and calcites (Gaffey, 1986). However, the strength of the Fe^{2+} CFA feature was found to be very variable, especially when comparing it across mineral species (Gaffey, 1986; Green and Schodlok, 2016; Hunt and Salisbury, 1971; Lampinen et al., 2019). Two less intense diagnostic absorption features in calcite occur at around 1990 nm (medium intensity) and 1870 nm (weak intensity), respectively. The intensity of these absorption features decreases with increasing Mg or Fe content. However, because they overlap with the main OH/H_2O

absorption at around 1900 nm, these features can be obliterated, becoming not useful for satellite-based hyperspectral analyses. According to Laukamp et al. (2021), they can help when the true nature of a left-hand asymmetric absorption feature in the 2340-nm region is dubious.

The Zn carbonates smithsonite ($ZnCO_3$) and hydrozincite ($Zn_5(CO_3)_2(OH)_6$) show the carbonate absorption features in the range between 2300 nm and 2400 nm (McConachy et al., 2007). The main CO_3^{2-} absorption band for smithsonite is present at 2365 nm, whereas hydrozincite absorptions occur as only minor absorptions at 2300 nm and 2400 nm. Smithsonite can change in color from white to brown-red varieties. The brown-red variety shows deep and broad crystal field effects, due to Zn^{2+} between 800 nm and 1200 nm, centered around 960 nm (McConachy et al., 2007).

H_2O and/or OH-bearing Zn silicates, such as hemimorphite ($Zn_4Si_2O_7(OH)_2H_2O$) and sauconite ($Na_{0,3}Zn_3(Si, Al)_4O_{10}(OH)_2(H_2O)$), are characterized by significant absorption features close to 1400 nm and 1900 nm, caused by the first overtone of O–H stretching vibration and the combination of O–H stretching and H–O–H bending vibrations, respectively (Crowley, 1991; Hunt, 1971; Hunt and Salisbury, 1971; McConachy et al., 2007). Nevertheless, these features are not useful for satellite-based hyperspectral analyses, because of atmospheric interferences. Weaker absorption bands in the SWIR region, instead, are related to Zn–OH, occurring at 2210 nm for hemimorphite and 2305 nm for sauconite. Si–O bonding appears very weak in the SWIR (McConachy et al., 2007).

Iron-bearing oxides/hydroxides (i. e. hematite and goethite; Crowley et al. 2003; Cudahy and Ramanaidou, 1997; Curtiss, 1985) are defined by diagnostic absorption features in the range between 450 nm and 1200 nm, corresponding to the VNIR region of the electromagnetic spectrum. The significant absorption bands of these phases are caused by electronic processes involving Fe^{3+} octahedrally bonded to ligands of oxygen (hematite α-Fe_2O_3) or oxygen and hydroxyl (goethite – α-FeO(OH)) (Cudahy and Ramanaidou, 1997). In detail, hematite exhibits its

diagnostic absorption feature typically at ~ 880 nm, which is related to energy level changes in the valence electrons (CFA). The major CFA feature of goethite appears, instead, shifted to longer wavelengths compared to hematite, occurring generally at ~ 940 nm (Crowley et al., 2003; Cudahy and Ramanaidou, 1997). Other weaker absorption bands are at 480 nm and 670 nm (Charge Transfer Feature – CTF; Cudahy and Ramanaidou, 1997), and the water-related features are close to 1400 nm and 1900 nm. Absorption position shifting to longer wavelengths of the main Fe-bearing oxides/hydroxides feature (of about 14 nm; Scheinost et al., 1999) is due to compositional modifications related to Al^{3+} substitution for Fe^{3+} iron (Cudahy and Ramanaidou, 1997). As a common product of supergene alteration of sulfides ores, jarosite ($KFe_3(SO_4)_2(OH)_6$) can show the CFA absorption features at ~910 nm and ~437 nm, together with the weaker 650 nm band (Crowley et al., 2003). Moreover, jarosite (as well as plumbojarosite) shows OH-related features at around 2212 nm and 2263 nm, which it shares with di-octahedral and tri-octahedral sheet silicates, respectively (Bishop and Murad, 2005; Laukamp et al., 2021).

Di-octahedral sheet silicates (white micas, Al-smectites, and kaolinite) are SWIR 2-active mineral phases, producing a characteristic Al-OH spectral absorption feature between 2195 and 2225 nm. The absorption is related to the presence of hydroxyl bound to Al (Al-OH) in the octahedral layer, and it is given by the combination of the Al-OH bending and the O-H stretching vibration ($\nu + \delta Al_2OH$; (Vedder and McDonald, 1963; Vedder, 1964; Hunt, 1977; Clark et al., 1990b; van der Meer, 2004; Laukamp et al., 2021).

The O-H-related absorption feature in white micas is centered at around 2350 nm, overlapping the carbonate spectral feature in the same range from 2300 to 2550 nm (Clark et al., 1990b; van der Meer, 2004). As noted earlier, the left-hand symmetry shown by the spectral absorption feature at 2300 to 2335 nm, can be used to distinguish them from white micas (Gaffey, 1986; Lampinen et al., 2017).

Tab. 5.2 Indexes (in italics) used for the identification of the various mineral groups and mineral phases based on their absorption features in the VNIR and SWIR regions, and their applicability. The stretch values give the lower and upper limits applied to the respective index for the PRISMA mineral maps.

Index name	Index Identifier	Applicability	Algorithm	PRISMA algorithm	Stretch lower limit*	Stretch upper limit*	References
Mg-OH feature depth	***2350D***	Abundances of both carbonates (e.g., calcite, dolomite) and trioctahedral silicates (e.g., chlorite, epidote, amphibole, talc, FeMg-clays).	(R2327 + R2364)/R2349	*(B149+B154)/B152*	1.97	2.12	Laukamp et al. (2011)
Al-sheetsilicate feature depth (ASA)	***2200D***	Abundance of white micas (e.g. illite, muscovite, paragonite, brammalite, phengite, lepidolite, margarite) and smectites (montmorillonite, beidellite)	(R2143 + R2229)/R2206	*(B125+B136)/B133; masked with 2350D<2.0*	2.15	2.32	Laukamp (2022); Sonntag et al. (2012)
Dolomites feature depth	***2320D***	Abundance of dolomites	(R2298 + R2342)/R2320	*(B145+B151)/B148*	2.08	2.15	Gaffey (1986); Laukamp et al. (2012)
Fe oxy-hydroxides abundance (FOA)	***900D***	Abundance of mixture of hematite, goethite, "limonite", ferrihydrite, jarosite, Fe^{3+}-carbonate	(R770+R962)/R908	*(B44+B62)/B57 , masked with 2350D<2.0 and 2200D>2.15*	2.3	2.4	Cudahy et al. (2008); Haest et al. (2012a, 2012b); Laukamp (2022)

5.4 Materials and Methods

5.4.1 Analysis of Ground Samples

For this study, 17 ground samples (carbonate host-rock, and Fe- and Zn-bearing mineralized products) from 10 sampling areas of the Jabali mine site were analyzed (Fig. 5.2). VNIR-to-SWIR reflectance spectra were measured in the laboratory at CSIRO Mineral Resources (Perth, Western Australia), focusing on both fresh and altered portions, using a FieldSpec Pro 3 spectrometer, which records spectra via contact probe, with a data acquisition spot size of 10 mm, and a spectral resolution of 10 nm with a sampling interval of 1 nm in the 350- to 2500-nm wavelength range ("Malvern Panalytical" n.d.). Acquired hyperspectral data were downsampled using ENVI 5.6.1 software (L3Harris Technologies, USA) to the PRISMA resolution (see Cogliati et al., 2021 for specifications), to test the effect of spectral resolution on the measuring and mapping of the abundance and composition of specific minerals. The Spectral Library Resampling tool in ENVI was used for downsampling the field-based spectral library by applying a Gaussian model proving wavelengths (band centers) and full-width-half-maximum (FWHM) information obtained from the PRISMA input data file.

Spectra display, analysis and interpretation were carried out using The Spectral Geologist software (TSG^{TM} version 8.0.7.4, CSIRO, Perth, WA, Australia, ("The Spectral Geologist," n.d.), accessed on 25 November 2021). Since the characteristics of the absorption features of the mineral phases of interest (summarized in Tab. 5.1) can be extracted from reflectance spectra through band ratios or polynomial fitting, the spectra analysis was performed by plotting the relative intensities of each diagnostic absorption feature obtained by feature extraction scripts, then shown in binary discrimination diagrams. We used the feature extraction scripts derived from previous work by Cudahy et al. (2008) and Lampinen et al. (2019), Laukamp et al. (2011, 2021), that were adapted to the PRISMA bands setting and applied to reflectance spectra downsampled to the PRISMA spectral resolution, after continuum removal by division of the reflectance spectrum by the continuum. For extraction of the relative abundance of a given mineral, the sum of two spectral bands located at

the shoulders of a given absorption feature is divided by one or more bands located at the center of the absorption minimum. The binary diagrams are useful to identify clusters of mineral species or groups characterizing the analyzed samples, to evaluate their spectral behavior, and, amongst other applications, to estimate relative mineral abundances and compositional changes. The feature extraction indexes description is shown in Tab. 5.2. We firstly focused on the SWIR 2 wavelength region (between 2000 and 2500 nm) by using the 2320D and 2350D feature extraction scripts, plotted against the Carbonate Composition script (Sonntag et al., 2012). The VNIR region, instead, was considered for evaluating the Ferric Oxide Abundance, applying the same-named feature extraction script (hereinafter referred to as 900D), plotted against the Hematite-Goethite ratio (Cudahy et al., 2008; Cudahy and Ramanaidou, 1997). The authors decided to keep the same nomenclature adopted in previous studies, labeling the latter scripts by the center wavelength position followed by D (for "depth") (Laukamp et al. 2021).

To validate the laboratory reflectance hyperspectral measurements, X-ray Powder Diffraction (XRPD) and Quantitative Phase Analysis (QPA) were conducted on the 17 milled samples (Tab. 5.3), corresponding to the half counterparts of the samples used for spectral analysis. An aliquot of 20 wt % corundum was added to the powders to quantify mineral and amorphous contents. The XRPD analyses were conducted at the Osservatorio Vesuviano-INGV (Napoli, Italia) with a Panalytical X'pert PRO PW 3040/60 Malvern- Panalytical diffractometer in Bragg-Brentano geometry with unfiltered CuKα radiation (40 kV, 40 mA) in the 3°-70° 2θ range, in steps of 0.02° 2θ, counting time in 30 s/step. Diffraction patterns were interpreted using the HighScore software version 4.9 (Malvern - PANalytical B.V.) and JCPDS PDF-2 database. QPA followed the combined Rietveld and Reference Intensity Ratio (RIR) methods (Bish and Post, 1993; Chung, 1974a, 1974b; Gualtieri et al., 1996; Gualtieri, 2000). The profile was refined using the High Score plus 4.9 software exporting the structure models for each phase from ICSD data library. Rietveld refinement has been performed by correcting major parameters like scale factor, flat background, zero shift, lattice parameters, half-width, orientation parameters, U V

W, peak shape parameters, etc., to obtain high Goodness of Fitment (GOF) and reliable Rwp and Rp agreement indexes. Bulk-rock geochemical analyses (Tab. 5.4) were used to better evaluate compositional variations characterizing the samples, to calibrate the XRPD analyses (see for example Santoro et al. 2021), and for comparison with the reflectance spectroscopic data. Ten grams of identical split powders to those used for the XRPD analyses were used for determining major, minor, and trace element concentrations by Bureau Veritas Commodities Canada Ltd. (Vancouver, Canada). Major oxides were analyzed by Inductively Coupled Plasma Emission Spectroscopy (ICP-ES) and Trace Elements by Inductively Coupled Plasma-Mass Spectroscopy (ICP-MS), following a lithium borate fusion on the LF202 package, in which the samples are fused with $Li_2B4O_7/LiBO_2$ fluxes before being analyzed by ICP-ES/MS. Fe^{2+} was analyzed using the GC806 package (FeO Titration). Zn and Pb over limits were analyzed by GC816 (Zn Titration) and GC817 (Pb Titration), respectively.

Tab. 5.3 Mineral abundances (wt.%) from X-ray diffraction quantitative analysis of outcrop samples.

Sample ID	Sampling area	Sample group	Dol	Cal	Hm	Hyd	Sm	Qz	Gth	Hem	Sme	Jrs	Pb-Jrs	Kln	Ilt	Gp	Cph	A-FeHyOX	TOT
JSMAR4	8	Zn ore	72		3	20.2					0.8						1.3	2.7	100
JSMAR5	2	Zn ore	24	54.8	2.9		8	1			0.2							9.1	100
JSMAR7	7	Gossan		64.5					31			0.5		tr.				4	100
JSMAR8	7	Zn ore		6.9	23.2	56.9	5											8	100
JSMON H9		Host rock		96.1														3.9	100
JSMON13	1B	Zn ore	34.5				55.7		1.5		1			tr.				7.3	100
JSMON16	2	Gossan		43				1.3	20.7	13.2								21.8	100
JSMON18	3	Gossan		18.8				3.6	6.1	23.2	8		16.5			0.2		23.6	100
JSMON2	1A	Host rock	72.5	7			14.6		4								1.3	0.6	100
JSMON20	3	Zn ore			14.5	19.1	4.6		40.4									21.4	100
JSMON23	4	Host rock	87	1					1.7		2							8.3	100
JSMON25	4	Gossan		26.7					47.5									25.8	100
JSMON29	5	Zn ore			8.5	77.6	2.2				2.5							9.2	100
JSMON31	5	Gossan		1					61.3	15.4				1.3				21	100
JSMON33	6	Host rock	74.5	14.9							4.5							6.1	100
JSMON39	Jabal Salab	Gossan		34.5					49.2									16.3	100
JSMON3b	1A	Host rock	88.5	4.8			0.7							tr.				6	100

Notes: The sampling areas' location is indicated in Fig. 5.2; "tr." traces. Minerals' names abbreviations mostly after Mondillo et al. (2014) - Dol: dolomite; Cal: calcite; Hm: hemimorphite; Hyd: hydrozincite; Sm: smithsonite; Qz: quartz; Gth: goethite; Hem: hematite; Sme: smectites; Fld: feldspar; Jrs: jarosite; Pb-jrs: plumbojarosite; Kln: kaolinite; Ilt: Illite; Gp: gypsum; Cph: chalcophanite; A-FeHyOX: Amorphous Fe-hydroxides.

Tab. 5.4 Major (wt.%) and minor (mg/kg) element concentrations of outcrop reference samples from ICP-ES/MS analysis.

	Sample ID	MDL	JSMAR4	JSMAR5	JSMAR7	JSMAR8	JSMON H9	JSMON13	JSMON16	JSMON18	JSMON2	JSMON20	JSMON23	JSMON25	JSMON29	JSMON31	JSMON33	JSMON39	JSMON3b
Wt%																			
SiO_2	LF200	0.01	1.15	1.96	0.82	7.6	0.64	1.14	2.76	8.08	0.54	4.43	1.35	2.1	2.64	2.03	1.94	2.58	0.62
Al_2O_3	LF200	0.01	0.17	0.2	0.22	0.48	0.07	0.25	0.52	4.59	0.05	0.23	0.4	0.41	0.3	0.58	0.83	0.5	0.22
Fe_2O_3	LF200	0.04	2.3	6.3	28.25	4.51	0.34	6.55	43.31	49.89	3.65	50.88	6	55.88	5.83	78.95	3.94	52.86	2.58
MgO	LF200	0.01	14.97	4.98	0.09	0.14	0.25	7.31	0.27	0.27	15.14	0.09	18.23	0.32	0.14	0.04	15.48	0.24	18.59
CaO	LF200	0.01	23.86	37.33	36.04	3.31	54.73	10.83	23.95	10.59	26.14	0.13	27.55	14.72	0.36	0.56	30.44	19.19	30.04
Na_2O	LF200	0.01	0.05	<0.01	<0.01	0.02	<0.01	<0.01	0.03	0.04	0.01	0.04	<0.01	0.02	0.07	0.18	<0.01	0.01	0.02
K_2O	LF200	0.01	0.02	<0.01	<0.01	<0.01	0.01	<0.01	0.04	0.09	<0.01	0.02	0.03	0.02	0.03	0.13	0.02	0.02	0.03
TiO_2	LF200	0.01	<0.01	<0.01	0.02	0.02	<0.01	0.01	0.1	0.05	<0.01	0.02	0.03	0.04	0.02	0.26	0.06	0.02	0.02
P_2O_5	LF200	0.01	<0.01	0.04	<0.01	0.02	0.01	0.03	0.02	0.11	<0.01	0.03	0.01	0.02	<0.01	0.11	0.03	0.03	0.02
MnO	LF200	0.01	0.89	0.86	0.04	2.22	0.14	1.11	0.05	0.73	0.91	0.06	0.66	0.04	0.99	0.07	0.79	0.04	0.79
FeO	GC806	0.2	<0.20	<0.20	<0.20	<0.20	<0.20	<0.20	0.35	<0.20	<0.20	<0.20	<0.20	<0.20	<0.20	<0.20	<0.20	0.31	1.89
ZnO	GC816*	1	17.54	10	<1.00	59.3	-	37.48	1.97	3.72	10	29.23	3	3.51	65.7	3.01	3.5	1.33	-
PbO	GC817*	2	-	-	<2.00	-	-	-	3.23	6.03	-	-	-	<2.00	-	<2.00	-	<2.00	-
Cr_2O_3	LF200	0.002	<0.002	<0.002	<0.002	<0.002	<0.002	0	0	0.01	<0.002	0	<0.002	0	<0.002	0.01	<0.002	0.01	<0.002
LOI	LF200	-	41.1	38.9	33	20.7	43.7	36.3	24.1	15.4	43	16.1	43.5	21.2	24	13.9	42.9	23.1	46
TOT/C	TC000	0.02	10.87	10.37	8.26	3.46	12.03	9.95	5.55	2.36	11.93	1.54	11.71	3.55	4.07	0.29	11.55	4.25	12.75
TOT/S	TC000	0.02	<0.02	<0.02	0.06	<0.02	<0.02	<0.02	0.19	1.08	<0.02	0.16	<0.02	0.14	0.03	0.18	0.14	0.14	0.02
mg/kg																			
Ba	LF200	1	30	12	4	27	215	14	46	51	29	3	315	12	144	13	71	29	4
Ni	LF200	20	33	<20	<20	<20	<20	125	<20	78	<20	37	<20	21	<20	<20	<20	<20	<20
Sc	LF200	1	<1	1	<1	<1	<1	<1	1	7	<1	<1	<1	<1	<1	2	1	<1	<1
Be	LF200	1	<1	<1	<1	<1	<1	2	<1	4	<1	1	<1	<1	1	<1	<1	<1	<1
Co	LF200	0.2	1.2	2.8	0.4	33.3	0.3	9.5	1.5	26.7	0.9	1.5	0.8	1.1	21.8	0.8	2.6	2.5	1
Cs	LF200	0.1	<0.1	<0.1	<0.1	<0.1	<0.1	<0.1	<0.1	<0.1	<0.1	<0.1	<0.1	<0.1	<0.1	<0.1	<0.1	<0.1	<0.1
Ga	LF200	0.5	<0.5	5.2	0.7	1.2	<0.5	<0.5	14.5	21.7	1	<0.5	0.7	11.1	<0.5	5.2	1	3	<0.5
Hf	LF200	0.1	<0.1	0.1	0.2	0.1	<0.1	<0.1	0.9	0.6	<0.1	0.2	0.3	0.4	0.2	1.7	0.3	0.2	0.4
Nb	LF200	0.1	0.3	0.3	0.4	0.4	0.1	0.2	2.1	1.3	0.2	0.5	0.7	0.7	0.3	6.1	1.2	0.5	0.4
Rb	LF200	0.1	<0.1	0.2	0.1	<0.1	0.4	0.1	1.1	0.7	0.1	<0.1	1.2	0.1	<0.1	0.5	0.8	0.5	1
Sn	LF200	1	<1	1	<1	<1	<1	<1	5	6	<1	<1	<1	5	<1	<1	<1	<1	<1
Sr	LF200	0.5	34.2	106	24.1	13.8	78.7	32.3	397	175.4	19.8	6.8	53.7	21.6	15.5	22.9	86.3	178	48.3
Ta	LF200	0.1	<0.1	<0.1	<0.1	<0.1	<0.1	<0.1	<0.1	<0.1	<0.1	<0.1	<0.1	<0.1	<0.1	0.3	<0.1	<0.1	<0.1
Th	LF200	0.2	<0.2	<0.2	0.3	<0.2	<0.2	<0.2	0.7	1.8	<0.2	<0.2	0.5	0.6	0.2	1.1	0.7	0.5	0.2
U	LF200	0.1	1.7	3.2	2.8	11.8	1	1.3	4	10.9	0.8	2.4	1.6	3	2.8	5.3	2.7	3.8	1.3

V	LF200	8	10	8	<8	13	<8	9	<8	35	<8	<8	17	<8	<8	13	16	<8	8
W	LF200	0.5	<0.5	<0.5	<0.5	<0.5	<0.5	<0.5	0.6	<0.5	<0.5	<0.5	<0.5	<0.5	<0.5	0.9	0.8	<0.5	<0.5
Zr	LF200	0.1	2.1	9.3	6.9	7.6	3.9	3.3	35.5	21.4	3.3	6.6	11.4	15.4	6.5	65.9	12	10.3	25
Y	LF200	0.1	13	23	3.2	10.8	3.3	9.2	3.1	16.8	4.4	4.7	10.3	1.5	5.8	3.3	13.9	4.3	5.2
La	LF200	0.1	8.3	9.3	5	6.3	3	6.8	2.5	17.4	4.2	3	12.2	1.7	5.5	5.1	21.9	4.4	7.9
Ce	LF200	0.1	6.1	9.1	6.5	19	2.9	8.7	4.6	69.4	4.6	3.4	15	2	14.2	8.5	24.5	7	8.2
Pr	LF200	0.02	1.7	1.9	1.1	1.5	0.5	1.2	0.5	3.5	0.6	0.6	1.9	0.2	1.6	0.7	2.9	0.8	1
Nd	LF200	0.3	7.7	8.7	4.4	6.6	1.9	4.5	2.2	16.3	2.5	3.1	7.3	0.9	7.5	2	11.1	3.4	4.2
Sm	LF200	0.1	1.4	2.2	0.9	1.5	0.3	0.8	0.6	5.6	0.5	0.5	1.4	0.2	1.6	0.3	2.2	0.6	0.7
Eu	LF200	0.02	0.5	1.5	0.3	0.9	0.1	0.4	0.2	1.8	0.4	0.3	0.9	0.1	0.7	0.1	1.8	0.2	0.5
Gd	LF200	0.1	2	3.3	0.8	2.2	0.4	1.2	0.6	6.5	0.7	0.7	1.8	0.3	1.5	0.3	3.1	0.8	0.9
Tb	LF200	0.01	0.2	0.5	0.1	0.3	0.1	0.2	0.1	1	0.1	0.1	0.2	0	0.2	0.1	0.3	0.1	0.1
Dy	LF200	0.1	1.4	3.3	0.4	1.6	0.4	0.8	0.5	5.6	0.4	0.6	1.1	0.2	1.1	0.4	1.5	0.6	0.6
Ho	LF200	0.02	0.3	0.7	0.1	0.3	0.1	0.2	0.1	0.9	0.1	0.1	0.2	0	0.2	0.1	0.3	0.1	0.1
Er	LF200	0.03	0.9	2.1	0.2	0.7	0.2	0.6	0.3	2.2	0.3	0.4	0.6	0.1	0.5	0.3	0.7	0.3	0.3
Tm	LF200	0.01	0.1	0.3	<0.01	0.1	0	0	0	0.3	0	0	0.1	<0.01	0.1	0	0.1	0	0
Yb	LF200	0.1	0.6	1.5	0.1	0.4	0.1	0.3	0.3	1.7	0.2	0.3	0.4	0.1	0.4	0.3	0.4	0.3	0.2
Lu	LF200	0.01	0.1	0.2	<0.01	0.1	0	0	0	0.2	0	0	0.1	<0.01	0	0	0.1	0	0
Mo	AQ200	0.1	4	5.5	2.6	9.8	1.4	3.4	5.7	9.2	1.1	5	1.1	2.3	3.1	9.6	3.8	2.5	0.8
Cu	AQ200	0.1	1.8	67.6	3.6	35.3	4.4	37.3	7.6	44.7	24.7	7.1	6.4	20.9	2.7	9.9	11.8	10.2	1.9
Pb	AQ200	0.1	2011.8	>10000.0	5034.1	>10000.0	71.3	7553.9	>10000.0	>10000.0	8107	4610.3	74.7	>10000.0	483.9	2054.4	>10000.0	1303.9	24.2
Zn	AQ200	1	>10000	>10000	5765	>10000	192	>10000	>10000	>10000	>10000	>10000	>10000	>10000	>10000	>10000	>10000	6929	4675
Ni	AQ200	0.1	27	3.7	4.9	24.7	2.2	104.5	10.3	66.2	1.8	32.9	9	18.3	22	14.7	9.8	15.6	1.5
As	AQ200	0.5	3.9	1.6	8.9	3.3	0.7	1.1	19.2	24.5	0.6	17.2	2.8	30.3	1.4	28.8	4.3	17.3	1
Cd	AQ200	0.1	>2000.0	>2000.0	376.9	1490.7	4.8	>2000.0	69.3	33.4	440.7	152	10.4	588.9	439.7	42.4	59.6	6	57.2
Sb	AQ200	0.1	0.1	0.2	<0.1	<0.1	<0.1	<0.1	0.2	0.2	0.1	<0.1	<0.1	0.1	<0.1	0.5	0.4	0.1	<0.1
Bi	AQ200	0.1	<0.1	<0.1	<0.1	<0.1	<0.1	<0.1	<0.1	<0.1	<0.1	<0.1	<0.1	<0.1	<0.1	<0.1	<0.1	<0.1	<0.1
Ag	AQ200	0.1	55	7	2.5	4.8	0.2	19.1	11.6	36	24.3	4.4	35.5	4.8	4.6	3.7	41.4	0.2	1.4
Au	AQ200	0.5	<0.5	<0.5	<0.5	<0.5	<0.5	<0.5	0.8	2	<0.5	<0.5	<0.5	<0.5	<0.5	<0.5	<0.5	1.3	<0.5
Hg	AQ200	0.01	0.2	0.2	0.1	0.2	0	1.2	0.2	0.2	0.2	0.6	0.3	0.7	0.1	0.2	0.1	0.1	<0.01
Tl	AQ200	0.1	5.3	1.9	0.2	4.4	<0.1	3	0.2	1.8	1.1	0.5	1.1	1.4	2.7	1.3	0.2	0.3	<0.1
Se	AQ200	0.5	1	0.7	<0.5	3.2	<0.5	2.1	1.7	1.7	0.7	1.8	<0.5	<0.5	3.6	1.1	<0.5	1	<0.5

Notes: "-" no detected; * corrected for oxides wt%. MDL= minimum detection limit. Methods (Bureau Veritas Commodities Canada Ltd., Vancouver, Canada): LF202 package, which includes LF200, TC000 (IR Combustion – total C and S), and AQ200: $Li_2B_4O_7/LiBO_2$ + aqua regia (AQ) digestion ICP-ES/MS; GC806 FeO by Titration; GC816 Zn by Titration; GC817 Pb by Titration.

5.4.2 Satellite hyperspectral data collection and processing

The mineral maps presented in this article are based on a Bottom-Of-Atmosphere (BOA) reflectance hyperspectral satellite image using the PRISMA[1] hyperspectral satellite sensor, which is currently acquiring data all over the World, releasing free images to scientific community and the public. The hyperspectral datum (PRS_L2C_STD) was acquired at 07:41:46 a.m. on 21 November 2021 (UTC) and downloaded from the mission website (" PRISMA data portal" n.d.; accessed on 21 November 2021) (Fig. 5.3).

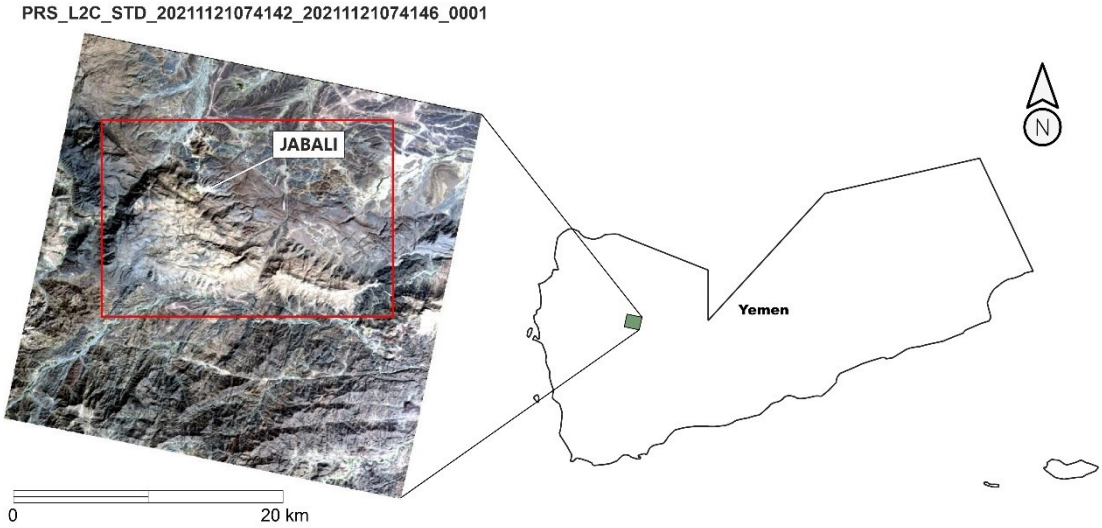

Fig. 5.3 The Jabali study area. PRISMA True colors image (product identifier: PRS_L2C_STD_20211121074142_20211121074146_0001) and its location. The red box highlights the processed Area of Interest subset.

The L2 PRISMA products are atmospherically corrected images following the standard data processing chain developed by ASI for PRISMA (see PRISMA product specifications, " PRISMA data portal").

[1] Project carried out using PRISMA Products, © of the Italian Space Agency (ASI), delivered under an ASI License to use by visiting prisma.asi.it ("PRISMA data portal").

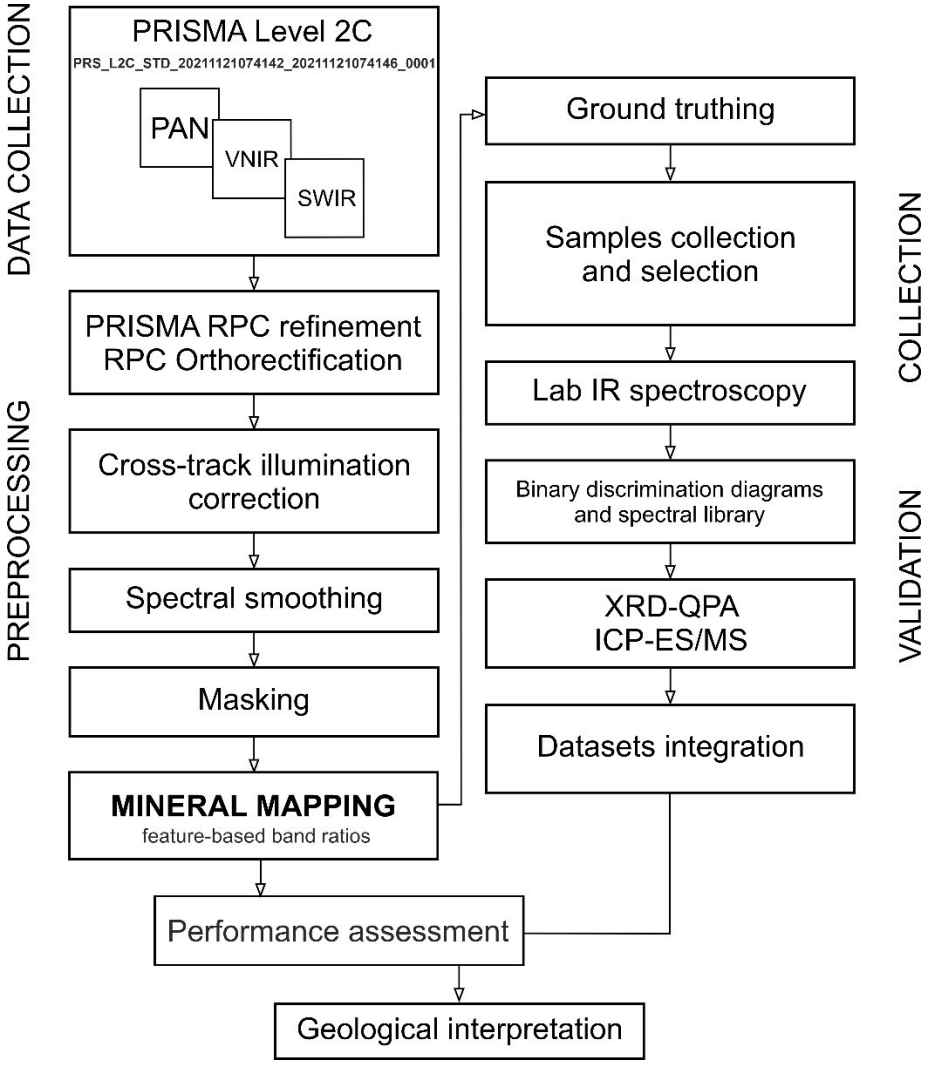

Fig. 5.4 Schematic multi-scale workflow used in this study.

The workflow proposed for this study (Fig. 5.4) was performed using a range of tools in ENVI 5.6.1. At first sight, PRISMA hyperspectral bands strongly affected by atmospheric absorption were excluded from further processing. Atmospheric absorption bands occur in the wavelength ranges between 1317 to 1533 nm and 1,784 to 2035 nm, corresponding to the band ranges from B39 to B59 and from B84 to B112, where B is used to indicate spectral bands of the PRISMA SWIR cube. Due to their low SNR, SWIR bands from B158 (2392 nm) to B173 (2495 nm) were not considered. Errors in the absolute geolocation of ~100 m of the L2D PRISMA images introduced issues in the comparison with field hyperspectral data. However,

the geolocation was improved using the Refine RPCs (HDF-EOS5) task, contained within the PRISMA Toolkit, a recently developed extension for ENVI. The task relies on a Sentinel-2 reference image with the same acquisition date, which has geometric localization errors not greater than 5 to 10 m (Sentinel-2 User Handbook, 2015). Cross-track illumination correction (using a sample-based approach) was applied to both VNIR and SWIR scenes, before stacking them to investigate the full wavelength range as determined by target minerals' significant absorption features. The latter correction was applied to reduce the "see-saw" pattern in the VNIR wavelength range that is caused by the applied spectral resampling during the smile correction processing within the L1 processor (Cogliati et al. 2021). The product's stacking was performed using the Build HSI Cube task, included in the PRISMA Toolkit in ENVI, which allows the combination of the VNIR and SWIR datasets and the removal of the redundant overlapping wavelengths. The final processed product includes only 168 bands out of 234 original bands. The stacked product was smoothed before further processing, using the Savitzky-Golay smoothing filter in ENVI (Savitzky and Golay, 1964). The best results were obtained by using a combination of filter parameters including Filter Width=3, Order of the Derivative=0, and Degree of Smoothing Polynomial =2. Pixels affected by shadows or belonging to non-geological materials, mainly vegetation, and man-made features, were masked and excluded as well. The vegetation and agriculture areas masking was carried out using the Normalized Difference Vegetation Index (*NDVI*), that for the PRISMA specific case is (B53-B35)/(B53+B35), where band 35 (RED) is centered at 679.48 nm, while band 53 (NIR) corresponds to 865.95 nm ("*NDVIcsiro*"; Laukamp et al., 2022) with *NDVIcsiro* > 0.13 masked out. Other interference factors (e.g., roads, the nearby exploration camp, bare areas under cultivation) were recognized visually, supported by higher spatial resolution satellite images and local large-scales maps, then masked using specifically designed *Regions of Interest* (*ROIs*) and excluded from further processing. Finally, a spatial subset was obtained before the mineral mapping.

Tab. 5.5 Mineral assemblage (in abundance order from XRPD-QPA analysis) and VNIR-to-SWIR continuum-removed spectral feature positions in nm. When differences occurred in a sample, both fresh and weathered sides were acquired. Abbreviations are explained in Table 5.3.

Sample ID	Mineral Assemblage	Acquired portion	Characteristic spectral features in VNIR (nm)	Characteristic spectral features in SWIR (nm)
JSMON2	Dol + Cal + Sm + Gth + Cph + A-FeHyOX	fresh side	950	1438 (weak), 1935, 2322
		weathered side	918	1430 (very weak), 1941, 2322
JSMON3b	Dol + Cal + Sm (tr.) + A-FeHyOX	fresh side		1050, 1270, 1414 (very weak), 1938, 2320
		weathered side	940	1298 (very weak), 1414 (weak), 1940, 2320
JSMAR4	Dol + Hz + Hm + A-FeHyOX	fresh side	945	1425, 1934, 2315
		weathered side	950	1429, 1931, 2296, 2392
JSMAR5	Cal + Dol + A-FeHyOX	fresh side	673 (weak), 970	1425, 1916, 2334
		weathered side	673 (weak), 970	1425, 1916, 2210 (very weak), 2350
JSMAR7	Cal + Gth + Jrs + A-FeHyOX	fresh side	676, 940	1440, 1940, 2303, 2334
		weathered side	670 (weak), 970	1442, 1939, 1670, 1770, 1937, 2337
JSMAR8	Hyd + Hm + Cal + A-FeHyOX		970	1405, 1967, 2300, 2375
JSMON H9	Cal + A-FeHyOX			1415, 1876-1995, 1755, 2158, 2338
JSMON13	Sm + Dol + Gth + A-FeHyOX		942	1434 (very weak), 1937, 2320
JSMON16	Cal + Gth + Hem + A-FeHyOX		667 (weak), 925	1443, 1762 (very weak), 1938, 2216 (extremely weak), 2339
JSMON18	Cal + Hem + Pb-Jrs + A-FeHyOX		670, 908	1416, 1924, 1672 (very weak), 1780 (weak), 1925, 2208, 2325
JSMON20	Gth + A-FeHyOX		670, 980	1437, 1680, 1778, 1941, 2300, 2401
JSMON23	Dol + A-FeHyOX	fresh side	916	1416 (very weak), 1938, 2320
		weathered side	680 (very weak), 916	1416, 1916, 2208, 2255, 2319
JSMON25	Gth + Cal + A-FeHyOX		668, 970	1437, 1940, 1675 (very weak), 1776, 1931, 2333 (very weak), 2405 (very weak)
JSMON29	Hyd + A-FeHyOX		962	1490, 1940, 2299, 2371
JSMON31	Gth + Hem + A-FeHyOX	fresh side	672, 963	1442, 1937, 1670, 1775 (weak), 2268 (extremely weak), 2410 (weak)
		weathered side	672, 963	1442, 1937, 1670, 1775 (weak), 2268 (extremely weak), 2410 (weak)
JSMON33	Dol + Cal + A-FeHyOX	fresh side	965	1414 (extremely weak), 1938, 2209, 2320
		weathered side	966	1438 (weak), 1937, 2322
JSMON39	Gth + Cal + A-FeHyOX		678, 1010	1443, 1941, 1680, 1777, 1936, 2335 (extremely weak), 2404

5.4.3 Hyperspectral mineral mapping

The feature extraction indexes technique adopted in this study assumes that the combination of a relatively small number of bands (wavelength) can outline the interaction between light and surface-exposed materials, extracting the wavelength position of specific absorption features exhibited by rock-forming and alteration minerals, regardless of the number of bands collected (Laukamp et al. 2021). Therefore, feature extraction indexes were applied to the PRISMA L2C subset scene for obtaining surface compositional information, while at the same time minimizing reflectance variations associated with topography and albedo effects (Clark et al., 1990b; Crowley et al., 1989). The band ratios used were adapted to the PRISMA hyperspectral data, avoiding bands dominated by strong instrument noise, to minimize along-track striping and improve the contrast of the remaining pixel values. The considered feature extraction indexes can be easily applied by using the Band Algebra Tool in ENVI.

We focused on interpreting/discriminating the dolomitization distribution in the Jabali area, mainly using the following band ratios (Tab. 5.2):

owing band ratios (Tab. 5.2):

$$2320D = \frac{R2298 + R2342}{R2320} = \frac{\mathrm{B145+B151}}{\mathrm{B148}} \quad (1)$$

$$2350D = \frac{R2327 + R2364}{R2349} = \frac{\mathrm{B149+B154}}{\mathrm{B152}} \quad (2)$$

where R is the reflectance value and B is the corresponding PRISMA spectral band (Gaffey, 1986; Haest et al., 2012a, 2012b; Laukamp et al., 2012). The 2320D index was obtained by dividing spectral bands indicating the specific dolomites and limestones absorption minima. The algorithm is referred to the depth of the dolomites' diagnostic absorption at 2320 nm. The index 2350D was introduced because the (1) output appears noisier. The index 2350D (2) is based on the 2349 nm feature. In the latter case, problems in delineating the dolomite distribution may arise when Mg-OH and Al-OH minerals-bearing rocks are also present because they are characterized by the 2350 nm absorption feature, which overlaps the absorption

caused by carbonates. Since distinction from these other minerals can be achieved by other features, e.g., the Al- di-octahedral sheet silicates (white micas and smectites) feature around 2200 nm, pixels with (2) values greater than 2.0 were masked out from further processing, then the 2200D index (Al-sheet silicate abundance "ASA"; Laukamp 2022; further developed based on Sonntag et al. 2012) was applied to the remaining pixels:

$$2200D = \frac{R2143 + R2229}{R2206} = \frac{\mathrm{B125+B136}}{\mathrm{B133}} \quad (3)$$

Pixels with (3) resulting values greater than 2.15 were masked out to better delineate the areas effectively characterized by the presence of dolomites using the ratio 2320D/2350D and evaluating compositional variation within dolomites.

The identification of the outcropping rocks dominated by Fe-oxy-hydroxides (i.e., gossans) and nonsulfides, instead, was obtained through the 900D relative depth index (Fe-oxyhydroxides abundance "*FOA*"; Laukamp 2022):

$$900D = \frac{R770+R962}{R908} = \frac{\mathrm{B44+B62}}{\mathrm{B57}} \quad (4)$$

A rainbow color scale was applied to all the mineral maps, where red indicates higher abundances and blue indicates lower abundances referring to the upper and lower stretching limits reported in Table 5.2. This also allows a quick comparison with the binary discrimination diagrams. To obtain the hyperspectral mineral mapping performance assessment, *ROIs* were created on the L2C PRISMA VNIR-SWIR image over the areas where the target lithology (i.e., dolomite, limestone, gossan) was recognized by the PRISMA-derived mineral mapping. Statistics were extracted from each *ROI* and then directly compared to the field-based spectra representative of each target phase resampled to the PRISMA hyperspectral resolution (as explained in sub-section 4.1), after continuum removal to normalize the spectra.

5.5 Results

5.5.1 Quantitative mineralogy (XRPD-QPA), geochemistry, and absorption properties at PRISMA spectral resolution of ground samples

The three main groups of analyzed samples (host rock, gossans, and Zn- ore samples) were characterized by distinct features when comparing their mineralogy (Tab. 5.3), geochemistry (Tab. 5.4) and reflectance spectra properties (Fig. 5.5 to 5.7; Tab. 5.5)

Host rock samples. The group comprises five samples characterized by dolomite and calcite as main phases, and minor alteration minerals and impurities, such as smithsonite, goethite and smectite (Fig. 5.5 and Tab. 5.3).

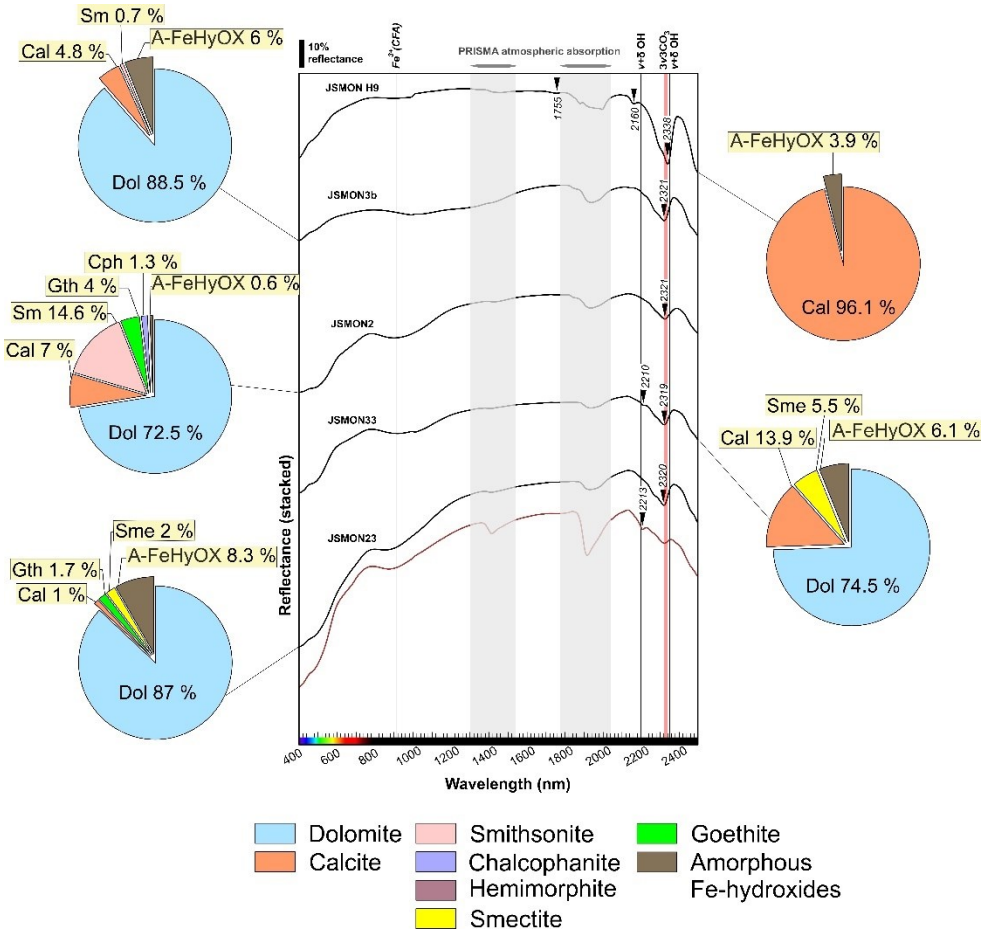

Fig. 5.5 Laboratory reflectance spectra downsampled to the PRISMA resolution in the VNIR-SWIR region, showing the spectral signatures for limestones and dolomites. For sample JSMON23 in red is shown the spectra acquired on the sample's weathered side. Pie charts showing the modal mineralogy of bulk samples obtained by XRPD-QPA are also shown for direct comparison. PRISMA spectral bands strongly affected by atmospheric absorption are marked at the top of the diagram and were excluded from mineral mapping processing. Abbreviations explanation in Tab. 3.

The chemical composition of host rock limestones is defined by CaO contents of 54.73 wt% and very low MgO (0.25 wt%) (Tab. 5.4). SiO_2, Al_2O_3, Na_2O, K_2O, and MnO contents are always lower than 0.6 wt%. Dolomite-dominated samples are characterized by CaO values ranging between 30.04 wt% and 26.14 wt%, while MgO contents vary between 18.59 wt% and 15.14 wt% (Tab. 5.4). Fe_2O_3 values range between 0.5 wt% and 3.64 wt%. JSMON3b is the only sample characterized

by a significant content of bivalent iron (FeO of 1.89 wt%; Tab. 5.4). Except for Cd, which is higher for sample JSMON2 compared to the other samples, and Ba, which reaches hundreds of mg/kg only in samples JSMON23 and JSMON H9, trace elements do not vary considerably for all the host rock samples and are generally negligible (Tab. 5.4).

Spectral signatures of limestones outcropping within the study area show a very pronounced CO_3-related absorption feature in the SWIR region at 2338 (limestone sample JSMON H9), with weaker features occurring at 2160 and 1755 nm (Fig. 5.5). The main CO_3 absorption feature, instead, appears shifted to shorter wavelengths in the dolomite spectra, with the main features occurring as variably deep absorptions around 2320 nm (Fig. 5.5). However, the same feature frequently appears shifted to longer wavelengths (between 2322 nm and 2324 nm) in almost all the samples, except for sample JSMAR4 (2320 nm). The left-hand asymmetry of the main CO_3 absorption feature, showing a shoulder on the short-wavelength side, is ubiquitously present in all the carbonate-bearing samples. Sample JSMON33 and the more weathered side of sample JSMON23 show the Al-OH feature at around 2210 nm, in the latter sample accompanied by a deepening in the water and hydroxyl-related feature (1416 nm and 1914 nm) (Fig. 5.5). The broad Fe-related absorption feature in the VNIR region for the dolomite-dominated samples, centered in the range from 900 nm to 950 nm, may be associated with goethite (when present) and/or Zn-Fe-bearing altered dolomites (CFA). An exception is the unaltered portion of sample JSMON3b, characterized by a shallower, but broader, absorption centered around 1000 nm to 1200 nm (a broad absorption doublet is more visible in the continuum-removed spectrum) due to Fe^{2+} contribution. Smectite (Zn-bearing smectite sauconite) occurring in sample JSMON33 (5.5 wt% from XRPD-QPA analysis) is visible at 2210 nm (Zn-OH and/or Al-OH feature) (Fig. 5.5). The contribution of water and hydroxyl-bearing material is ubiquitously represented by two variably deep absorption features close to 1900 nm and 1400 nm, which may, in some cases, appear shifted due to the occurrence of specific hydrous phases (Tab. 5.5).

Gossan samples. In these heterogeneous samples, goethite ubiquitously predominates, followed by calcite with lesser amounts of hematite (Fig. 5.6).

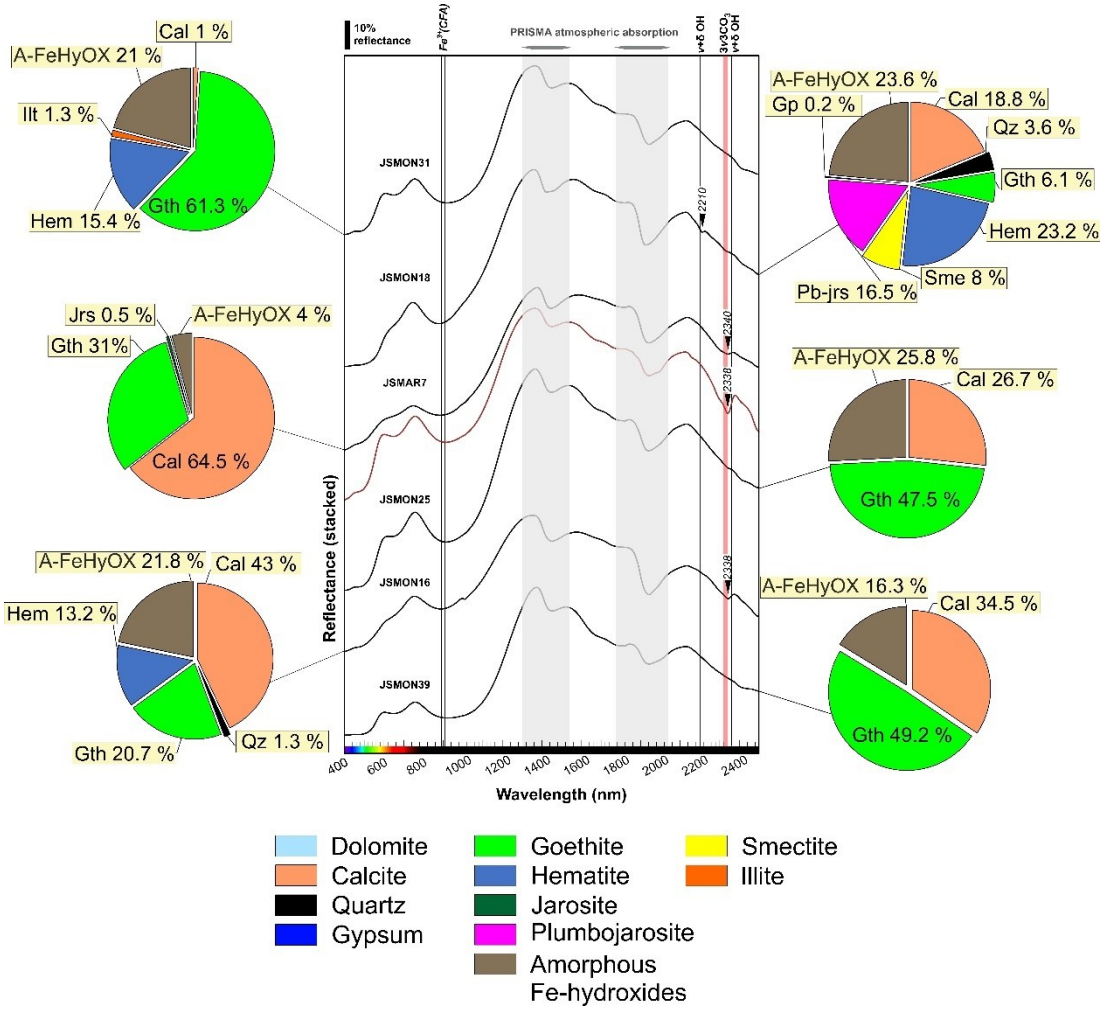

Fig. 5.6 Laboratory reflectance spectra downsampled to the PRISMA resolution in the VNIR-SWIR region, showing the spectral signatures for gossan samples. For sample JSMAR7, in red is shown the spectra acquired on the sample's weathered side. Pie charts showing the modal mineralogy of bulk samples obtained by XRPD-QPA are also shown for direct comparison. PRISMA spectral bands strongly affected by atmospheric absorption are marked at the top of the diagram and were excluded from mineral mapping processing. Abbreviations explanation in Tab. 3.

Quartz, K-Fe-Pb-bearing sulfates (jarosite and plumbojarosite) and kaolinite, gypsum, and Zn-bearing smectite were also observed in lower amounts (Fig. 5.6 and

Tab. 5.3), except for sample JSMON18, where plumbojarosite occurs up to 16.5 wt% and Zn-bearing smectite shows amounts of 8 wt%. The specimens from the gossan are marked by very high bulk Fe_2O_3 contents ranging from 78.9 wt% to 28.2 wt% (Tab. 5.4). SiO_2 values are generally between 2 and 3 wt%, except for sample JSMON18 (8.08 wt%), which is also characterized by significant Al_2O_3 values of about 4.5 wt% (Tab. 5.4). Calcite-bearing gossan samples are characterized by CaO values varying between 10.59 wt% and 36.04 wt% (Fig. 5.6; Tab. 5.3 and 5.4), with mean values of about 20 wt%. MgO contents are ubiquitously very low, showing mean values of 0.28 wt%, and always below 0.3 wt%. Variable ZnO contents were observed between 0.6 wt% and 3.7 wt%. PbO is generally low; contents of 6 wt% are shown by sample JSMON18, followed by sample JSMON16, which is characterized by PbO values of 3.23 wt% (mean values of about 2 wt%). The other gossan samples have very low PbO values (Tab. 5.4). Most variable trace elements observed in the samples from gossan zones are Cd, Cu, Ag, Ni, Cu, V, Ga, Co (Tab. 5.4). However, bulk concentrations reaching hundreds of mg/kg were only observed for Cd (mean 482 mg/kg Cd) in samples JSMAR7 and JSMON25, while it is always lower than about 70 mg/kg for all the other samples belonging to this group (Tab. 5.4).

The gossan samples dominated by goethite show the main absorption features at 660 nm (CTF) and 908 nm - 920 nm (CFA), except for sample JSMON18, where the CFA is slightly shifted to shorter wavelengths (878 nm) due to greater hematite content (Fig. 5.6). The CO_3 main feature occurs generally at around 2338 nm, but it is ubiquitously very weak due to the low calcite content, except for sample JSMAR7 and sample JSMON16, where calcite concentration is higher (Cal 64.5 wt%, and 43 wt%). Sample JSMON18, instead, is characterized by the presence of the Al-OH feature at 2210nm (Fig. 5.6) due to the higher presence either of plumbojarosite (16.5 wt%) and smectites (Sme 8 wt%).

Zn ore samples. In these samples, hydrozincite is the most abundant mineral, followed by hemimorphite, with lesser smithsonite and calcite, dolomite and goethite as gangue minerals (Fig. 5.7 and Tab. 5.3).

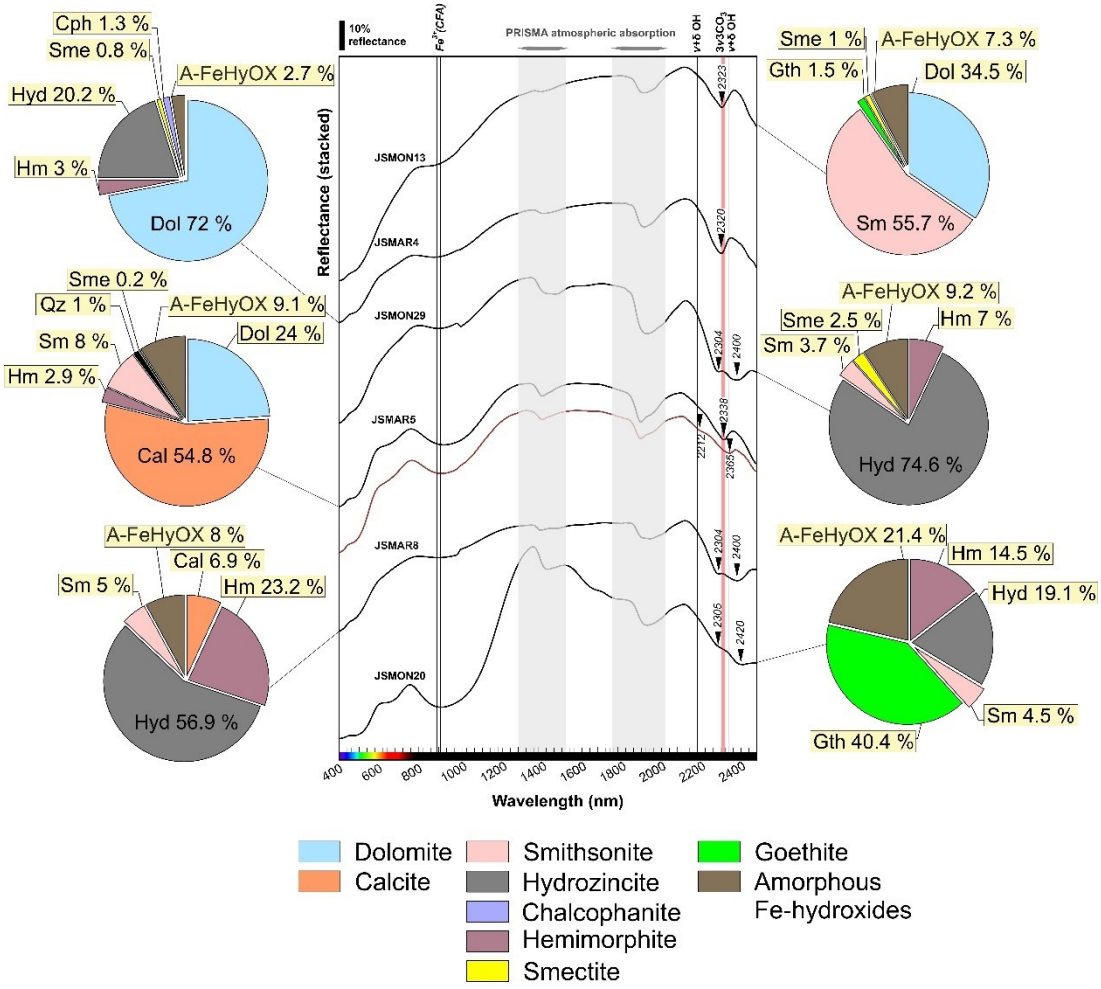

Fig. 5.7 Laboratory reflectance spectra downsampled to the PRISMA resolution in the VNIR-SWIR region, showing the spectral signatures for Zn ore samples. Pie charts showing the modal mineralogy of bulk samples obtained by XRPD-QPA are also shown for direct comparison. PRISMA spectral bands strongly affected by atmospheric absorption are marked at the top of the diagram and were excluded from mineral mapping processing. Abbreviations explanation in Tab. 3.

Goethite occurs in higher quantities in sample JSMON20 (40.4 wt%). The sample JSMON13, instead, is characterized predominantly by smithsonite (55.7 wt%) and dolomite (34.5 wt%), with goethite (1.5 wt%) as a minor phase, and smectite in

traces (1 wt%) (Fig. 5.7 and Tab. 5.3). Zn ore samples are characterized by bulk MgO and CaO concentrations up to 14.9 wt% and 37.3 wt%, respectively. SiO_2 is generally equal to or slightly lower than 2 wt%, except for sample JSMON20, defined by bulk SiO_2 contents of 4.4 wt%. ZnO concentrations are always higher than 20 wt. %, reaching bulk contents of 65.7 wt% (Tab. 5.4). PbO contents are generally very low and never higher than 0.81 wt%. Fe_2O_3 bulk contents observed are between 2.3 wt% and 6.54 wt% (mean values of 5.2 wt%), aside from sample JSMON20 (Fe_2O_3 of 50.9 wt%) (Tab. 5.4). Bulk Cd concentrations are high for all the samples belonging to this group (Tab. 5.4), showing values above the detection limit (2000 mg/kg) for the smithsonite and hydrozincite-bearing samples.

The smithsonite-hydrozincite-bearing samples are characterized by a broad absorption doublet at 2304 and 2400 nm (Tab. 5.3; Fig. 5.7), resulting from the overlapping of the CO_3 features of the two Zn-bearing carbonates, not allowing their clear distinction in any of the investigated samples. A very weak band at 2210 nm characterizes the altered portion (red spectrum in Fig. 5.5) of sample JSMAR5, which may be associated with the Zn-OH bond in hemimorphite (Fig. 5.5). A deep and broad absorption centered around 920 nm, instead, may be related to the presence of either Fe-oxy-hydroxides or Fe impurities. However, the sample JSMON20, characterized by goethite as the main phase (40.4 wt%), clearly shows the typical CTF and CFA features at 670 nm and 912 nm, respectively. The sample JSMON13, instead, is characterized by a smithsonite-dolomite ratio close to 1:1, it is only defined by a "rather" symmetric absorption band centered at 2323 nm (Fig. 5.7).

5.5.2 Relationships between spectral properties and ICP-MS/ES geochemical data of ground samples

The same feature extraction indexes applied to the PRISMA L2C scene were also used for describing the spectral behavior of the ground samples and colored using the variable in y-axes, to improve the comparison with the mineral maps (Figs. 5.8 a-f).

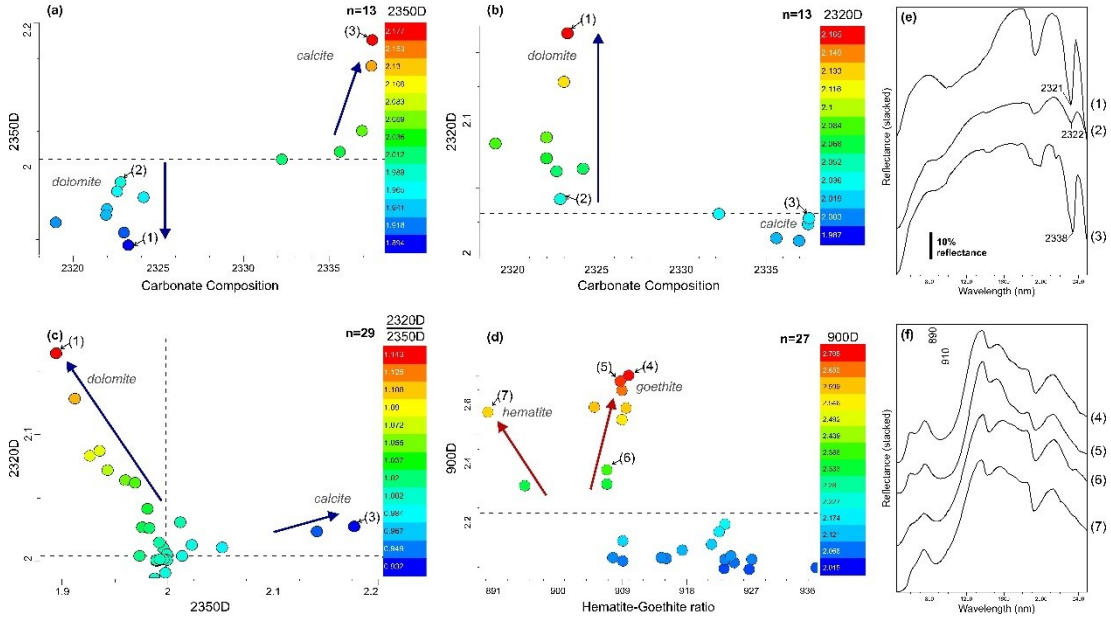

Fig. 5.8 Binary discrimination plots for the ground samples reflectance spectra dataset. (a) 2350D versus Carbonate Composition colored following the 2350D. Dolomite samples in blue are characterized by 2350D values lower than 2.0, while values above 2.20 are shown by limestones samples (orange-to-red). In green colors are shown the rusty and partially dedolomitized dolomite samples and the calcite-bearing gossan sample. (b) 2320D versus Carbonate Composition colored following the 2320D. The dolomite-bearing samples are shown as green to red samples points and placed above the 2320D threshold value of 2.02. Calcite-bearing samples plotted as light blue dots are characterized by 2320D lower than 2.02. (c) 2350D versus 2320D diagram, colored following the 2320D/2350D ratio. Dolomites samples (green to red dots) and limestones (blue dots) are negatively correlated, the distribution trends are indicated by the arrows. (d) 900D plotted against the Hematite-Goethite ratio. Gossan samples are characterized by values higher than 2.3. (e) spectra of representative host rock samples, (1) and (2) indicate decreasing dolomite content; (3) refers to limestone sample. (f) spectra of representative gossan samples order as decreasing

goethite content (4, 5, 6) and hematite (7). The numbers refer to their position in the binary diagrams. Arrows indicate increasing mineral abundances.

The same indexes were plotted against MgO, CaO, and Fe_2O_3 bulk concentrations and shown in Fig. 5.9 a-d. The 2350D was plotted against the Carbonate Composition script to characterize the occurrence and the compositional variations between the carbonate phases (Fig. 5.8a). The deeper relative depth of the spectral feature at around 2340 nm in calcite-bearing samples resulted in higher 2350D values (orange to red samples dots), while the dolomites form a cluster defined by lower values compared to limestones (blue samples dots). A threshold value of 2.0 is observed. The 2320D feature extraction script was used to better define the dolomites samples (diagnostic feature centered between 2322 nm and 2324 nm) and correctly evaluate their abundances. The dolomite-bearing samples place above the 2320D threshold value of 2.02, directly proportional to the dolomite content in the studied samples (green to red samples points in Fig. 5.8b).

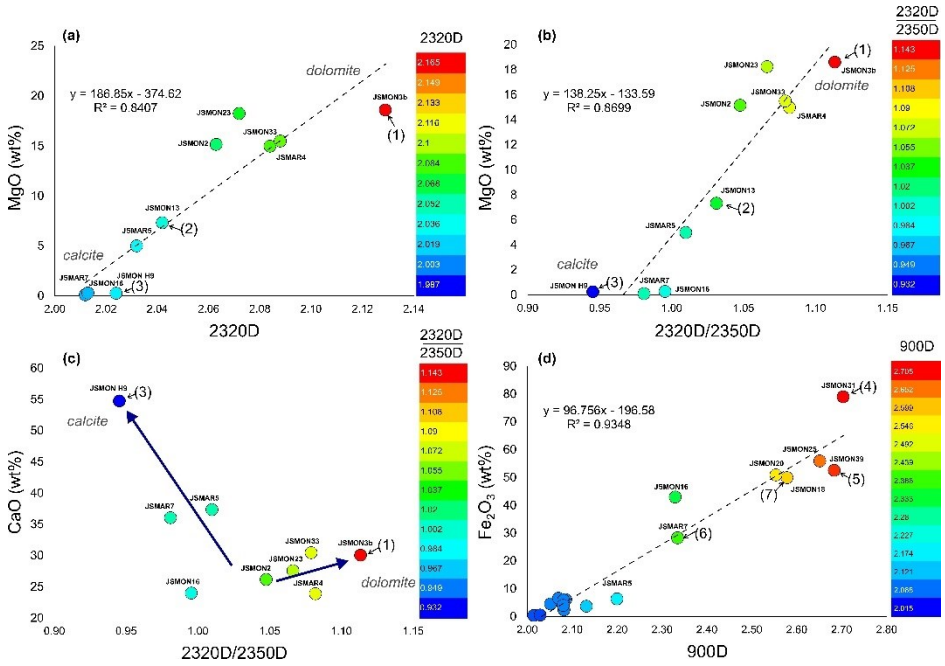

Fig. 5.9 Validation Binary plots reporting the integration with whole-rock geochemical data; (a) 2320D plotted versus MgO (wt%), colored following 2320D; (b) 2320D/2350D ratio plotted versus MgO (wt%), colored following 2320D/2350D; (c) 2320D/2350D ratio plotted

versus CaO (wt%), colored following 2320D/2350D; (d) 900D plotted versus Fe_2O_3 (wt%), colored following 900D.

Lower 2320D values (2.04) are observed for sample JSMON13, characterized by 34.5 wt% dolomite, while higher 2320D values are shown by sample JSMON3b (Dol 88.5 wt%). A positive correlation ($y=186.85x - 374.62$, $R^2 = 0.84$) is noticed for the bulk MgO (wt%) concentration. Dolomite samples show both higher 2320D and MgO (wt%) values (Fig. 5.9a). The 2350D and 2320D feature extraction scripts were plotted against each other (Fig. 5.8C) as they are negatively correlated. The binary discrimination diagram is colored by the ratio 2320D/2350D, which highlights the two resulting trends. The latter trends are indicated by arrows in Fig. 5.8c, discriminating both dolomites (green to red samples points in Fig. 5.8c, indicating higher 2320D and lower 2350D) and limestones (blues samples points in Fig. 8c; defined by lower 2320D and higher 2350D) and their increasing abundance. A very good correlation is shown by plotting the 2320D/2350D ratio values and the MgO (wt%) bulk concentrations in host rock samples ($y=138.25x - 133.59$, $R^2= 0.86$) (Fig. 5.9c). Two defined trends, instead, can be noticed by plotting the ratio against the CaO (wt%), where calcite-bearing samples place at high CaO (wt%) values and low 2320D/2350D (Fig. 5.9c). The gossan samples, instead, were analyzed through the 900D feature extraction script, plotted against the Hematite-Goethite ratio, to define their abundance in the analyzed samples and composition (predominance of either goethite or hematite in the samples), respectively (Fig. 5.8d). Gossan samples are defined by higher 900D values, shown by the green to red dots in Fig. 5.8d, placing above the threshold value of around 2.3. Goethite-dominated samples (diagnostic CFA absorption feature occurring between 905 nm and 909 nm) show an increase of the 900D values directly correlated with the goethite abundances obtained through XRPD-QPA analyses. Sample JSMON 31 (61.3 wt% Gth) is characterized by 900D values at around 2.8, while 900D close to 2.44 defines sample JSMAR7 (31 wt% Gth) (Fig. 5.8d). A shift to shorter wavelengths is observed for hematite-bearing samples, proportional to increasing hematite abundances (23.2 wt% and 13.2 wt%, respectively). As shown before for host rock samples, also the Fe_2O_3 (wt%) bulk

content for the analyzed samples is highly correlated with the 900D index ($y=96.756x - 196.58$, $R^2=0.93$) (Fig. 5.9d). In particular, the highest Fe_2O_3 (wt%) values were measured for goethite-dominated samples, which are also characterized by high 900D values.

5.5.3 Mineral maps obtained through hyperspectral satellite remote sensing

In Figures 5.10 a-c, and 11a, the band depth indexes proposed in this study, 2350D, 2320D, 2200D, and 900D are shown. In the 2350D mineral map (Fig. 5.10a), the distribution of dolomites and volcanic rocks outcropping in the study area is shown in blue, indicated by pixel values below the observed 2.0 threshold. Limestones are highlighted in red colors. In Fig. 5.10b, the 2320D/2350D ratio map shows in red the pixels that are defined by a strong 2320 nm feature depth, allowing a clear definition of the dolostones distribution within the study area, while limestones are characterized by lower values (shown in blue Fig. 5.10b).

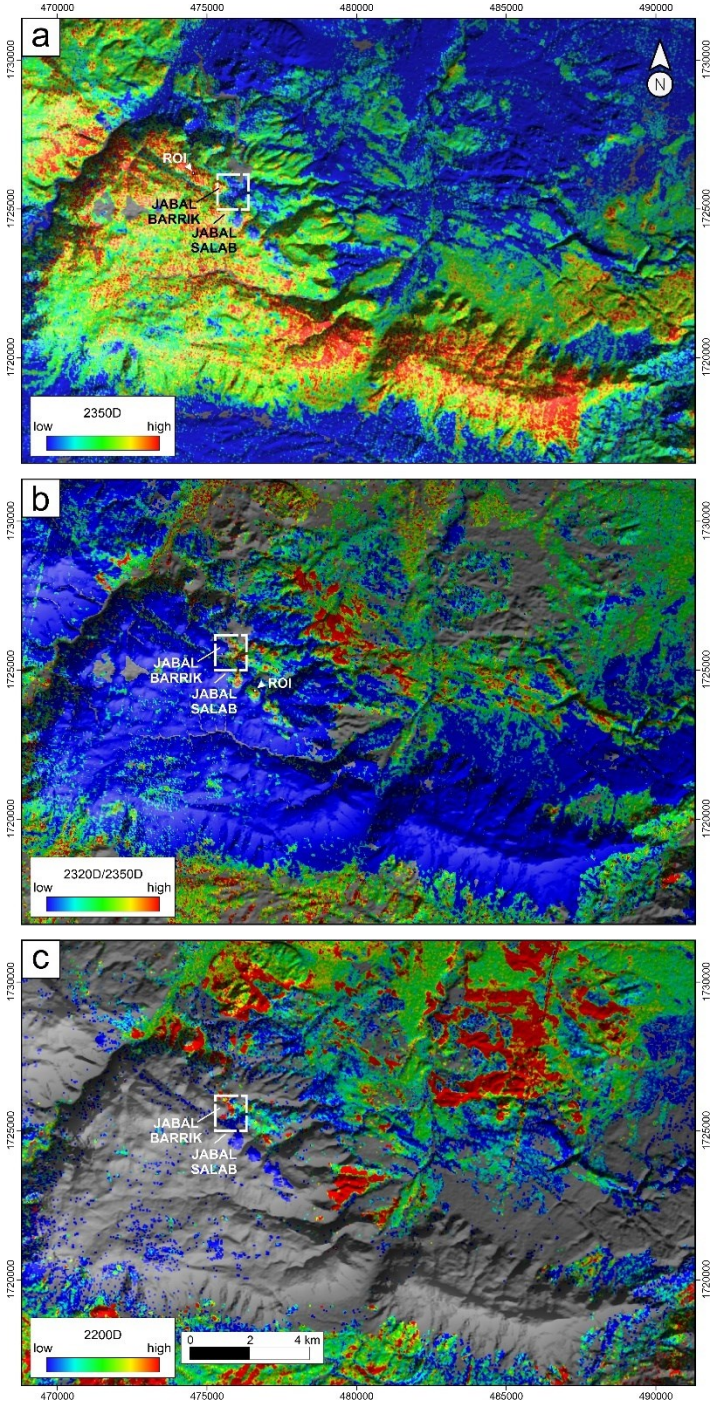

Fig. 5.10 Relative absorption depth indexes applied to the PRISMA L2C scene of the Jabali area: (a) 2350 nm feature depth (2350D) map masked for vegetation and man-made features; (b) 2320D/2350D ratio masked for 2200D>2.15. (C) 2200 nm feature depth (2200D) masked for 2350D>2.0, vegetation, and man-made features; Topographic shaded relief from SRTM

NASA Version 3 data (Farr et al., 2007; NASA JPL, 2013) is used as background. The borders of Figure 2 are reported as white dotted squares for localizing the Jabali area.

The 2200 nm feature depth map (2200D) is shown in Fig. 5.10c. The areas characterized by higher and lower relative abundances of Al-sheet silicates (micas) are highlighted in red (higher) and blue (lower). The 900D mineral map (Figs. 5.11a and b) shows in red the Fe^{3+}-bearing rocks, characterized by higher 900D values (Fig. 5.11a). The group includes the gossans outcrops, but also red beds and granite complexes. As the latter lithologies were identified also in the 2200D map, they could be excluded from further interpretation. The known gossan distribution was highlighted, together with possibly newly identified gossans a few kilometers E-NE from the Jabali prospect area (Fig. 5. 11b).

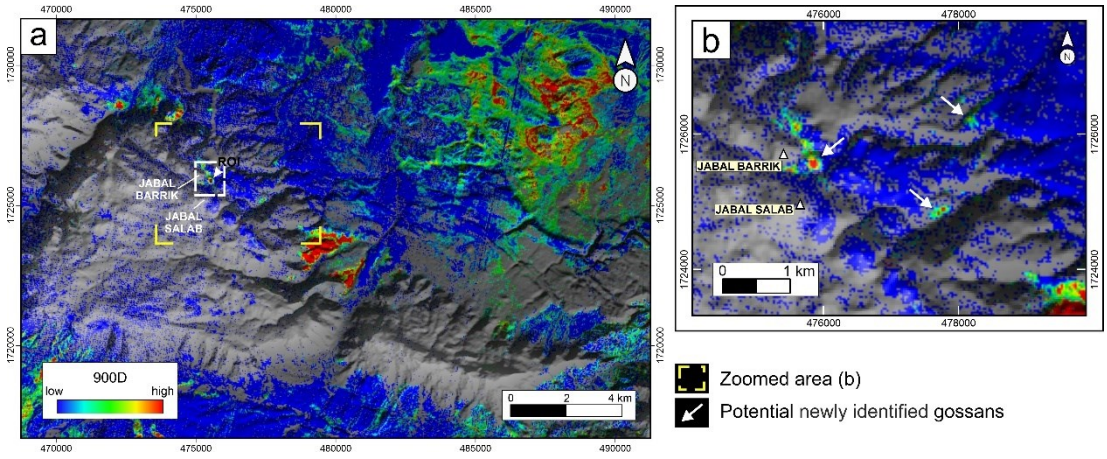

Fig. 5.11 (a) Ferric Oxides Abundance (900D) map and (b) a focus on the Main Area Of Interest. Topographic shaded relief from SRTM NASA Version 3 data (Farr et al., 2007; NASA JPL, 2013) is used as background. The borders of Figure 2 are reported as white dotted squares for localizing the Jabali area.

5.5.4 Comparison between PRISMA L2C results and field-based hyperspectral data

The spectra derived from the selected *ROIs* created on the PRISMA L2C VNIR-SWIR scene over the areas recognized as (a) dolomites (Fig. 5.10 b), (b) limestones (Fig. 5.10 a) and (c) gossans (Fig. 5.11 a) are reported in Fig. 5.12 a-c.

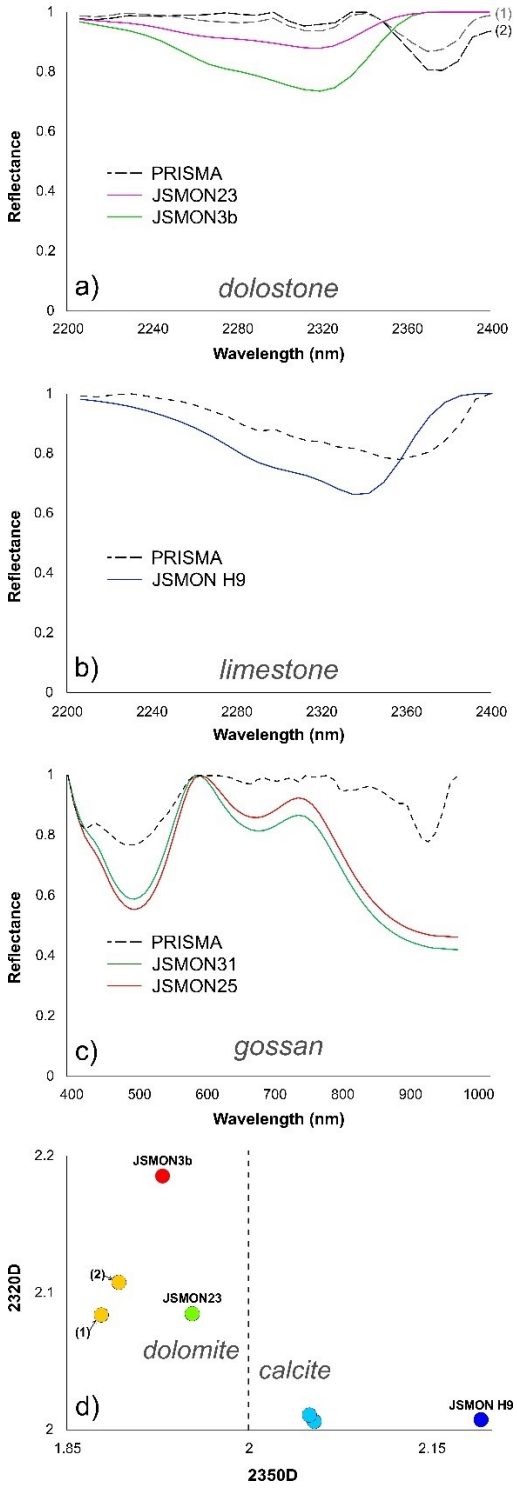

Fig. 5.12 Comparison between field-based representative spectra and PRISMA L2C. a) dolostones; b) limestones; c) gossans; d) 2350D versus 2320D validation binary plot, colored following the 2320D/2350D ratio. Only for field-based spectra, a label indicates the sample

number. Dolomites (green to red dots) and limestones (light blue to dark blue dots) spectra are negatively correlated.

In detail, Fig. 5.12 a-c shows the comparison between some representative field-based spectra downsampled to the PRISMA spectral resolution, and the spectra derived from the defined *ROIs* over the PRISMA image (black dotted lines). The intervals chosen are SWIR-2 (2200-2400nm) and VNIR (400-1000 nm). The spectral signatures generally appear consistent with those obtained from laboratory hyperspectral measurements. The differences visible may be due to PRISMA 30m-spatial resolution and mineral phases mixing compared to the spectra collected under laboratory conditions. However, a slight shift towards longer wavelengths (of about 7 nm) can be noted between the limestone spectrum (JSMON H9) and the PRISMA selected *ROIs* spectrum. The dolomite absorption feature, instead, is visible at 2320 nm in both the PRISMA spectra and the dolomite samples spectra. Regarding the gossan samples, Fe-hydroxides spectral features (CTF and CFA) are quite well visible, despite some distortions, due perhaps to non-absorption and absorption bands applied in the L2 processing for water columnar content assessment. Fig. 5.12 d, instead, shows the same spectra in Fig. 5.12 a-c after applying the 2350D and the 2320D band ratios, then plotted against each other and colored following the 2320D/2350D ratio in order to facilitate the comparison with the binary discrimination plots (see sub-section 5.5.2) and the mineral maps (see sub-section 5.5.3). As shown by the binary plot, the spectra derived from the PRISMA selected *ROIs* fall into the respective group (either dolomites or limestones), in agreement with the field-based hyperspectral data chosen for validation.

5.6 Discussion

5.6.1 Dolomite identification and mapping

Due to their spectral contrast, the distribution of the main rock types outcropping in the Sab'atayn basin, such as limestone, dolomite, Precambrian basement granites, and Tertiary volcanism products can be mapped using the workflow proposed in this study (Fig. 5.13a, b; see the simplified geological map for comparison Fig. 5.1b).

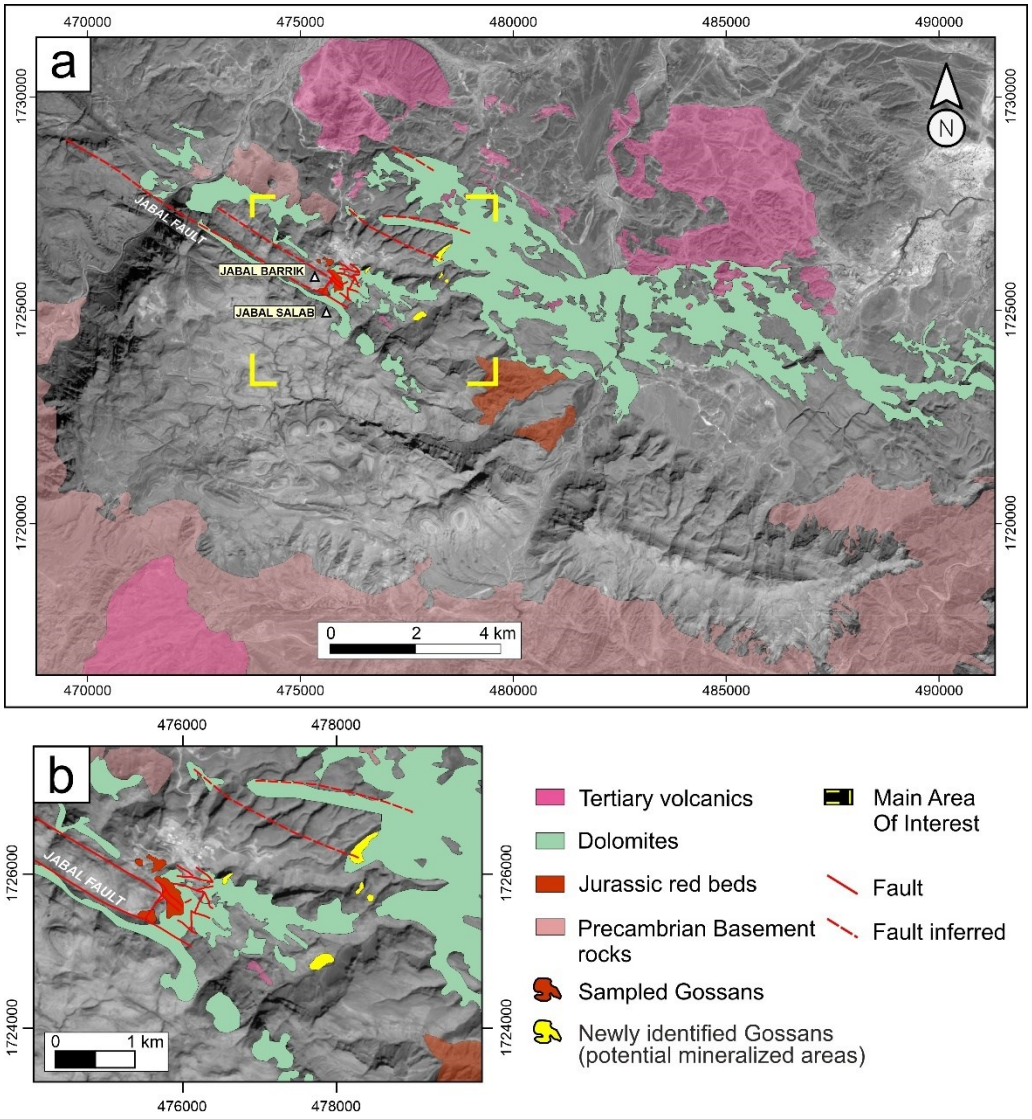

Fig 5.13 (a) Geological interpretation resulting from the band depth indexes and band ratio applied to the PRISMA L2C scene of the Jabali area and (b) a focus on the main area of interest. A subset of the PRISMA Panchromatic scene is used as background (pixel resolution 5 m).

In addition, by comparing the obtained PRISMA-derived spectral maps with the geological field data shown in previous studies (e.g., Christmann et al., 1989; Al-Ganad et al., 1994 and references therein), it is shown that PRISMA data also allows delineation of the alteration at regional scale, providing information about prospective zones for mineral exploration.

The distinction between dolomites and limestones was possible based on the main CO_3^{2-} absorption feature, which appears shifted to shorter wavelengths for dolomites, with the main feature occurring at 2320 nm (Gaffey, 1986; Lampinen et al., 2019), compared to the main calcite absorption feature located at 2335 to 2340 nm (Clark et al., 1990b; Kurz et al., 2012; van der Meer, 1995). Dolomite-dominated samples used for validation of the Jabali deposit area are characterized by dolomite abundances ranging from ~73 to 88 wt% (Fig. 5.5, samples JSMON3b, JSMON2, JSMON33, and JSMON23). Reflectance spectra from FieldSpec data show that most of them cluster between 2322 nm and 2324 nm (Figs. 5.5, 5.8a-c), shifted to longer wavelengths compared to the diagnostic wavelength position of stoichiometric dolomite at around 2320 nm, except for sample JSMAR4. When comparing both 2320D and 2350D feature extraction indexes with XRPD-QPA analyses, it appears that dolomite-dominated samples are characterized by an increase of the 2320D values, directly correlated with the dolomite abundances gained through XRPD-QPA analyses, while they are inversely correlated with 2350D values, which decrease with increasing dolomite abundances. On the contrary, calcite-bearing samples (both limestones and alteration samples) show an increase of the 2350D proportional to the XRPD-QPA calcite abundances (Figs. 5.5, 5.8a-c). When comparing the 2320D and 2350D feature extraction indexes with the whole-rock geochemical analyses, a positive correlation ($y=186.85x - 374.62$, $R^2 = 0.84$) is shown between the bulk MgO (wt%) concentration and the 2320D index, which is higher for samples with high MgO (wt%) values (Fig. 5.9a). A very high correlation ($y=138.25x - 133.59$, $R^2= 0.86$) was also obtained by comparing the 2320D/2350D ratio with the MgO (wt%) bulk concentrations in host rock samples. Moreover, two defined trends can be noticed by correlating the 2320D/2350D ratio against the CaO (wt%), where calcite-bearing samples (JSMON H9 and, secondly, JSMAR7 and JSMAR5) show high CaO (wt%) values and low 2320D/2350D (Fig. 5.9c). These relationships demonstrate the value of the 2320D and 2350D feature extraction indexes for the discrimination of limestone from dolomite.

As in several carbonate-hosted Zn-Pb deposits (e.g., Poland, USA, Ireland; Leach et al., 2005; Davies and Smith, 2006), the hydrothermal dolomite at Jabali is Fe- and Mn-bearing (containing up to 2 wt.% MnO and between 0.1 and 6 wt.% FeO). As outlined in previous studies (Gaffey, 1985, 1986; Green and Schodlok, 2016; Kurz et al., 2012; Lampinen et al., 2019), higher Mn and Fe contents can cause the shift to longer wavelengths of the main carbonate bands in dolomite spectra, however, a discriminator between Fe-carbonate species is the Fe^{2+} CFA feature, a broad double band in the NIR region centered at around 1200 nm. From hyperspectral analysis from hand specimens, the latter aspect is visible only in the slightly Fe-enriched dolomite in sample JSMON3b for which, together with the presence of a broad but weak absorption doublet around 1200 nm (Figs. 5.5, 5.8e and Tab. 5.5), the bulk FeO contents obtained from whole-rock geochemical analysis show values up to ~1.9 wt% (Tab. 5.4). Samples JSMON2, JSMON33, and JSMON23, instead, show FeO concentration always lower than the detection limits (i.e., FeO <0.20 wt%; Tab. 5.4) and are less pure, characterized by typical alteration products such as smithsonite and chalcophanite (JSMON2), goethite (JSMON2 and JSMON23) and smectites (i.e., sauconite; JSON33 and JSMON23; Fig. 5.5 and Tab. 5.5). At the same time, the latter samples show a broad absorption feature in the VNIR region at shorter wavelengths compared to ferroan hydrothermal dolomites (sample JSMON3b), centered from around 910 nm up to 940 nm (Fig. 5.5 and Tab. 5.5). The presence of this feature could be mostly related to the presence of goethite and/or amorphous Fe-oxy-hydroxides, which are characterized by the CFA feature occurring at around 908 nm (Crowley et al., 2003). However, the hydrothermal dolomite at Jabali also experienced later supergene alteration and formation of Zn-bearing dolomite (Mondillo et al., 2014), associated with the oxidation of Zn-Pb sulfide ores (Boni et al., 2011). Thus, the goethite-related absorption (Fe^{3+} CFA) in the dolomite samples could have been affected by a shift to longer wavelengths, potentially related to the presence of Zn^{2+}, similar to smithsonite which displays deep and broad crystal field effects between 800 nm and 1200 nm and centered around 960 nm (McConachy et al., 2007).

Regarding the satellite spectral mapping, dolomite feature-based distribution maps of the Jabali deposit area could be obtained from the successive application of the latter tested indexes targeting the relative depths and wavelength positions of the carbonate phases absorptions. The 2320D index and its relationship with the 2350D index applied to the PRISMA L2C scene allow the discrimination of dolomites from calcite-bearing outcrops/samples (Figs. 5.8a-c, Figs. 5.9 a-c, Fig. 5.10a, b). In the 2320D/2350D mineral map (Fig. 5.10b), limestones were highlighted in blue, and different dolomite types are characterized by shades of red (high relative abundances) to green (lower relative abundances). The spectra derived from selected *ROIs* (Figs. 5.12 a, b, and d) confirm and validate the accuracy of the mineral mapping.

The application of the 2200D index (Tab. 5.2 and Fig. 5.10c) and its combination with the 2320D and the 2350D indexes helped to discriminate silicatic lithologies related to magmatic activity (i.e., Tertiary volcanics and the Precambrian Basement), enabling their masking before mapping the dolomite distribution (Figs. 5.10b and 5.12a). In addition to these rocks, shown in red in Fig. 5.10c, it was noticed that the areas known from previous studies and fieldwork for the occurrence of hydrothermal dolomites are characterized by slightly lower 2200D index values (shown in blue in Fig. 5.10c), if compared to other areas mapped as dolomite from the 2350D/2320D ratio (Fig. 5.10b; green zones in Figs. 5.13a, b). Since higher 2200D values are related to a higher relative abundance of Al-sheet silicates, this feature could be due to the presence of micas and/or clays within the early diagenetic dolomite country rock (as also observed by Youssef (1998). Thus, the areas with dolomites (high 2320D/2350D) and low 2200D were interpreted as hydrothermal dolomites sensu stricto.

The main challenge in distinguishing between different dolomite types (i.e., hydrothermal, and early diagenetic) is related to the relatively low spatial resolution of the space-borne hyperspectral instruments (i.e., ~30 m, as in the PRISMA specific case), as well as to the lack of characteristic spectral features achievable from SWIR spectra able to differentiate the dolomite facies in the studied wavelength region. For

the Jabali case, the spatial resolution issue also affects the ability to differentiate the different carbonate units (Units 1 to 4), which are characterized by very small thicknesses (from 10 m to 40 m). Nevertheless, Kurz et al. (2012), who proposed a workflow combining ground-based hyperspectral imaging and lidar data for differentiating limestones from dolomites and characterizing also diagenetic and compositional features, achieved the results by using much higher spatial resolved hyperspectral data collected from a tripod-mounted sensor (HySpex SWIR-320m imager). Lampinen et al. (2019), instead, evaluated the use of the Fe^{2+} CFA feature for discriminating between dolomite, siderite, and Fe-dolomite (+ankerite) from TIR trained SWIR drill core hyperspectral data. Good results were gained by applying the Fe^{2+} intensity scalar based on the measure of the depth of the Fe^{2+} reflectance absorption feature at ~1200 nm. A band ratio for Fe^{2+}-bearing minerals identification, including carbonates, and always based on the Fe^{2+} CFA feature, was proposed and successfully applied in previous studies to airborne hyperspectral data (Cudahy et al., 2008), e.g., the commercial HyMap system, equipped with a VNIR-SWIR spectrometer collecting 126 spectral bands at 3 to 10 m spatial resolution (depending on flying acquisition height). Potentially, a higher Fe^{2+} content in ore-related hydrothermal dolomites, compared to the one observed for the Jabali dolomites, could enable to use of the same bands for discriminating Fe-rich dolomites from Fe-poor dolomites even from satellite hyperspectral data, assisting the mineral identification and mapping even at the PRISMA spatial resolution, allowing the delineation of the ore-related alteration haloes from the barren diagenetic dolomite rocks.

5.6.2 Delineation of gossans and mineralized outcrops

The gossan samples analyzed in this study (Tab. 5.3, sampling areas 2, 3, 4, 5, 7 and Jabal Salab in Fig. 5.2) are dominated by goethite and hematite, displaying the main absorption features at 660 nm (CTF) and 908 nm to 910 nm (CFA) when goethite dominates, and the CFA shifted to shorter wavelengths (878 nm) when hematite occurs in higher amounts (e.g., sample JSMON18; Fig. 5.6). Moreover, the OH-related feature characteristic of a sufficient presence of jarosite, plumbojarosite, and

smectites is also visible in some samples (e.g., JSMON18; Fig. 5.6). The feature used for mineral mapping was the one at around 900 nm. As shown in Figs. 5.8d and 5.9d, it can discriminate all the gossan samples analyzed. The 900D was applied to the whole samples hyperspectral dataset and plotted against the Hematite-Goethite ratio (Cudahy and Ramanaidou, 1997) and the bulk Fe_2O_3 concentrations. It indicates that gossan samples are defined by higher 900D values (Fig. 5.8d), and both goethite- and hematite-dominated samples display an increase of the 900D values directly correlated with the goethite/hematite abundances obtained through XRPD-QPA analyses. A highly positive correlation is also shown in Fig. 5.9d, where higher Fe_2O_3 (wt%) bulk contents correspond to high 900D values (y=96.756x – 196.58, R^2=0.93). Figs. 5.11 a and b illustrate the application of the 900D to the PRISMA L2C scene, after masking pixels with 2350D<2.0. In the resulting mineral distribution map (Figs. 5.11 a, and b), the known gossan outcrops are highlighted, but new gossans (i.e., new potential mineralized areas) were also identified (in yellow in Figs. 5.12a and b), a few kilometers E-NE from the Jabali prospect area (Figs. 5.11b, 5.12a and b).

With regards to the Zn-nonsulfides samples hyperspectral characterization, the smithsonite-hydrozincite bearing samples (JSMON29 and JSMAR8, Hyd > 20 wt%) are defined generally by broad absorption doublets at 2304 and 2400 nm (Fig. 5.7). Hemimorphite occurrence is, instead, commonly characterized by the Zn-OH bound displaying a very weak absorption at 2210 nm (JSMAR5, red spectrum in Fig. 5.7), however, it occurs only in minor amounts in the studied samples. When either Fe-hydroxides (both goethite and amorphous phases) or Fe impurities are present, deep, and broad absorptions centered around 920 nm occur, summed to the contribution of Zn^{2+} in the same range. The overlapping of the CO_3^{2-} features of calcite, dolomite, and Zn-bearing carbonate phases (i.e., smithsonite and hydrozincite) limits their clear distinction in the SWIR 2 region in any of the investigated samples (Fig. 5.7) due to mineral phases mixing. However, the ubiquitous presence of the broad absorption doublet when hydrozincite occurs in significant amounts in the mineral assemblage

could be very useful for discriminating Zn-bearing nonsulfide phases from secondary calcite by employing portable hyperspectral instruments in the field.

An additional factor that can assist during the geo-mineralogical interpretation of hyperspectral maps is the possible association of hydrothermal-mineralized facies with tectonic structures (e.g., fractures and faults). In the Jabali case, for example, the hydrothermal alteration and the related mineralization at Jabali are preferentially located along faults and at their intersection following three main structural trends recognized in the field, associated with boundary faults at the flanks of basement highs (Figs. 5.1 and 5.2; Mondillo et al. 2014). Looking at Figures 5.12a and b, it is possible to see that the main targets in the Jabali area are defined by gossan occurrences in dolomites (identified through hyperspectral satellite imagery processing), and the position of main structural lineaments.

5.6.3 PRISMA capabilities in mineral mapping

The PRISMA surface reflectance data collected in the area appear to be suitable for mapping the target mineral phases in both the VNIR (around 900 nm) and SWIR 2 (between 2000 nm and 2400 nm) wavelength regions. In particular, the SWIR detector provides 174 spectral bands between 920 and 2500 nm, at an SNR ≥100 at wavelengths larger than 2000 nm (Cogliati et al., 2021). Compared with previous studies based on remote sensing applications in the Jabali region (Deroin et al., 2012, 2011), where the use of Landsat (MSS, TM, ETM+), QuickBird, and ALOS AVNIR-2 multispectral satellite data led to a quite detailed mapping of the area, the narrower bands of the PRISMA SWIR 2 represent a more effective tool for discriminating SWIR-active spectrally similar minerals, like dolomite and calcite. Deroin et al. (2011, 2012) obtained a good identification of gossans possibly related to archeological remains, but carbonate species discrimination was only based on the broad 30m-SWIR 2 band 7 of Landsat (2.08-2.35 μm) and, therefore, it was less accurate due to poor coverage of the SWIR region. As shown in Figs. 5.12 a, b, and d, except for a slight shift of the 2340-2342 nm calcite main feature (of ~7 nm), both dolomite and limestone are defined by the PRISMA spectra and are in agreement with the field-based hyperspectral data collected for validation and the geological

features described in the area (Figs. 5.1b, 5.2). A shift of the calcite absorption feature was already encountered by Heller Pearlshtien et al. (2021). However, Heller Pearlshtien et al. (2021) observed a significant shift (29 nm versus ~7 nm observed in this study), resulting in higher inaccuracy in mapping. The authors explained the issue to be related to artifacts introduced for SWIR-2 long-wavelengths higher than 2340 nm by the L2D atmospheric correction process developed by ASI, and it was minimized by the same authors correcting radiance data instead of using L2D At-surface reflectance products. Therefore, even if the shift observed in this study is not so significant, and the limestone mapping, as well as its distinction from dolomites, could be performed by using the 2349 nm PRISMA band (B152 of the SWIR cube), the results can possibly even improve by using L1 data instead of applying the feature-based band ratios on already processed L2 images.

Due to the careful user-guided evaluation of the PRISMA bands before proceeding with the mineral mapping, the PRISMA-derived spectral maps appeared only slightly influenced by the striping effect, which represented the main issue for some specific and diagnostic absorption bands and spectral regions in mineral mapping. Generally, they are noticeable in the form of noisy bands with along-track lines with no spectral information and other noise distortions that, for the PRISMA scene from the Jabali area, are characterized by some of the bands used for the 2320D and the 900D indexes. The accuracy in the detection of the geological features of the area was only negligibly impacted since it is covered with hardly any green and dry vegetation which may contribute to mixing effects (Cudahy et al., 2008).

5.7 Conclusions

The results of this study illustrate the advantages of using feature extraction indexes applied to hyperspectral data for the recognition of outcropping geology, which can be used as a powerful tool for mineral exploration in sedimentary environments at regional scale. Since the understanding of the mineralogical and geochemical features in both country rocks and weathering profiles is crucial for enabling successful exploration, we adopted a combined use of remote and proximal sources of hyperspectral data for defining features possibly able to target carbonate-hosted

Zn-Pb ore deposits. The VNIR-SWIR reflectance spectroscopic data derived from the PRISMA satellite, which were interpreted with the support of analyses on ground samples, allowed us to (1) delineate the distribution of the dolomitization in the Jabali area, enabling its discrimination from limestones, and (2) identify the gossan outcrops overlying the mineralized areas. The detailed evaluation of the reflectance spectra from mineralized samples, even if their distribution mapping is not achievable at the satellite spatial resolution, helped the definition of the spectral responses of Zn(-Pb)-bearing oxidation-related minerals. Since they are commonly associated with nonsulfide ores related to supergene alteration of sulfide ore bodies, they represent a useful tool for exploration surveys based on field spectroscopy.

In conclusion, this study demonstrates that PRISMA can be a valuable tool for mineral exploration. The proposed method could be potentially applied to other hydrothermal ore deposits in sedimentary environments, including sedimentary-exhalative (SEDEX) Pb-Zn ores, hypogene willemite nonsulfide deposits (e.g., Vazante district, Beltana, and Berg Aukas deposits; Hitzman et al. 2003), as well as many hydrocarbon reservoirs (Davies and Smith, 2006). Each of the latter systems displays a strong structural control by extensional and/or strike-slip (wrench) faults, typically acting as preferential paths for fluid flow and controlling the hydrothermal alteration of country rocks. An extension to other spectral ranges (e.g., Thermal InfraRed – TIR) can also be considered, applying the method proposed to other case studies and systems defined by VNIR-SWIR non-active alteration minerals and lithologies. Distinguishing diverse dolomite types (i.e., hydrothermal vs. early diagenetic) has not been solved in the current study using PRISMA, mostly due to limitations in the satellite spatial resolution. More investigation is necessary to develop and improve methods for noise suppression (e.g., de-striping) for some wavelength regions of the PRISMA data.

Chapter 8:

Application of multispectral remote sensing for mapping flood-affected zones in the Brumadinho mining district (Minas Gerais, Brazil)

8.1 Introduction

On the 25th of January 2019, the tailing dam called "Dam B1" of the Córrego do Feijão Mine (Brumadinho Iron Mine), one of the upstream iron tailing dams located around 9 km east of Brumadinho, Minas Gerais, Brazil, collapsed. The catastrophic failure was considered one of the largest environmental disasters in the World (Vergilio et al., 2020), and caused a huge flood consisting of more than 11 million m^3 of mining waste spreading about 10 km downhill, that destroyed mining offices, houses, roads and resulted in a tragic loss of lives, with 259 people died. The polluting flood reached quickly the Paraopeba River: a major tributary of the São Francisco River–one of the largest rivers in Brazil. The flood affected decisively 249.5 thousand m^2 of the surrounding area, impacting seriously the local flora and fauna and the Paraopeba River aquatic system but also involving the vegetation and agriculture areas (Silva Rotta et al., 2020; Thompson et al., 2020). As a result, human, and social consequences, including water supply in the municipalities, tourism, and agriculture economy, were seriously compromised (Vergilio et al., 2020). According to Vergilio et al. (2020) the flood event has produced an increase in Paraopeba river turbidity levels due to the high amount of fine flood material, mainly composed of silt-clay particles and higher contents of Fe and Mn. The water analysis has indicated total heavy metals values up to 21 times above the acceptable, representing risks to the ecosystem (de Minas Gerais and do Brasil, 2019). The environmental impact after the Brumadinho dam disaster has also caused several issues for the surrounding lands. The presence of metals, including iron, aluminum, and manganese, was registered in the affected and unaffected soil samples with values above the acceptable thresholds (Furlan et al., 2020). Even though the Brumadinho tailing dam stability has been subject to local systematic monitoring, it collapsed only three years after the end of mining operations. This was due to water

accumulation and infiltration through the dam, causing the increase of moisture contents and saturation of the tailing dam. In this contest, the acceleration of the seepage erosion and internal liquefaction processes caused the weakening of the structure of the dam ending in the collapse (Silva Rotta et al., 2020). Investigation about surficial displacement and subsidence rate measuring during the period before the Dam B1 disaster (2016-2019) has been subjected to several studies based on remote sensing techniques and satellite data (Ammirati et al., 2021; Du et al., 2020; Holden et al., 2020; Silva Rotta et al., 2020), such as Advanced Differential Interferometric Synthetic Aperture Radar (A-DInSAR) analysis. These investigations revealed that before the collapse, deformations of the body of the dam started on the eastern side and progressively developed with higher values in the central zone, in relationship with anomalous rainy seasons (Ammirati et al., 2021). The current study aims to map and assess the land cover affected by the flood due to dam failure by using multispectral satellite data. Spectral sensing quickly allows classifying materials exposed at the Earth's surface based on their mineralogy and chemical properties (van der Meer et al., 2014; van der Meer et al., 2012), in this case making it easier to evaluate the effective area covered by the flood and to investigate the evolution of land properties after the disaster (Aamir et al., 2021; Gläßer and Reinartz, 2005; Kasmaeeyazdi et al., 2022; Sharma et al., 2022; Yan et al., 2022). To pursue this aim, we used Sentinel-2 images obtained from the Europe Space Agency of the Copernicus Program. The potential of multispectral remote sensing, and more specifically the use of Sentinel-2 imagery, for geological applications and mine waste monitoring has been widely studied (Ge et al., 2020; Mielke et al., 2014; van der Werff and van der Meer, 2015), mainly referring to the VNIR Sentinel-2 bands for the detection of ferric oxides and hydroxides. In fact, if compared to other multispectral satellites commonly used in the geology field, Sentinel-2 provides several relatively narrow bands in the VNIR region of the electromagnetic spectrum (van der Werff and van der Meer, 2015), i.e., band 4, band 8/8A, and band 9 of Sentinel-2 (Ge et al., 2020; Mielke et al., 2014; van der Werff and van der Meer, 2015) (centered at 665 nm, 842/865 nm, and 940 nm, respectively), which fit with the Iron-bearing oxides and hydroxides diagnostic spectral features associated with

the electronic transitions involving Fe^{3+} (Crowley et al., 2003; Cudahy and Ramanaidou, 1997). Here below we first describe the geology, mineralization, and spectral proprieties of the investigated areas. Then a short description of the data and the multispectral images processing methods is followed by discussion and conclusions.

8.2 Geological setting

The Córrego do Feijão mine is located along the ENE–WSW-striking Serra do Curral syncline, in the northwest portion of the so-called Quadrilátero Ferrífero (QF) area, located on the southern border of the São Francisco craton in the central portion of the Minas Gerais State (northern Brazil) (Figure 8.1). The Serra do Curral is the host of several iron ore deposits where, together with the Córrego do Feijão mine, the main are the West-, Central-, and East-Mine of the Usiminas mining complex, the Esperança, Jangada and the now exhausted Águas Claras ore deposits (Hensler et al., 2015). The geology of the QF is characterized by the metavolcanic greenstone belt sequence of the Rio das Velhas Supergroup (Chemale et al., 1994; Dorr, 1969), and by the Archean granite-gneiss domes, which border the metasedimentary units of the Minas Supergroup preserved as synclinal keels (Hensler et al., 2015).

The Minas Supergroup (Siderian to Rhyacian) unconformably overlies the Rio das Velhas Supergroup and is divided into the Caraça, Itabira, Piracicaba and Sabará Groups (Alkmim and Marshak, 1998; Cabral et al., 2012; Dorr, 1969; Guimarães, 1935; Klein and Ladeira, 2000). The Paleo-(Statherian) to Mesoproterozoic metasedimentary rocks Espinhaço Supergroup and the post-Minas intrusive rocks (i. e. the Borrachudo granite; (Baltazar and Zucchetti, 2007; Rosière and Chemale, 1996) represent the younger sequences in the QF area. Two orogenic events affected the area, (1) the Paleoproterozoic Transamazonian orogeny (2.1–1.9 Ga), which caused the uplift of the crystalline basement and folding of the Rio das Velhas and Minas Supergroups, and (2) the Neoproterozoic Brasiliano orogeny (0.8–0.6 Ga), which resulted in complex structures superimposed to the previous deformation, leading to the development of a W-verging thrust belt, especially in the eastern portion of the QF (Hensler et al., 2015). Metamorphic grades vary from west to east:

greenschist-facies with martite-granoblastic hematite ores characterize the western domain (low-strain domain), while amphibolite-facies with micro-platy and specular hematite ores occur in the central and NW parts (high-strain do-main) (Herz, 1978; Pires, 1995; Renger et al., 1994).

High-grade hypogene and supergene iron ores are mostly hosted by the Cauê Formation itabirites (Neoarchean - (Cabral et al., 2012); or Paleoproterozoic - (Babinski et al., 1995), basal unit of the Itabira Group (Minas Supergroup), consisting of up to 300 m-thick metamorphosed BIFs with sericitic and dolomitic phyllites and marbles intercalations. The mineralization is mainly characterized by veins cross-cutting the above-mentioned metamorphosed iron formation (itabirite) of the Itabira Group (Lüders et al., 2005). Itabirites of the QF have been divided into three different types: (1) quartz-itabirite, composed of recrystallized quartz and iron oxides in alternated bands (Dorr, 1969; Hensler et al., 2015; Spier et al., 2003); (2) dolomite-itabirites, characterized by carbonates-rich layers with hematite micro-inclusions, iron oxides and less quartz (Hensler et al., 2015; Rosière et al., 2008); and (3) amphibolite-itabirites, that are defined by red carbonates and/or iron oxides with less quartz, similar to the dolomite-itabirite, besides of disseminated amphiboles (Dorr, 1969; Guild, 1953; Pires, 1995). The supergene alteration, which occurred mainly in Paleogene, resulted in the development of a deep weathering profile where goethite is present as the main phase, occurring as alteration rims and porosity-filling replacing former Fe-oxides (Hensler et al., 2015, 2017).

8.3 Main features of the Brumadinho tailing Dam B1: structure and geochemical characterization

The 86 m-high dam was built in 1976 by Ferteco Mineração using the upstream heightening method and was active until 2015 under operations conducted by Vale S/A. The upstream method consists of building vertically the dam and depositing the tailings through successive uphill accumulation (de Minas Gerais and do Brasil, 2019; Silva Rotta et al., 2020). The construction starts with an embankment where the tailings are discharged from the crest of the starter dam and form the first level. This is compacted and then used to form the foundation for subsequent levels of the

wall as the dam is raised. As such, the crest of the dam moves up-stream with each raise (de Minas Gerais and do Brasil, 2019; Furlan et al., 2020). According to Furlan et al. (2020), the diffusion of this old type of dam is related to economic advantages, as it is the cheapest building method, as well as occupies a smaller area compared to the conventional downstream model, resulting in constructing licenses easier to obtain (Silva Rotta et al., 2020). However, the upstream method is considered very dangerous and unsafe (De Minas Gerais, 2019), due to the increasing instability after operations stop and dam deactivation (Silva Rotta et al., 2020). The geochemical characterization of the waste material of the Córrego do Feijão mine released from the Brumadinho Dam B1 collapse (Vergilio et al., 2020) revealed that the iron ore tailings are composed, amongst other elements, of Fe (26.5 wt.%), Al (1.1 wt.%), Mn (0.5 wt.%) and Ti (0.043 wt.%), contained in fine particulate material characterized by ~30% sand and ~70% silt-clay fractions, products of the wet processing method used to classify and purify the iron ore. Mineralogical characterization carried out on iron ore tailing dams from similar mines within the Quadrilátero Ferrífero area (i. e. Fundão Dam, Samarco mining company; (Almeida et al., 2018) showed that the mine waste mainly consists of quartz and hematite, as main phases, and kaolinite, goethite, and gibbsite present in minor amounts (Almeida et al., 2018; Souza et al., 2021). Fe-bearing phases (hematite/magnetite and associated goethite) are classified as ultrafine (about 76 % of their particles occurring in the range between 37μm and 6μm) and totally free (up to 88% of the particles) material (Souza et al., 2021).

8.4 Methods of study

The present study is based on multispectral products acquired by means of the Sentinel-2 Instrument (Multi-Spectral Image - MSI) of the European Space Agency. The available images from 2019 to 2021 with cloud coverage <5% were processed. In particular, we focused on the months: January 2019, August 2020, and July 2021. The orthorectified Level-2A Bottom-Of-Atmosphere (BOA) reflectance product has been used. In order to obtain a map of the affected flooded areas, the images were selected including the Minas Gerais mining district and covering a period before and after the Dam B1 failure. The thirteen Sentinel-2 bands and their combinations in the visible, Near-Infrared (NIR), and Short-wave Infrared (SWIR) spectral domains,

served as proxies for identifying geologic features (van der Meer et al., 2014), mainly for studying the ferric iron, ferrous iron, laterite, gossan, ferrous silicate, and ferric oxides products. The Sentinel-2 data were very useful for studying the iron-bearing minerals because of their spectral absorption in the VNIR region (bands 6, 7, 8, and 8A), particularly regarding the narrow band 8A, centered at 865 nm (21 nm band width) (Ge et al., 2020) (Figure 8.2). The bands were resampled to the spatial resolution of band B2 (10m) so that all pixels of other bands with 20x20 m^2 pixel size were loaded. The main aim of the MSI processing techniques adopted in this study was to apply several steps for mapping the flood-affected zones. The work was carried out by using the Sentinel Application Platform (SNAP) developed by European Space Agency (ESA), and the tool called Spectral Unmixing. The materials on the surface are characterized by their own diagnostic spectral properties, called endmembers, and the fractions of each material composing a mixed pixel refer to fractional abundances. The spectral unmixing tool uses the decomposition of reflectance source spectrum into endmember selected. The result of the spectral unmixing is a measure of the contribution of the individual endmember to the source spectrum. This measure is related to endmember's relative abundance. Through the identification in the pre-event map of materials of interest with a spectrally unique signature, that are the so-called principal elements, and of their endmember spectral signatures, the abundance maps were calculated. Therefore, if 30% of a pixel contains the endmember X, 20% of the pixel contains Y, and 50% of the pixel contains endmember Z, the spectrum for that pixel is composed by the sum of 0.30, 0.20, and 0.50 times the single spectra of relative endmembers X, Y, Z. The fully constrained algorithm is used to obtain the sum of abundances equal to 1 and eliminate the values below zero. An RGB color composite map can be produced, assigning the X, Y, and Z abundances, respectively red, green, blue. For the aims of this work, after the visual analysis of the pre-failure dam image, collected on the 11th of January 2019, we selected as possible principal elements: the water, vegetation, and the tailing dams and mining areas (Figures 8.1 and 8.2).

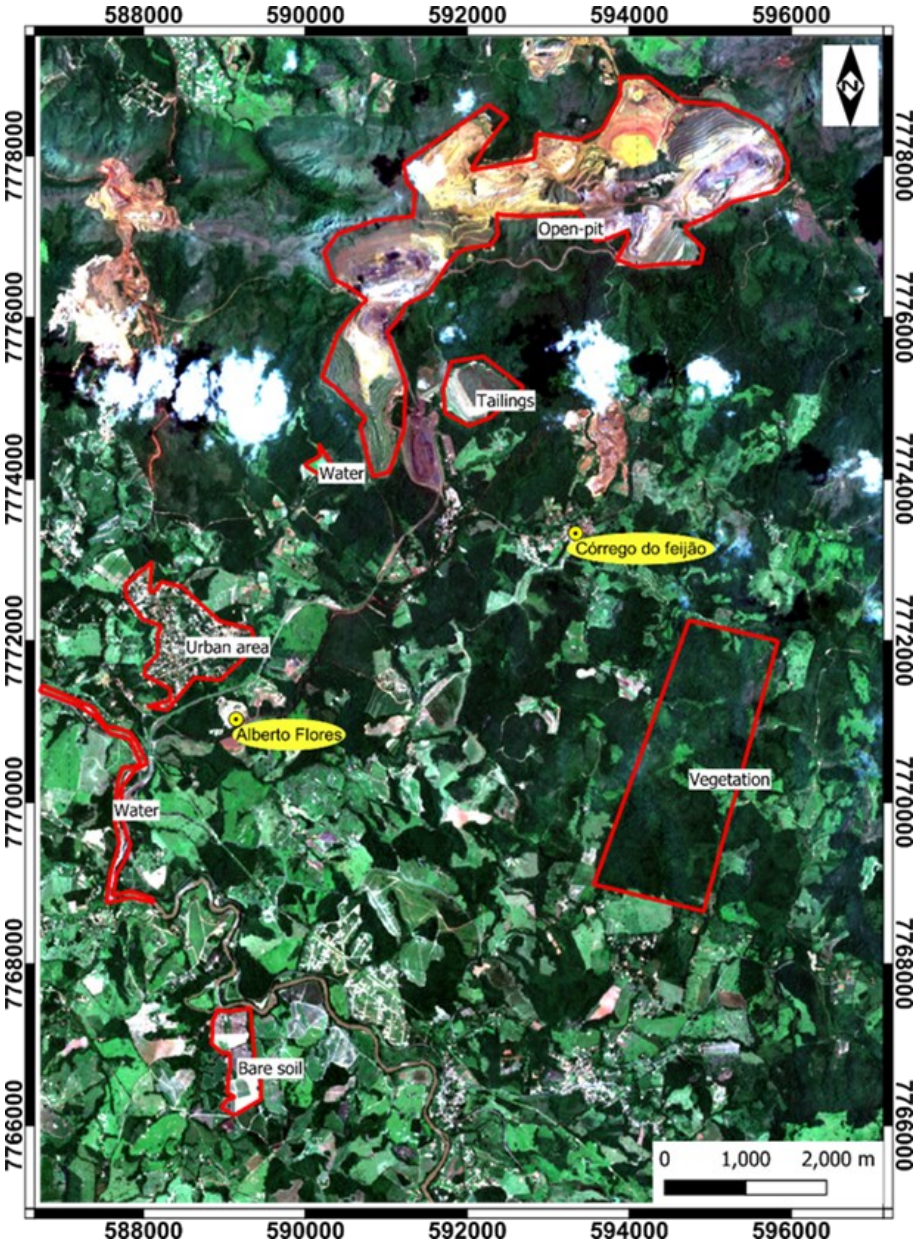

Fig. 8.1 Study area. The red zones are the principal elements (see section 8.4).

Generally, water is characterized by only reflection in the visible light range, with almost no reflection in the near-infrared range. However, the reflectance may increase between 400 and 1000 nm with turbidity showing maxima between 400 and 700 nm and 800 nm for highly turbid waters (Keshava and Mustard, 2002). Vegetation is generally characterized by an absorption caused by the chlorophyll in the blue range (450–550 nm), a high reflectance in the near-infrared region (~ 865 nm), and strong water absorption in the mid-infrared region (Adam et al., 2010). The

tailing dams and mining areas have the spectral signatures of ferric oxides. The spectral properties of iron-bearing oxide/hydroxide (i.e., hematite and goethite) have been studied in detail by several authors (Crowley et al., 2003; Curtiss, 1985). Hematite and goethite are characterized by diagnostic absorption features in the Visible Near InfraRed (VNIR) region of the electromagnetic spectrum, in the range between 450 nm and 1200 nm, due to electronic processes involving Fe^{3+} octahedrally bonded to ligands of oxygen (hematite α-Fe2O3) or oxygen and hydroxyl (goethite – α-FeO(OH)) (Hensler et al., 2015). Specifically, goethite generally exhibits the main spectral absorption ~ 940 nm, related to energy level changes in the valence electrons (Crystal Field Absorption features - CFA) Cudahy and Ramanaidou, 1997). Minor absorption features are at 480 nm and 670 nm (Charge Transfer Feature – CTS) (Cudahy and Ramanaidou, 1997), and the water-related bands occur close to 1400 nm and 1900 nm. On the other hand, the major CFA feature appears shifted to shorter wavelengths for hematite, occurring typically ~ 880 nm (Crowley et al., 2003). Absorption position displacements to longer wavelengths of the main Fe-bearing oxides/hydroxides feature (~14 nm; (Scheinost et al., 1999) are due to compositional variations related to Al^{3+} substitution for Fe^{3+} iron. In the present case study, tailing dams and mining areas spectral properties resulted comparable to the hematite signature from the official USGS spectral library (Souza et al., 2021), detectable through the absorption feature in band 8 of Sentinel-2 (centered in 842 nm) which is commonly used to investigate all the iron oxides and hydroxides, i.e., Ferric oxides (Ge et al., 2020; Mielke et al., 2014) (Figure 8.2). Thus, only water, vegetation, and ferric oxides were considered as valuable endmembers for mapping the most relevant features occurring in the study area.

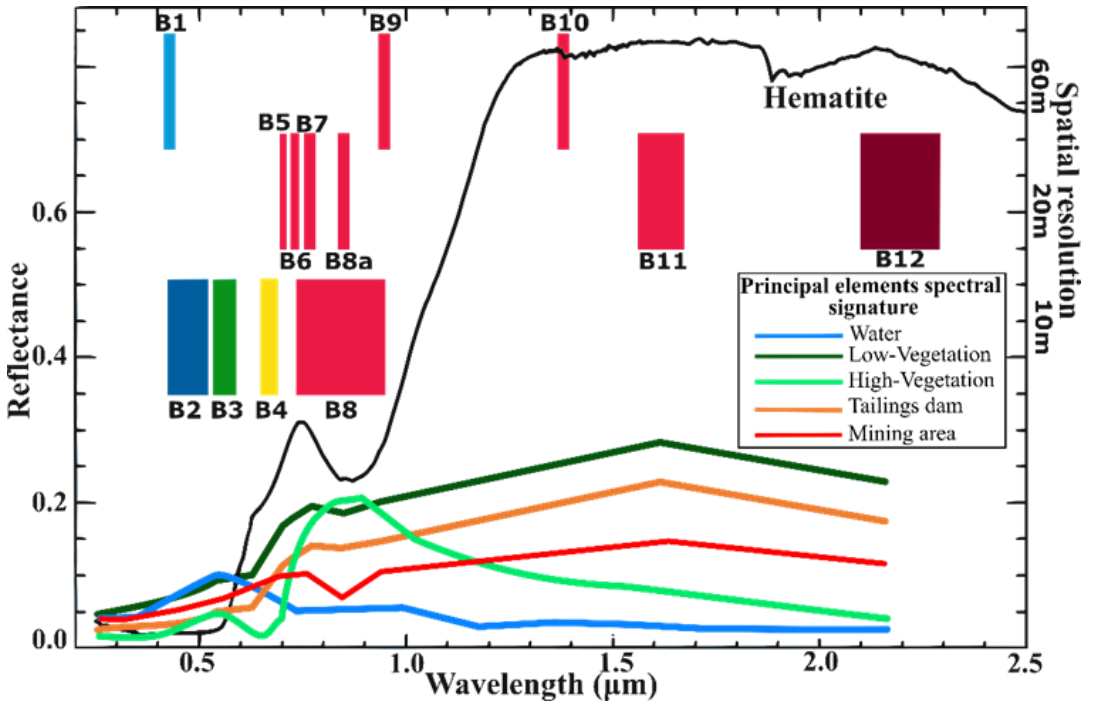

Fig. 8.2 The spectral properties of Principal Elements sampled in the pre-event image. The black line is the official USGS hematite signature (Kokaly et al., 2017b) compared to Sentinel-2 bands (from B1 to B12).

8.5 Results

Figure 8.3 shows the thematic maps in the Brumadinho mining district, during the pre-and post-failure event, revealing the relative abundances of selected endmember spectral signatures: i.e., ferric oxides, vegetation, and water. The maps have been characterized using a grayscale color, where the zero value indicates that the endmembers are not present, while greater values reveal where the endmembers are present. The water maps allowed to detect the water bodies present in the area, such as the river, and the dam corresponding to the principal elements in Figure 8.1. The temporal evolution of vegetation shows a different spectral response due to the decreasing of vegetated areas. The ferric oxides maps display the distribution of open-pit iron mine areas only in 2019, whereas in the years 2020 and 2021, they show an increase of the white color in the zones where the flood occurred.

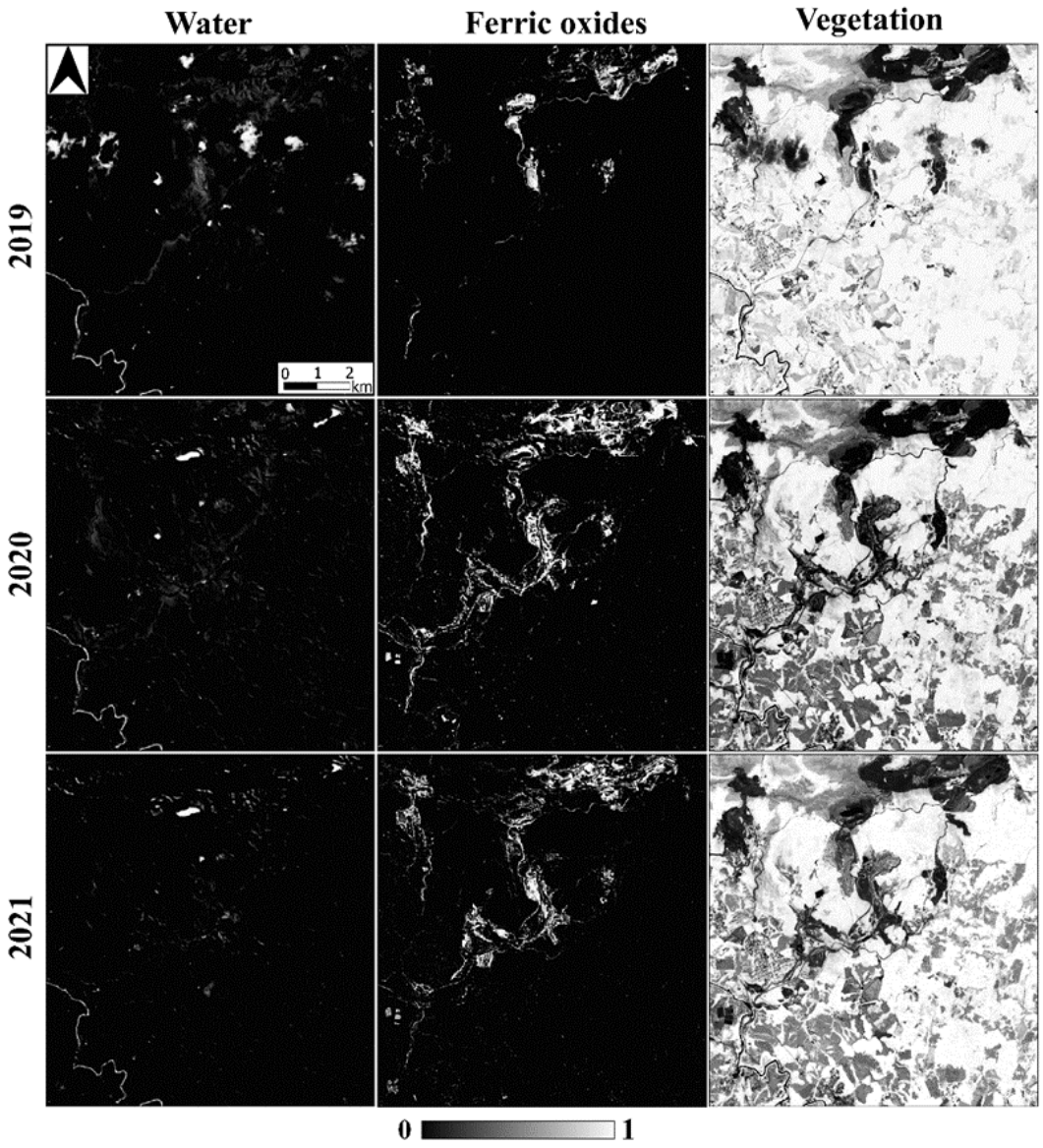

Fig. 8.3 The relative abundance maps of water, ferric oxides, and vegetation endmembers, at different periods.

An RGB color composite map was produced, assigning the ferric oxides, vegetation, and water abundances, respectively red, green, and blue. This process was applied for post-event satellite images, using the same training dataset as before (i. e. pre-event image). In the RGB maps (Figure 8.4) the red-colored ferric oxides-zones allow to better highlight the shape of the flooded areas in 2020 and 2021 (post-event) images. In all the images most of the considered area is covered by vegetation, but in the post-event periods (2020 and 2021), it is possible to observe a decreasing

vegetative rate in flood-affected zones. Four zones have been identified as flood-affected zones where a clear change in the soil nature is noted. It is worth pointing out that areas 1, 2, and 3 in the top, center, and bottom of the flood-ed area were characterized by an increase in the abundance of ferric oxides. In the 4th area, it is possible to detect pixels changing in the riverbed (R) and riverside (RS). Figure 8.4 shows how in 2020 the affected area was distinguished by an increase in red pixels that are not present in 2019, while a decrease is observed in 2021. Figure 6.5 shows the mean spectral signatures of the flood-affected zones. The graphs are distinguished for the years 2019, 2020, and 2021 and shown respectively in red, black, green, blue, and orange colors. It must be noted that the flood-affected zone 4 was divided into two mean spectra signatures obtained by the riverbed (R) and river side (RS) features.

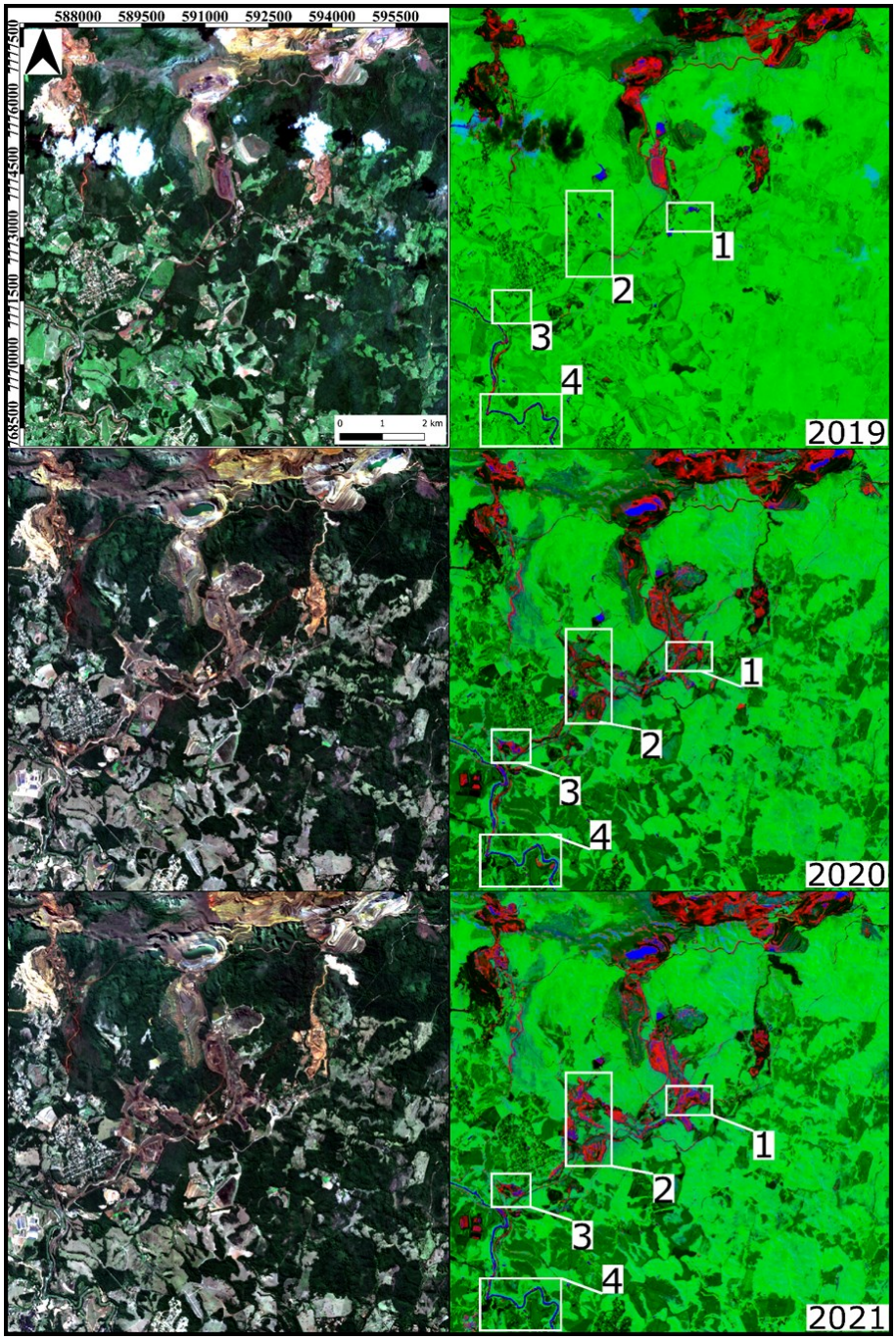

Fig. 8.4 The RGB true color on left, the RGB (ferric oxides, vegetation, water) composites with endmember abundances on right. The white boxes are the flood-affected zones selected.

In 2019 (Figure 8.5a), in the Flood-affected zones 1,2,3, and RS, the spectra are characterized by a visible ab-sorption band of about 560 nm, corresponding to the chlorophyll peak (Sanches et al., 2014), evidencing healthier vegetation. The R spectrum was similar to the water signature with absorption from the mid-infrared

region forward. After the flood event, the 2020 and 2021 spectra change. In particular, in 2020 (Figure 8.5b), it is possible to note the main spectral absorption ~ 840 μm in the VNIR region characteristic of the ferric oxides (van der Meer et al., 2014) decreases in 2021 (Figure 8.5c). Figures 5 b and c show in blue, the spectral signature achieved in 2020 and 2021 corresponding to the riverbed area where it is possible to note light absorption in the VNIR region characteristic of the ferric oxides and hydroxides and an increase in SWIR domains.

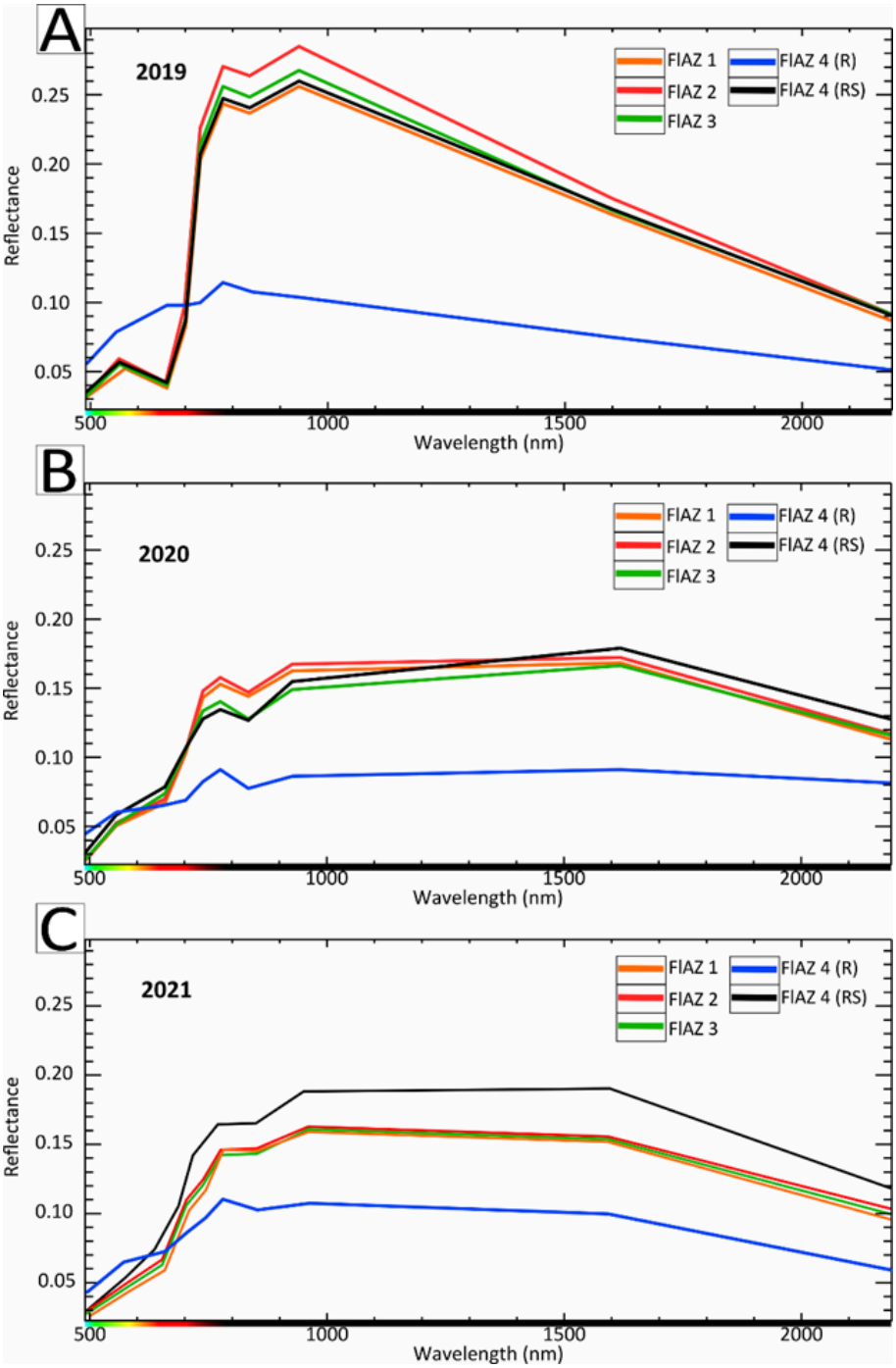

Fig. 8.5 Mean spectral signatures obtained by flood-affected zones 1st, 2nd, 3rd, and 4th (derived from the riverbed (R) and river side (RS) features) in 2019 (a), 2020 (b), 2021 (c).

8.6 Discussion

As reported by Silva Rotta et al. (2020) the flood resulted in a massive loss of local vegetation and agricultural areas comprising 49 % and 24 % of the areas most

affected by the floods. In the present study, the obtained results allowed to investigate the Brumadinho zone affected by the flood phenomena occurred in January 2019. The dam failure provoked fatalities, infrastructure damage, as well as caused considerable environmental aftermaths, which are still now present. This paper aimed to use the potential of multispectral Sentinel-2 data (MSI) to map the flood-affected zones one and two years after the disaster to remotely detect possible signatures still existing in the area. The Spectral Unmixing tool, using the different spectral responses of each material, allowed to identify areas, called Flood-affected zones, where the ferric oxides signature was observed. Satellite Multispectral data have been recently used (Syifa et al., 2019), for studying the Brumadinho dam collapse. The authors, by using artificial intelligence (AI) techniques based on the Landsat-8 and Sentinel-2 bands, defined the pixel classification for the pre-and post-dam failure. The maps produced by using each satellite data (Syifa et al., 2019) allowed dividing the study area into seven and five classes, respectively from the Landsat-8 and the Sentinel-2. The authors affirmed that the difference was attributed to the cloud that did not appear. (Syifa et al., 2019)used the AI classifications to differentiate the flood area from other land cover types, which could be negatively influenced by the input source data. Differently from (Syifa et al., 2019), we considered for our study a longer time interval (2019, 2020, 2021), and we used the specific spectral signatures of exposed materials (Figures 8.5). With this study, four areas were selected within the mining district, based on the ferric oxides impact. Considering that the images were acquired during the months of January, August, and July, the general decrease of the vegetation cover in the district from 2019 to 2021, could be associated with the seasons. However, the influence of ferric oxides related to the dam collapse doesn't depend on the seasonal vegetation rate. Figure 8.5 displays the mean spectral signatures, extracted in the selected zones, as a function of the wavelength band of the satellite. It is possible to notice that, still one year after the dam failure, the influence of ferric oxides is well defined in all the spectra (Figure 8.5b), where it is possible to note the ferric oxides absorption feature centered in 833 nm. In 2021 the ferric oxides impact continues to be highlighted by weak absorption. Spectra collected in the riverbed (Figure 8.5A) are characterized by

spectral properties which may be associated with water turbidity in the visible region. According to Gholizadeh et al. (2016) the effects of turbidity, due to suspended particles in surface waters, occur in the band range between 700 and 800 nm. Indeed, in 2019 it is possible to note a reflectance maximum at the same wavelength values, diagnostic of turbidity. While in 2020 and 2021 it is notable ferric oxides absorption (Figure 8.5B, C), thus suggesting that waste material still occurs in the river. According to Fang et al. (2018), the clay minerals in soils show diagnostic absorption features in the shortwave-infrared domain (SWIR), and their reflectance spectra exhibit OH-H_2O-related absorptions approximately around 1400 nm and 1900 nm, and Al-OH absorption near 2200 nm, the latter covered by Sentinel-2 in band 12 (2100–2280 nm) (Sekandari et al., 2020). In Figure 8.5 the signatures obtained in 2020 and 2021 show a spectral absorption feature in the SWIR region, which may be related to clay minerals occurring in the waste material. Indeed, the latter could be associated with the presence of kaolinite composing the silty-clayey fractions of the tailing dam material that after the failure moved in the flood and affected the surrounding areas. This observation is consistent with the mineralogical and geochemical composition of the tailing dam materials, discussed in previous studies on the Córrego do Feijão mine (Vergilio et al., 2020) and other tailing dams in the Quadrilatero Ferrifero area (Fundão Dam, Samarco mining company) (Thompson et al., 2020). According to Almeida et al. (2018), hematite occurs as the main phase in the mine waste of the Fundão Dam, followed by goethite, kaolinite, and gibbsite, in line with Vergilio et al. (2020, which observed Fe concentrations up to 26.5 wt.% and Al up to 1.1 wt%, for the fine waste material of the Córrego do Feijão mine. As Sentinel-2 cannot accurately detect the clay mineral content due to the low spectral resolution in the SWIR region, it didn't allow to use of this observation to produce specific clay distribution maps.

8.7 Conclusions

In this paper, a multispectral approach was used to determine affected areas by the flood generated after the dam collapse. Starting from the spectral analysis and using the SNAP tool, the absorption features of the mining products, vegetation and water were recognized, and land cover maps were produced. The methodology uses a

linear approach to obtain rapidly RGB composite maps useful to detect flood-affected zones. The multispectral bands of the Sentinel-2 data have proved to be an extremely useful tool for mapping flooded areas. The method allows for obtaining significant information potentially useful for monitoring lands affected by floods related to tailing dam collapse and planning the post activities management. To support the study and better examine the environmental impact, as essentially as possible, might be necessary to carry out a soil sampling of the flood-affected zones.

References

Aamir, M., Ali, T., Irfan, M., Shaf, A., Azam, M.Z., Glowacz, A., Brumercik, F., Glowacz, W., Alqhtani, S., Rahman, S., 2021. Natural Disasters Intensity Analysis and Classification Based on Multispectral Images Using Multi-Layered Deep Convolutional Neural Network. Sensors 21, 2648. https://doi.org/10.3390/s21082648

Abrams, M., Yamaguchi, Y., 2019. Twenty Years of ASTER Contributions to Lithologic Mapping and Mineral Exploration. Remote Sensing 11, 1394. https://doi.org/10.3390/rs11111394

Adam, E., Mutanga, O., Rugege, D., 2010. Multispectral and hyperspectral remote sensing for identification and mapping of wetland vegetation: a review. Wetlands Ecol Manage 18, 281–296. https://doi.org/10.1007/s11273-009-9169-z

Agenzia Spaziale Italiana (ASI), 2020. Agenzia Spaziale Italiana (ASI) (2020) PRISMA Products Specification Document Issue 2.1 Date 12/02/2020.

Aguirre, L., 1988. Chemical mobility during low-grade metamorphism of a Jurassic lava flow: Río Grande Formation, Peru. Journal of South American earth sciences 1, 343–361.

Ahmed, A.H., Arai, S., Ikenne, M., 2009. Mineralogy and Paragenesis of the Co-Ni Arsenide Ores of Bou Azzer, Anti-Atlas, Morocco. Economic Geology 104, 249–266. https://doi.org/10.2113/gsecongeo.104.2.249

Al Ganad, I., Lagny, P., Lescuyer, J.L., Ramboz, C., Touray, J.C., 1994. Jabali, a Zn-Pb-(Ag) carbonate-hosted deposit associated with Late Jurassic rifting in Yemen. Mineral. Deposita 29, 44–56. https://doi.org/10.1007/BF03326395

Alkmim, F.F., Marshak, S., 1998. Transamazonian Orogeny in the Southern São Francisco Craton Region, Minas Gerais, Brazil: evidence for Paleoproterozoic collision and collapse in the Quadrilátero Ferrífero. Precambrian Research 90, 29–58. https://doi.org/10.1016/S0301-9268(98)00032-1

Almeida, C.A., Oliveira, A.F. de, Pacheco, A.A., Lopes, R.P., Neves, A.A., Lopes Ribeiro de Queiroz, M.E., 2018. Characterization and evaluation of sorption potential

of the iron mine waste after Samarco dam disaster in Doce River basin – Brazil. Chemosphere 209, 411–420. https://doi.org/10.1016/j.chemosphere.2018.06.071

Alpers, C.N., Brimhall, G.H., 1988. Middle Miocene climatic change in the Atacama Desert, northern Chile: Evidence from supergene mineralization at La Escondida. Geological Society of America Bulletin 100, 1640–1656.

Amato, U., Antoniadis, A., Carfora, M.F., Colandrea, P., Cuomo, V., Franzese, M., Pignatti, S., Serio, C., 2013. Statistical Classification for Assessing PRISMA Hyperspectral Potential for Agricultural Land Use. IEEE Journal of Selected Topics in Applied Earth Observations and Remote Sensing 6, 615–625. https://doi.org/10.1109/JSTARS.2013.2255981

Ammirati, L., Chirico, R., Di Martire, D., Mondillo, N., 2022. Application of Multispectral Remote Sensing for Mapping Flood-Affected Zones in the Brumadinho Mining District (Minas Gerais, Brazil). Remote Sensing 14, 1501. https://doi.org/10.3390/rs14061501

Ammirati, L., Mondillo, N., Calcaterra, D., Di Martire, D., 2021. Sentinel-1 Data for Monitoring a Pre-failure Event of Tailings Dam, in: Rizzo, P., Milazzo, A. (Eds.), European Workshop on Structural Health Monitoring, Lecture Notes in Civil Engineering. Springer International Publishing, Cham, pp. 140–148. https://doi.org/10.1007/978-3-030-64908-1_13

Arévalo, A., Skewes, A., Stern, C., Floody, R., Goldfarb, R., Nielsen, R., Zúñiga, R., 2002. The giant El Teniente, breccia deposit: hypogene copper distribution and emplacement. Integrated methods for discovery: Global exploration in the Twenty-first Century 9, 299–332.

As-Saruri, M.A., Sorkhabi, R., Baraba, R., 2010. Sedimentary basins of Yemen: their tectonic development and lithostratigraphic cover. Arab J Geosci 3, 515–527. https://doi.org/10.1007/s12517-010-0189-z

Babinski, M., Chemale, F., Van Schmus, W.R., 1995. The Pb/Pb age of the Minas Supergroup carbonate rocks, Quadrilátero Ferrífero, Brazil. Precambrian Research 72, 235–245. https://doi.org/10.1016/0301-9268(94)00091-5

Balassone, G. and Bellatreccia F., 2019. Spettroscopia nell'infrarosso, In Mercurio M, Langella A, Di Maggio RM, Cappelletti P, editors. Analisi Mineralogiche in ambito forense. Canterano, RM: Aracne editrice, 2019:83–131. ISBN 978–88–255-2235-8.

Ballantyne, G.H., 1981. Chemical and mineralogical variations in propylitic zones surrounding porphyry copper deposits: Unpublished Ph.D. thesis, Utah, University of Utah, 208 p.

Baltazar, O.F., Zucchetti, M., 2007. Lithofacies associations and structural evolution of the Archean Rio das Velhas greenstone belt, Quadrilátero Ferrífero, Brazil: A review of the setting of gold deposits. Ore Geology Reviews, Special Issue on Gold Deposits of Quadrilátero Ferrífero, Minas Gerais, Brazil 32, 471–499. https://doi.org/10.1016/j.oregeorev.2005.03.021

Barra, F., Reich, M., Selby, D., Rojas, P., Simon, A., Salazar, E., Palma, G., 2017. Unraveling the origin of the Andean IOCG clan: A Re-Os isotope approach. Ore Geology Reviews 81, 62–78. https://doi.org/10.1016/j.oregeorev.2016.10.016

Beckinsale, R., Sanchez-Fernandez, A., Brook, M., Cobbing, E., Taylor, W., Moore, N., 1985. Rb-Sr whole-rock isochron and K-Ar age determinations fot he Coastal Batholith of Peru. Presented at the Magmatism at a plate edge. The Peruvian Andes, pp. 177–202.

Bedini, E., 2017. The use of hyperspectral remote sensing for mineral exploration: a review. Journal of Hyperspectral Remote Sensing 7, 189–211. https://doi.org/10.29150/jhrs.v7.4.p189-211

Bedini, E., Chen, J., 2020. Application of PRISMA satellite hyperspectral imagery to mineral alteration mapping at Cuprite, Nevada, USA. Journal of Hyperspectral Remote Sensing v 10, 87–94.

Belov, N. V., & Rumanova, J. M., 1953. The crystal structure of epidote $Ca_2Al_2FeSi_3O_{12}(OH)$: Doklady Akademii Nauk SSSR, 89, 853-856.

Belperio, A., Flint, R., Freeman, H., 2007. Prominent Hill: A hematite-dominated, iron oxide copper-gold system. Economic Geology 102, 1499–1510.

Benavides, J., Kyser, T., Clark, A.H., Oates, C.J., Zamora, R., Tarnovschi, R., Castillo, B., 2007. The Mantoverde iron oxide-copper-gold district, III Región, Chile: the role of regionally derived, nonmagmatic fluids in chalcopyrite mineralization. Economic Geology 102, 415–440.

Berger, B.R., King, T.V.V., Morath, L.C., Phillips, J.D., 2003. Utility of High-Altitude Infrared Spectral Data in Mineral Exploration: Application to Northern Patagonia Mountains, Arizona. Economic Geology 98, 1003–1018. https://doi.org/10.2113/gsecongeo.98.5.1003

Biel, C., Subías, I., Acevedo, R.D., Yusta, I., Velasco, F., 2012. Mineralogical, IR-spectral and geochemical monitoring of hydrothermal alteration in a deformed and metamorphosed Jurassic VMS deposit at Arroyo Rojo, Tierra del Fuego, Argentina. Journal of South American Earth Sciences 35, 62–73. https://doi.org/10.1016/j.jsames.2011.11.005

Bish, D.L., Post, J.E., 1993. Quantitative mineralogical analysis using the Rietveld full-pattern fitting method. American Mineralogist 78, 932–940.

Bishop, J.L., Lane, M.D., Dyar, M.D., Brown, A.J., 2008. Reflectance and emission spectroscopy study of four groups of phyllosilicates: smectites, kaolinite-serpentines, chlorites and micas. Clay Minerals 43, 35–54. https://doi.org/10.1180/claymin.2008.043.1.03

Bishop, J.L., Murad, E., 2005. The visible and infrared spectral properties of jarosite and alunite. American Mineralogist 90, 1100–1107. https://doi.org/10.2138/am.2005.1700

Blengini, G.A., Nuss, P., Dewulf, J., Nita, V., Peirò, L.T., Vidal-Legaz, B., Latunussa, C., Mancini, L., Blagoeva, D., Pennington, D., Pellegrini, M., Van Maercke, A., Solar, S., Grohol, M., Ciupagea, C., 2017. EU methodology for critical raw materials assessment: Policy needs and proposed solutions for incremental

improvements. Resources Policy 53, 12–19. https://doi.org/10.1016/j.resourpol.2017.05.008

Boni, M., Balassone, G., Iannace, A., 1996. Base Metal Ores in the Lower Paleozoic of Southwestern Sardinia, in: Sangster, D.F. (Ed.), Carbonate-Hosted Lead-Zinc Deposits: 75th Anniversary Volume. Society of Economic Geologists, p. 0. https://doi.org/10.5382/SP.04.03

Boni, M., Mondillo, N., Balassone, G., 2011. Zincian dolomite: A peculiar dedolomitization case? Geology 39, 183–186. https://doi.org/10.1130/G31486.1

Bouzari, F., Clark, A.H., 2002. Anatomy, evolution, and metallogenic significance of the supergene orebody of the Cerro Colorado porphyry copper deposit, I Región, northern Chile. Economic Geology 97, 1701–1740.

Brown, M., Diaz, F., Grocott, J., 1993. Displacement history of the Atacama fault system 25° 00′ S-27° 00′ S, northern Chile. Geological Society of America Bulletin 105, 1165–1174.

Burns, R.G., 1993, Mineralogical Applications of Crystal Field Theory: Cambridge University Press, 563.

Cabello, J., 2021. Gold deposits in Chile. Andean Geology 48, 1–23.

Cabral, A.R., Zeh, A., Koglin, N., Gomes Jr, A.A.S., Viana, D.J., Lehmann, B., 2012. Dating the Itabira iron formation, Quadrilátero Ferrífero of Minas Gerais, Brazil, at 2.65 Ga: depositional U–Pb age of zircon from a metavolcanic layer. Precambrian Research 204, 40–45.

Campbell, J.B., Wynne, R.H., 2011. Introduction to Remote Sensing, Fifth Edition. Guilford Press.

Casa, R., Pignatti, S., Pascucci, S., Ionca, V., Mzid, N., Veretelnikova, I., 2020. Assessment of PRISMA imaging spectrometer data for the estimation of topsoil properties of agronomic interest at the field scale 6728. https://doi.org/10.5194/egusphere-egu2020-6728

Casagli, N., Frodella, W., Morelli, S., Tofani, V., Ciampalini, A., Intrieri, E., Raspini, F., Rossi, G., Tanteri, L., Lu, P., 2017. Spaceborne, UAV and ground-based remote sensing techniques for landslide mapping, monitoring and early warning. Geoenviron Disasters 4, 9. https://doi.org/10.1186/s40677-017-0073-1

Castelli, D.C.C., Giorza, A., Rossetti, P., Piana, F., Clerico, F., 2011. Le mineralizzazioni a siderite e arseniuri di cobalto-ferro-nichel del vallone di Arnàs (Usseglio, valli di Lanzo), in: Terre Rosse, Pietre Verdi e Blu Cobalto. Miniere a Usseglio-Prima Raccolta Di Studi. Museo Civico Alpino" Arnaldo Tazzetti", pp. 21–36.

Chang, Z., Hedenquist, J.W., White, N.C., Cooke, D.R., Roach, M., Deyell, C.L., Garcia Jr, J., Gemmell, J.B., McKnight, S., and Cuison, A.L., 2011. Exploration tools for linked porphyry and epithermal deposits: Example from the Mankayan intrusion-centered Cu-Au district, Luzon, Philippines: Economic Geology, 106, no. 8, 1365–1398.

Chemale, F., Rosière, C.A., Endo, I., 1994. The tectonic evolution of the Quadrilátero Ferrífero, Minas Gerais, Brazil. Precambrian Research 65, 25–54. https://doi.org/10.1016/0301-9268(94)90098-1

Chen, H., 2013. External sulphur in IOCG mineralization: Implications on definition and classification of the IOCG clan. Ore Geology Reviews 51, 74–78. https://doi.org/10.1016/j.oregeorev.2012.12.002

Chen, H., Cooke, D.R., Baker, M.J., 2013. Mesozoic iron oxide copper-gold mineralization in the Central Andes and the Gondwana supercontinent breakup. Economic Geology 108, 37–44.

Chen, Q., Zhao, Z., Zhou, J., Zeng, M., Xia, J., Sun, T., Zhao, X., 2021. New Insights into the Pulang Porphyry Copper Deposit in Southwest China: Indication of Alteration Minerals Detected Using ASTER and WorldView-3 Data. Remote Sensing 13, 2798. https://doi.org/10.3390/rs13142798

Chirico, R., Mondillo, N., Laukamp, C., Mormone, A., Di Martire, D., Novellino, A., Balassone, G., 2023. Mapping hydrothermal and supergene alteration zones

associated with carbonate-hosted Zn-Pb deposits by using PRISMA satellite imagery supported by field-based hyperspectral data, mineralogical and geochemical analysis. Ore Geology Reviews 152, 105244. https://doi.org/10.1016/j.oregeorev.2022.105244

Christmann, P., Lagny, P., Lescuyer, J.-L., Sharaf Ad Din, A., 1989. Discovery of the Jabali deposit (Zn-Pb-Ag) in the Jurassic cover of the Yemen Arab Republic. Chronique de la recherche minière 43–52.

Chung, F.H., 1974a. Quantitative interpretation of X-ray diffraction patterns of mixtures. I. Matrix-flushing method for quantitative multicomponent analysis. J Appl Cryst 7, 519–525. https://doi.org/10.1107/S0021889874010375

Chung, F.H., 1974b. Quantitative interpretation of X-ray diffraction patterns of mixtures. II. Adiabatic principle of X-ray diffraction analysis of mixtures. J Appl Cryst 7, 526–531. https://doi.org/10.1107/S0021889874010387

Cidu, R., Fanfani, L., 2002. Overview of the environmental geochemistry of mining districts in southwestern Sardinia, Italy. GEEA 2, 243–251. https://doi.org/10.1144/1467-787302-028

Clark, A.H., Farrar, E., Kontak, D.J., Langridge, R.J., Arenas F, M.J., France, L.J., McBride, S.L., Woodman, P.L., Wasteneys, H.A., Sandeman, H.A., 1990a. Geologic and geochronologic constraints on the metallogenic evolution of the Andes of southeastern Peru. Economic Geology 85, 1520–1583.

Clark, R.N., King, T.V.V., Klejwa, M., Swayze, G.A., Vergo, N., 1990b. High spectral resolution reflectance spectroscopy of minerals. Journal of Geophysical Research: Solid Earth 95, 12653–12680. https://doi.org/10.1029/JB095iB08p12653

Cogliati, S., Sarti, F., Chiarantini, L., Cosi, M., Lorusso, R., Lopinto, E., Miglietta, F., Genesio, L., Guanter, L., Damm, A., Pérez-López, S., Scheffler, D., Tagliabue, G., Panigada, C., Rascher, U., Dowling, T.P.F., Giardino, C., Colombo, R., 2021. The PRISMA imaging spectroscopy mission: overview and first performance analysis. Remote Sensing of Environment 262, 112499. https://doi.org/10.1016/j.rse.2021.112499

Coppo, P., Brandani, F., Faraci, M., Sarti, F., Dami, M., Chiarantini, L., Ponticelli, B., Giunti, L., Fossati, E., Cosi, M., 2020. Leonardo spaceborne infrared payloads for Earth observation: SLSTRs for Copernicus Sentinel 3 and PRISMA hyperspectral camera for PRISMA satellite. Appl. Opt., AO 59, 6888–6901. https://doi.org/10.1364/AO.389485

Correa, A., 2003. El Espino, un nuevo depósito del tipo Fe-Cu (Au) en Chile. Comuna de Illapel, Región de Coquimbo. Unpublished MS thesis, Universidad Catolica del Norte, Antofagasta, Chile.

Corriveau, L., 2007. Iron oxide copper-gold (±Ag±Nb±P±REE±U) deposits: a Canadian perspective. Mineral deposits of Canada: a synthesis of major deposit-types, district metallogeny, the evolution of geological provinces, and exploration methods, Special publication no 5, 307–328.

Corriveau, L., Montreuil, J.-F., Potter, E.G., 2016. Alteration facies linkages among iron oxide copper-gold, iron oxide-apatite, and affiliated deposits in the Great Bear magmatic zone, Northwest Territories, Canada. Economic Geology 111, 2045–2072.

Cortés, J, Marquardt, C., González, G., Wilke, H., Marinovic, N., 2007. Cartas Mejillones y Península de Mejillones, Región de Antofagasta., Carta Geológica de Chile, Serie Geología Básica, 103 y 104, 58 p., 1 mapa escala 1: 100.000.

Cotton III, W.B., 2003. Near infrared and XRD quantification of porphyry copper alteration at Cerro Colorado and Spence, Chile. University of Colorado at Boulder.

Crowley, J.K., 1986. Visible and near-infrared spectra of carbonate rocks: Reflectance variations related to petrographic texture and impurities. Journal of Geophysical Research: Solid Earth 91, 5001–5012. https://doi.org/10.1029/JB091iB05p05001

Crowley, J.K., 1991. Visible and near-infrared (0.4–2.5 μm) reflectance spectra of Playa evaporite minerals. Journal of Geophysical Research: Solid Earth 96, 16231–16240. https://doi.org/10.1029/91JB01714

Crowley, J.K., Brickey, D.W., Rowan, L.C., 1989. Airborne imaging spectrometer data of the Ruby Mountains, Montana: Mineral discrimination using relative absorption band-depth images. Remote Sensing of Environment 29, 121–134. https://doi.org/10.1016/0034-4257(89)90021-7

Crowley, J.K., Williams, D.E., Hammarstrom, J.M., Piatak, N., Chou, I.-M., Mars, J.C., 2003. Spectral reflectance properties (0.4–2.5 μm) of secondary Fe-oxide, Fe-hydroxide, and Fe-sulphate-hydrate minerals associated with sulphide-bearing mine wastes. Geochemistry: Exploration, Environment, Analysis 3, 219–228. https://doi.org/10.1144/1467-7873/03-001

Cudahy, T., Jones, M., Thomas, M., Laukamp, C., Caccetta, M., Hewson, R., Rodger, A., Verrall, M., 2008. Next Generation Mineral Mapping: Queensland airborne HyMap and satellite ASTER surveys 2006-2008. https://doi.org/10.13140/RG.2.1.2828.1844

Cudahy, T.J., Ramanaidou, E.R., 1997. Measurement of the hematite:goethite ratio using field visible and near-infrared reflectance spectrometry in channel iron deposits, Western Australia. Australian Journal of Earth Sciences 44, 411–420. https://doi.org/10.1080/08120099708728322

Curtiss, B., 1985. Evaluation of the Physical Properties of Naturally Occurring Iron (III) Oxyhydroxides on Rock Surfaces in Arid and Semi-arid Regions Using Visible and Near Infrared Reflectance Spectroscopy: PhD Thesis, University of Washington.

Dallmeyer, R.D., Brown, M., Grocott, J., Taylor, G.K., Treloar, P.J., 1996. Mesozoic magmatic and tectonic events within the Andean plate boundary zone, 26-27 30'S, north Chile: Constraints from $^{40}Ar/^{39}Ar$ mineral ages. The Journal of Geology 104, 19–40.

Davies, G.R., Smith, L.B., Jr., 2006. Structurally controlled hydrothermal dolomite reservoir facies: An overview. AAPG Bulletin 90, 1641–1690. https://doi.org/10.1306/05220605164

De Bonis, R., Laneve, G., Palombo, A., Pascucci, S., Pignatti, S., Santini, F., Ananasso, C., 2015. The potential impact of the next hyperspectral prisma mission on the natural and anthropogenic hazards management, in: 2015 IEEE 15th International Conference on Environment and Electrical Engineering (EEEIC). Presented at the 2015 IEEE 15th International Conference on Environment and Electrical Engineering (EEEIC), pp. 1643–1646. https://doi.org/10.1109/EEEIC.2015.7165418

de Haller, A., Zúñiga, A., Corfu, F., Fontboté, L., 2002. The iron oxide-Cu-Au deposit of Raúl-Condestable. Presented at the Mala, Lima, Peru [abs.]: Congreso Geológico Peruano, 11th, Resúmenes, p. 80.

de Minas Gerais, C. de S., do Brasil, S.G., 2019. Informativo n° 32-Informativo diário dos parâmetros de qualidade das águas nos locais monitorados ao longo do Rio Paraopeba, após o desastre na barragem B1 no complexo da Mina Córrego Feijão da Mineradora Vale/SA de Brumadinho-Minas Gerais.

Deckart, K., Clark, A.H., Celso, A.A., Ricardo, V.R., Bertens, A.N., Mortensen, J.K., Fanning, M., 2005. Magmatic and hydrothermal chronology of the giant Río Blanco porphyry copper deposit, central Chile: Implications of an integrated U-Pb and 40Ar/39Ar database. Economic Geology 100, 905–934.

Deckart, K., Silva, W., Spröhnle, C., Vela, I., 2014. Timing and duration of hydrothermal activity at the Los Bronces porphyry cluster: An update. Mineralium Deposita 49, 535–546.

del Real, I., Thompson, J.F., Carriedo, J., 2018. Lithological and structural controls on the genesis of the Candelaria-Punta del Cobre Iron Oxide Copper Gold district, Northern Chile. Ore Geology Reviews 102, 106–153.

Della Ventura, G., Hawthorne, F.C., Robert, J.-L., Iezzi, G., 2003. Synthesis and infrared spectroscopy of amphiboles along the tremolite-pargasite join. European Journal of Mineralogy 15, 341–347.

Deroin, J.P., Téreygeol, F., Heckes, J., 2011. Evaluation of very high to medium resolution multispectral satellite imagery for geoarchaeology in arid regions – Case

study from Jabali, Yemen. Journal of Archaeological Science 38, 101–114. https://doi.org/10.1016/j.jas.2010.08.015

Deroin, J.P., Téreygeol, F., Heckes, J., 2012. Remote Sensing Study of the Ancient Jabali Silver Mines (Yemen): From Past to Present, in: Lasaponara, R., Masini, N. (Eds.), Satellite Remote Sensing: A New Tool for Archaeology, Remote Sensing and Digital Image Processing. Springer Netherlands, Dordrecht, pp. 231–245. https://doi.org/10.1007/978-90-481-8801-7_10

Domenighini, G., Santoro, L., Moroni, M., Zanin, S., 2022. Co-Ni mineralization in the Punta Corna hydrothermal vein system (Piemonte, Italy): preliminary results, in: SGI-SIMP 2022: Geosciences for a Sustainable Future: Abstract Book. Società Geologica Italiana, pp. 408–408.

Dorr, J.V.N., 1969. Physiographic, stratigraphic, and structural development of the Quadrilatero Ferrifero, Minas Gerais, Brazil [WWW Document]. URL https://pubs.er.usgs.gov/publication/pp641A (accessed 1.11.22).

Du, Z., Ge, L., Ng, A.H.-M., Zhu, Q., Horgan, F.G., Zhang, Q., 2020. Risk assessment for tailings dams in Brumadinho of Brazil using InSAR time series approach. Science of The Total Environment 717, 137125. https://doi.org/10.1016/j.scitotenv.2020.137125

Duke, E.F., 1994. Near infrared spectra of muscovite, Tschermak substitution, and metamorphic reaction progress: Implications for remote sensing. Geology 22, 621–624. https://doi.org/10.1130/0091-7613(1994)022<0621:NISOMT>2.3.CO;2

EnMAP Mission - [WWW Document], n.d. URL https://www.enmap.org/mission/ (accessed 1.26.23).

European Commission (EU), 2018. Report on Critical Raw Materials in the Circular Economy.

European Commission (EU), 2020. Report on Critical Raw Materials in the Circular Economy.

Fadda, A.O., 1994. The sulcis carboniferous basin—geology, hydrogeology, mines - Carbosulcis S.p.a, Cagliari, Italy.

Farr, T.G., Rosen, P.A., Caro, E., Crippen, R., Duren, R., Hensley, S., Kobrick, M., Paller, M., Rodriguez, E., Roth, L., Seal, D., Shaffer, S., Shimada, J., Umland, J., Werner, M., Oskin, M., Burbank, D., Alsdorf, D., 2007. The Shuttle Radar Topography Mission. Reviews of Geophysics 45. https://doi.org/10.1029/2005RG000183

Flood, N., Watson, F., Collett, L., 2019. Using a U-net convolutional neural network to map woody vegetation extent from high resolution satellite imagery across Queensland, Australia. International Journal of Applied Earth Observation and Geoinformation 82, 101897. https://doi.org/10.1016/j.jag.2019.101897

Folkman, M.A., Pearlman, J., Liao, L.B., Jarecke, P.J., 2001. EO-1/Hyperion hyperspectral imager design, development, characterization, and calibration, in: Hyperspectral Remote Sensing of the Land and Atmosphere. Presented at the Hyperspectral Remote Sensing of the Land and Atmosphere, SPIE, pp. 40–51. https://doi.org/10.1117/12.417022

Foster, M.D., 1962. Interpretation of the composition and a classification of the chlorites: U.S. Geological Survey, Professional Paper 414-A, 1–33.

Frost, R.L. and Johansson, U., 1998. Combination Bands in the Infrared Spectroscopy of Kaolins—A Drift Spectroscopic Study. Clays Clay. Miner. 46, 466–477.

Furlan, J.P.R., dos Santos, L.D.R., Moretto, J.A.S., Ramos, M.S., Gallo, I.F.L., Alves, G. de A.D., Paulelli, A.C., Rocha, C.C. de S., Cesila, C.A., Gallimberti, M., Devóz, P.P., Júnior, F.B., Stehling, E.G., 2020. Occurrence and abundance of clinically relevant antimicrobial resistance genes in environmental samples after the Brumadinho dam disaster, Brazil. Science of The Total Environment 726, 138100. https://doi.org/10.1016/j.scitotenv.2020.138100

Gaffey, S.J., 1985. Reflectance spectroscopy in the visible and near-infrared (0.35–2.55 μm): Applications in carbonate petrology. Geology 13, 270–273. https://doi.org/10.1130/0091-7613(1985)13<270:RSITVA>2.0.CO;2

Gaffey, S.J., 1986. Spectral reflectance of carbonate minerals in the visible and near infrared (0.35-2.55 microns); calcite, aragonite, and dolomite. American Mineralogist 71, 151–162.

García, M., Maksaev, V., Townley, B., Dilles, J., 2017. Metallogeny, structural evolution, post-mineral cover distribution and exploration in concealed areas of the northern Chilean Andes. Ore Geology Reviews 86, 652–672.

Ge, W., Cheng, Q., Jing, L., Wang, F., Zhao, M., Ding, H., 2020. Assessment of the Capability of Sentinel-2 Imagery for Iron-Bearing Minerals Mapping: A Case Study in the Cuprite Area, Nevada. Remote Sensing 12, 3028. https://doi.org/10.3390/rs12183028

Gendall, I.R., Quevedo, L.A., Sillitoe, R.H., Spencer, R.M., Puente, C.O., and León, J.P., 2000. Discovery of a Jurassic porphyry copper belt, Pangui area, southern Ecuador: SEG Discovery, no. 43, 1–15.

Gervilla, F., Fanlo, I., Colás, V., Subías, I., 2012. Mineral compositions and phase relations of Ni–Co–Fe arsenide ores from the Aghbar Mine, Bou Azzer, Morocco. The Canadian Mineralogist 50, 447–470. https://doi.org/10.3749/canmin.50.2.447

Gholizadeh, M.H., Melesse, A.M., Reddi, L., 2016. A Comprehensive Review on Water Quality Parameters Estimation Using Remote Sensing Techniques. Sensors 16, 1298. https://doi.org/10.3390/s16081298

Giardino, C., Bresciani, M., Braga, F., Fabbretto, A., Ghirardi, N., Pepe, M., Gianinetto, M., Colombo, R., Cogliati, S., Ghebrehiwot, S., Laanen, M., Peters, S., Schroeder, T., Concha, J.A., Brando, V.E., 2020. First Evaluation of PRISMA Level 1 Data for Water Applications. Sensors 20, 4553. https://doi.org/10.3390/s20164553

Giorza, A., Castelli, D.C.C., Piana, F., Rossetti, P., 2007. The siderite-CoNi-arsenide mesothermal system of Taglio del Ferro (Lanzo Valley, Italy): an integrated

petrological and structural study of post-metamorphic hydrothermalism in the metaophiolites of Western Alps, in: Epitome Geoitalia 2007. Geoitalia, pp. 404–404.

Gläßer, C., Reinartz, P., 2005. Multitemporal and Multispectral Remote Sensing Approach for Flood Detection in the Elbe-Mulde Region 2002. Acta hydrochimica et hydrobiologica 33, 395–403. https://doi.org/10.1002/aheh.200400599

Green, D., Schodlok, M., 2016. Characterisation of carbonate minerals from hyperspectral TIR scanning using features at 14 000 and 11 300 nm. Australian Journal of Earth Sciences 63, 951–957. https://doi.org/10.1080/08120099.2016.1225601

Grieco, G., Moroni, M., Bussolesi, M., Cavallo, A., Orizio, S., 2021. Spatial distribution of the ophiolite-hosted Co-Ni-As-rich hydrothermal mineralization in the Punta Corna Mining complex, Lanzo Valleys, Northern Italy EGU21-7589. https://doi.org/10.5194/egusphere-egu21-7589

Griffiths, P.R., Chalmers, J.M., 2002. Handbook of vibrational spectroscopy. Wiley Online Library.

Grocott, J., Taylor, G.K., 2002. Magmatic arc fault systems, deformation partitioning and emplacement of granitic complexes in the Coastal Cordillera, north Chilean Andes (25 30′ S to 27 00′ S). Journal of the Geological Society 159, 425–443.

Groves, D.I., Bierlein, F.P., Meinert, L.D., Hitzman, M.W., 2010. Iron Oxide Copper-Gold (IOCG) Deposits through Earth History: Implications for Origin, Lithospheric Setting, and Distinction from Other Epigenetic Iron Oxide Deposits. Economic Geology 105, 641–654. https://doi.org/10.2113/gsecongeo.105.3.641

Gualtieri, A., Norby, P., Hanson, J., Hriljac, J., 1996. Rietveld Refinement using Synchrotron X-ray Powder Diffraction Data Collected in Transmission Geometry using an Imaging-Plate Detector: Application to Standard m-ZrO2. J Appl Cryst 29, 707–713. https://doi.org/10.1107/S0021889896008199

Gualtieri, A.F., 2000. Accuracy of XRPD QPA using the combined Rietveld–RIR method. J Appl Cryst 33, 267–278. https://doi.org/10.1107/S002188989901643X

Guanter, L., Irakulis-Loitxate, I., Gorroño, J., Sánchez-García, E., Cusworth, D.H., Varon, D.J., Cogliati, S., Colombo, R., 2021. Mapping methane point emissions with the PRISMA spaceborne imaging spectrometer. Remote Sensing of Environment 265, 112671. https://doi.org/10.1016/j.rse.2021.112671

Guild, P.W., 1953. Iron deposits of the Congonhas District, Minas Gerais, Brazil. Economic Geology 48, 639–676. https://doi.org/10.2113/gsecongeo.48.8.639

Guimarães, D., 1935. Contribuição ao estudo da origem dos depositos de minerio de ferro e manganez do centro de Minas Geraes.

Haest, M., Cudahy, T., Laukamp, C., Gregory, S., 2012a. Quantitative Mineralogy from Infrared Spectroscopic Data. I. Validation of Mineral Abundance and Composition Scripts at the Rocklea Channel Iron Deposit in Western Australia. Economic Geology 107, 209–228. https://doi.org/10.2113/econgeo.107.2.209

Haest, M., Cudahy, T., Laukamp, C., Gregory, S., 2012b. Quantitative Mineralogy from Infrared Spectroscopic Data. II. Three-Dimensional Mineralogical Characterization of the Rocklea Channel Iron Deposit, Western Australia. Economic Geology 107, 229–249. https://doi.org/10.2113/econgeo.107.2.229

Halley, S., Dilles, J.H., Tosdal, R.M., 2015. Footprints: Hydrothermal Alteration and Geochemical Dispersion Around Porphyry Copper Deposits. SEG Discovery 1–17. https://doi.org/10.5382/SEGnews.2015-100.fea

Halls, C., Stumpfl, E., 1972. The five-element (Ag-Bi-Co-Ni-As) vein deposits—A critical appraisal of the geological environments in which it occurs and of the theories affecting its origin. Presented at the 24th International Geological Congress, Section, p. 540.

Handbook, S.U., Tools, E., 2015. Sentinel-2 User Handbook. ESA Standard Document Date 1, 1–64.

Hansen, M.C., Loveland, T.R., 2012. A review of large area monitoring of land cover change using Landsat data. Remote Sensing of Environment, Landsat Legacy Special Issue 122, 66–74. https://doi.org/10.1016/j.rse.2011.08.024

Harraden, C.L., Mcnulty, B.A., Gregory, M.J., Lang, J.R., 2013. Shortwave Infrared Spectral Analysis of Hydrothermal Alteration Associated with the Pebble Porphyry Copper-Gold-Molybdenum Deposit, Iliamna, Alaska. Economic Geology 108, 483–494. https://doi.org/10.2113/econgeo.108.3.483

Hawthorne, F.C., 1983. The crystal chemistry of the amphiboles. Reviews in Mineralogy and Geochemistry, 9(1), 1-102.

He, Z., Shu, R., Wang, J., 2012. Research on method of geometry and spectral calibration of pushbroom dispersive hyperspectral imager, in: Multispectral, Hyperspectral, and Ultraspectral Remote Sensing Technology, Techniques and Applications IV. Presented at the Multispectral, Hyperspectral, and Ultraspectral Remote Sensing Technology, Techniques and Applications IV, SPIE, pp. 106–112. https://doi.org/10.1117/12.977423

Hedenquist, J.W., Arribas, A., 2022. Exploration Implications of Multiple Formation Environments of Advanced Argillic Minerals. Economic Geology 117, 609–643. https://doi.org/10.5382/econgeo.4880

Helba, H.A., Khalil, K.I., Abou, N.M.F., 2001. Alteration Patterns Related to Hydrothermal Gold Mineralizaition in Meta-andesites at Dungash Area, Eastern Desert, Egypt. Resource Geology 51, 19–30. https://doi.org/10.1111/j.1751-3928.2001.tb00078.x

Heller Pearlshtien, D., Pignatti, S., Greisman-Ran, U., Ben-Dor, E., 2021. PRISMA sensor evaluation: a case study of mineral mapping performance over Makhtesh Ramon, Israel. International Journal of Remote Sensing 42, 5882–5914. https://doi.org/10.1080/01431161.2021.1931541

Henderson, G., Neuville, D., Downs, R., 2014. Spectroscopic Methods in Mineralogy and Material Sciences. Walter de Gruyter GmbH & Co KG.

Hensler, A.-S., Hagemann, S.G., Rosière, C.A., Angerer, T., Gilbert, S., 2015. Hydrothermal and metamorphic fluid-rock interaction associated with hypogene “hard” iron ore mineralisation in the Quadrilátero Ferrífero, Brazil: Implications

from in-situ laser ablation ICP-MS iron oxide chemistry. Ore Geology Reviews 69, 325–351. https://doi.org/10.1016/j.oregeorev.2015.02.023

Hensler, A.-S., Rosière, C.A., Hagemann, S.G., 2017. Iron Oxide Mineralization at the Contact Zone Between Phyllite and Itabirite of the Pau Branco Deposit, Quadrilátero Ferrífero, Brazil—Implications for Fluid-Rock Interaction During Iron Ore Formation. Economic Geology 112, 941–982. https://doi.org/10.2113/econgeo.112.4.941

Herz, N., 1978. Metamorphic Rocks of the Quadrilatero Ferrifero, Minas Gerais, Brazil. United States Geological Survey Professional Paper 641-C (1978), 81 pp.

Hey, M.H., 1954. A new review of the chlorites: Mineralogical Magazine, v. 30, 277–292.

Hitzman, M.W., Oreskes, N., and Einaudi, M.T., 1992, Geological characteristics and tectonic setting of proterozoic iron oxide (Cu – U – Au – REE) deposits: Precambrian research, 58, n. 1–4, 241–287.

Hitzman, M.W., Reynolds, N.A., Sangster, D.F., Allen, C.R., Carman, C.E., 2003. Classification, Genesis, and Exploration Guides for Nonsulfide Zinc Deposits. Economic Geology 98, 685–714. https://doi.org/10.2113/gsecongeo.98.4.685

Holden, D., Donegan, S., Pon, A., Dight, P.M., 2020. Brumadinho Dam InSAR study: analysis of TerraSAR-X, COSMO-SkyMed and Sentinel-1 images preceding the collapse. Presented at the Slope Stability 2020: 2020 International Symposium on Slope Stability in Open Pit Mining and Civil Engineering, 2020 12-14 May 2020, Online, Australian Centre for Geomechanics. https://doi.org/10.36487/ACG_repo/2025_15

Hosseinjani Zadeh, M., Tangestani, M.H., Roldan, F.V., Yusta, I., 2014. Sub-pixel mineral mapping of a porphyry copper belt using EO-1 Hyperion data. Advances in Space Research 53, 440–451. https://doi.org/10.1016/j.asr.2013.11.029

Hund, K., La Porta, D., Fabregas, T.P., Laing, T., Drexhage, J., 2020. Minerals for climate action: The mineral intensity of the clean energy transition. World Bank 73.

Hunt, G.R., 1971. Visible and near-infrared spectra of minerals and rocks: III. Oxides and hydro-oxides. Modern Geology 2, 195–205.

Hunt, G.R., 1977. Spectral signatures of particulate minerals in the visible and near infrared. Geophysics 42, 501–513. https://doi.org/10.1190/1.1440721

Hunt, G.R., Ashley, R.P., 1979. Spectra of altered rocks in the visible and near infrared. Economic Geology 74, 1613–1629. https://doi.org/10.2113/gsecongeo.74.7.1613

Hunt, G.R., Salisbury, J.W., 1971. Visible and near infrared spectra of minerals and rocks. II. Carbonates. Modern Geology 2, 23–30.

Irarrazaval, V., Sillitoe, R.H., Wilson, A.J., Toro, J.C., Robles, W., Lyall, G.D., 2010. Discovery History of a Giant, High-Grade, Hypogene Porphyry Copper-Molybdenum Deposit at Los Sulfatos, Los Bronces-Río Blanco District, Central Chile, in: Goldfarb, R.J., Marsh, E.E., Monecke, T. (Eds.), The Challenge of Finding New Mineral Resources: Global Metallogeny, Innovative Exploration, and New Discoveries. Society of Economic Geologists, https://doi.org/10.5382/SP.15.1.14

Ito, T., Morimoto, N., Sadanga, R., 1954. On the structure of Epidote: Acta Crystallographica, v. 7, 53-59.

Jambor, J.L., 1971. Wall rock alteration. The Canadian Mineralogist 11, 272–304.

Jenkins, D.M., Bozhilov, K.N., Ishida, K., 2003. Infrared and TEM characterization of amphiboles synthesized near the tremolite-pargasite join in the ternary system tremolite-pargasite-cummingtonite. American Mineralogist 88, 1104–1114. https://doi.org/10.2138/am-2003-0719

Jia, S., Jiang, S., Lin, Z., Li, N., Xu, M., Yu, S., 2021. A survey: Deep learning for hyperspectral image classification with few labeled samples. Neurocomputing 448, 179–204. https://doi.org/10.1016/j.neucom.2021.03.035

Kalanchey, R., Castillo, A. F., Weston, A. S., Oviedo, A. L., Guzman, C, Jo, M., 2020. NI 43 101 Technical Report. Preliminary economic assessment Marimaca Project Antofagasta, II Region, Chile.

Kale, K.V., Solankar, M.M., Nalawade, D.B., Dhumal, R.K., Gite, H.R., 2017. A Research Review on Hyperspectral Data Processing and Analysis Algorithms. Proc. Natl. Acad. Sci., India, Sect. A Phys. Sci. 87, 541–555. https://doi.org/10.1007/s40010-017-0433-y

Kasmaeeyazdi, S., Braga, R., Tinti, F., Mandanici, E., 2022. Mapping Bauxite Mining Residues Using Remote Sensing Techniques. Materials Proceedings 5, 91. https://doi.org/10.3390/materproc2021005091

Keshava, N., Mustard, J.F., 2002. Spectral unmixing. IEEE Signal Processing Magazine 19, 44–57. https://doi.org/10.1109/79.974727

Kissin, S. A., 1992. Five-element (Ni-Co-As-Ag-Bi) veins. Geoscience Canada, 19(3), 113-124.

Klein, C., Ladeira, E.A., 2000. Geochemistry and Petrology of Some Proterozoic Banded Iron-Formations of the Quadrilátero Ferrífero, Minas Gerais, Brazil. Economic Geology 95, 405–427. https://doi.org/10.2113/gsecongeo.95.2.405

Kokaly, R., Graham, G., Hoefen, T., Kelley, K., Johnson, M., Hubbard, B., Buchhorn, M., Prakash, A., 2017a. Multiscale Hyperspectral Imaging of the Orange Hill Porphyry Copper Deposit, Alaska, USA, with Laboratory-, Field-, and Aircraft-based Imaging Spectrometers, in Proc. Explor., 923–943.

Kokaly, R.F., Clark, R.N., Swayze, G.A., Livo, K.E., Hoefen, T.M., Pearson, N.C., Wise, R.A., Benzel, W.M., Lowers, H.A., Driscoll, R.L., Klein, A.J., 2017b. USGS Spectral Library Version 7 (USGS Numbered Series No. 1035), USGS Spectral Library Version 7, Data Series. U.S. Geological Survey Data Series 1035, 68 p., accessed January 21, 2022, at USGS Spectral Library Version 7 at http://pubs.er.usgs.gov/publication/ds1035.

Kramer, W., Siebel, W., Romer, R.L., Haase, G., Zimmer, M., Ehrlichmann, R., 2005. Geochemical and isotopic characteristics and evolution of the Jurassic volcanic arc between Arica (18 30′ S) and Tocopilla (22 S), North Chilean Coastal Cordillera. Geochemistry 65, 47–78.

Kreissl, S., Gerdes, A., Walter, B.F., Neumann, U., Wenzel, T., Markl, G., 2018. Reconstruction of a >200 Ma multi-stage “five element” Bi-Co-Ni-Fe-As-S system in the Penninic Alps, Switzerland. Ore Geology Reviews 95, 746–788. https://doi.org/10.1016/j.oregeorev.2018.02.008

Kruse, F.A., Perry, S.L., 2013. Mineral Mapping Using Simulated Worldview-3 Short-Wave-Infrared Imagery. Remote Sensing 5, 2688–2703. https://doi.org/10.3390/rs5062688

Kurz, T.H., Dewit, J., Buckley, S.J., Thurmond, J.B., Hunt, D.W., Swennen, R., 2012. Hyperspectral image analysis of different carbonate lithologies (limestone, karst and hydrothermal dolomites): the Pozalagua Quarry case study (Cantabria, North-west Spain). Sedimentology 59, 623–645. https://doi.org/10.1111/j.1365-3091.2011.01269.x

Ladino, M., Tomlinson, A., Blanco, N., 1997. Nuevos antecedentes para la edad de la deformación cretácica en Sierra de Moreno, II Región de Antofagasta, Norte de Chile. Presented at the VIII Congreso Geológico Chileno, Antofagasta, pp. 103–107.

Lampinen, H.M., Laukamp, C., Occhipinti, S.A., Hardy, L., 2019. Mineral footprints of the Paleoproterozoic sediment-hosted Abra Pb-Zn-Cu-Au deposit Capricorn Orogen, Western Australia. Ore Geology Reviews 104, 436–461. https://doi.org/10.1016/j.oregeorev.2018.11.004

Lampinen, H.M., Laukamp, C., Occhipinti, S.A., Metelka, V., Spinks, S.C., 2017. Delineating Alteration Footprints from Field and ASTER SWIR Spectra, Geochemistry, and Gamma-Ray Spectrometry above Regolith-Covered Base Metal Deposits—An Example from Abra, Western Australia☼. Economic Geology 112, 1977–2003. https://doi.org/10.5382/econgeo.2017.4537

Landsat Science [WWW Document], n.d. URL https://landsat.gsfc.nasa.gov/ (accessed 1.26.23).

Lang, J.R., Thompson, F., 2001. Alkalic porphyry Cu-Au deposits: Magmatic-hydrothermal mineralization with similarities to Fe-oxide-Cu-Au deposits [abs.].

Society of Economic Geology, Special Session, GSA abstracts with program, A3–A4.

Langer, K., Raith, M., 1974. Infrared spectra of Al-Fe (III)-epidotes and zoisites, Ca2 (Al1-p Fe^{3+} p) Al_2O (OH)[Si_2O_7] [SiO_4]. American Mineralogist: Journal of Earth and Planetary Materials 59, 1249–1258.

Lara, L., Godoy, E., 1998. Hoja Quebrada Salitrosa, Región de Atacama. Servicio nacional de geología y minería.

Larson, R.L., 1991. Geological consequences of superplumes. Geology 19, 963–966.

Latty, R.S., Nelson, R., Markham, B., Williams, D., Toll, D., 1985. Performance comparisons between information extraction techniques using variable spatial resolution data. Photogrammetric Engineering and Remote Sensing 51.

Laukamp, C., 2022. Geological Mapping using Mineral Absorption Feature-Guided Band-Ratios Applied to Prisma Satellite Hyperspectral Level 2D Imagery, in: IGARSS 2022 - 2022 IEEE International Geoscience and Remote Sensing Symposium. Presented at the IGARSS 2022 - 2022 IEEE International Geoscience and Remote Sensing Symposium, pp. 5981–5984. https://doi.org/10.1109/IGARSS46834.2022.9884015

Laukamp, C., Cudahy, T., Thomas, M., Jones, M., Cleverley, J.S., Oliver, N.H.S., 2011. Hydrothermal mineral alteration patterns in the Mount Isa Inlier revealed by airborne hyperspectral data. Australian Journal of Earth Sciences 58, 917–936. https://doi.org/10.1080/08120099.2011.571287

Laukamp, C., LeGras, M., Montenegro, V., Windle, S., McFarlane, A., 2022. Grandite-based resource characterization of the skarn-hosted Cu-Zn-Mo deposit of Antamina, Peru. Miner Deposita 57, 107–128. https://doi.org/10.1007/s00126-021-01047-2

Laukamp, C., Rodger, A., LeGras, M., Lampinen, H., Lau, I.C., Pejcic, B., Stromberg, J., Francis, N., Ramanaidou, E., 2021. Mineral Physicochemistry Underlying Feature-Based Extraction of Mineral Abundance and Composition from

Shortwave, Mid and Thermal Infrared Reflectance Spectra. Minerals 11, 347. https://doi.org/10.3390/min11040347

Laukamp, C., Termin, K.A., Pejcic, B., Haest, M., Cudahy, T., 2012. Vibrational spectroscopy of calcic amphiboles – applications for exploration and mining. European Journal of Mineralogy 24, 863–878. https://doi.org/10.1127/0935-1221/2012/0024-2218

Living Textbook | Atmospheric absorption and transmission | By ITC, University of Twente [WWW Document], n.d. URL https://ltb.itc.utwente.nl/498/concept/81484 (accessed 1.26.23).

Llaumett, C., Olcay, L., Marin, C., Marquardt, J.C., Reyes, E., 1975. El yacimiento de cobre porfídico" Andacollo", Provincia de Coquimbo, Chile.: Revista Geológica de Chile, (2): 56-66, 1975.

Locatelli, M., Federico, L., Agard, P., Verlaguet, A., 2019. Geology of the southern Monviso metaophiolite complex (W-Alps, Italy). Journal of Maps 15, 283–297. https://doi.org/10.1080/17445647.2019.1592030

Loizzo, R., Guarini, R., Longo, F., Scopa, T., Formaro, R., Facchinetti, C., Varacalli, G., 2018. Prisma: The Italian Hyperspectral Mission, in: IGARSS 2018 - 2018 IEEE International Geoscience and Remote Sensing Symposium. Presented at the IGARSS 2018 - 2018 IEEE International Geoscience and Remote Sensing Symposium, pp. 175–178. https://doi.org/10.1109/IGARSS.2018.8518512

LP DAAC - ASTER Overview [WWW Document], n.d. URL https://lpdaac.usgs.gov/data/get-started-data/collection-overview/missions/aster-overview/ (accessed 1.26.23).

Lüders, V., Romer, R.L., Cabral, A.R., Schmidt, C., Banks, D.A., Schneider, J., 2005. Genesis of itabirite-hosted Au–Pd–Pt-bearing hematite-(quartz) veins, Quadrilátero Ferrífero, Minas Gerais, Brazil: constraints from fluid inclusion infrared microthermometry, bulk crush-leach analysis and U–Pb systematics. Miner Deposita 40, 289–306. https://doi.org/10.1007/s00126-005-0024-8

Lypaczewski, P., Rivard, B., 2018. Estimating the Mg# and AlVI content of biotite and chlorite from shortwave infrared reflectance spectroscopy: Predictive equations and recommendations for their use. International Journal of Applied Earth Observation and Geoinformation 68, 116–126. https://doi.org/10.1016/j.jag.2018.02.003

Makreski, P., Jovanovski, G., Gajović, A., 2006. Minerals from Macedonia: XVII. Vibrational spectra of some common appearing amphiboles. Vibrational Spectroscopy 40, 98–109. https://doi.org/10.1016/j.vibspec.2005.07.006

Maksaev, V., Munizaga, F., McWilliams, M., Fanning, M., Mathur, R., Ruiz, J., Zentilli, M., 2004. New chronology for El Teniente, Chilean Andes, from U-Pb, 40Ar/39Ar, Re-Os, and fission-track dating: Implications for the evolution of a supergiant porphyry Cu-Mo deposit. Society of Economic Geologists 11, 15–54.

Malik, K., Robertson, C., Braun, D., Greig, C., 2021. U-Net convolutional neural network models for detecting and quantifying placer mining disturbances at watershed scales. International Journal of Applied Earth Observation and Geoinformation 104, 102510. https://doi.org/10.1016/j.jag.2021.102510

Malvern Panalytical | Analytical Instrumentation [WWW Document], n.d. URL https://www.malvernpanalytical.com/en (accessed 1.26.23).

Marimaca Copper Corp. 2023. Regulatory News. Available online: https://marimaca.com/regulatory-news/ (accessed on 23 January 2022).

Mars, J.C., Rowan, L.C., 2006. Regional mapping of phyllic- and argillic-altered rocks in the Zagros magmatic arc, Iran, using Advanced Spaceborne Thermal Emission and Reflection Radiometer (ASTER) data and logical operator algorithms. Geosphere 2, 161–186. https://doi.org/10.1130/GES00044.1

Marschik, R., Fontboté, L., 2001. The Candelaria-Punta del Cobre Iron Oxide Cu-Au(-Zn-Ag) Deposits, Chile. Economic Geology 96, 1799–1826. https://doi.org/10.2113/gsecongeo.96.8.1799

Marschik, R., Singer, B., Munizaga, F., Tassinari, C., Moritz, R., and Fontboté, L., 1997. Age of Cu (-Fe)-Au mineralization and thermal evolution of the Punta del Cobre district, Chile: Mineralium Deposita, v. 32, p. 531–546.

Mathian, M., Hebert, B., Baron, F., Petit, S., Lescuyer, J.-L., Furic, R., Beaufort, D., 2018. Identifying the phyllosilicate minerals of hypogene ore deposits in lateritic saprolites using the near-IR spectroscopy second derivative methodology. Journal of Geochemical Exploration 186, 298–314. https://doi.org/10.1016/j.gexplo.2017.11.019

Maureira, I., Barra, F., Reich, M., and Palma, G., 2022, Geology of the Altamira and Las Luces deposits, Coastal Cordillera, northern Chile: implications for the origin of stratabound Cu–(Ag) deposits: Mineralium Deposita, 1–24. https://doi.org/10.1007/s00126-022-01132-0

Maus, V., Giljum, S., Gutschlhofer, J., da Silva, D.M., Probst, M., Gass, S.L.B., Luckeneder, S., Lieber, M., McCallum, I., 2020. Global-scale mining polygons (Version 1). https://doi.org/10.1594/PANGAEA.910894

McCombe, D., Fernette, G., Aalawi, A., 1994. The geological and mineral resources of Yemen. Ministry of oil and Mineral Resources, Geological Survey of Yemen, Sana'a, Yemen.

McConachy, T.F., Yang, K., Boni, M., Evans, N.J., 2007. Spectral reflectance: preliminary data on a new technique with potential for non-sulphide base metal exploration. Geochemistry: Exploration, Environment, Analysis 7, 139–151. https://doi.org/10.1144/1467-7873/07-129

McLeod, R.L.; Gabell, A.R.; Green, A.A.; Gardavsky, V., 1987. Chlorite Infrared Spectral Data as Proximity Indicators of Volcanogenic Massive Sulphide Mineralisation; in Pacific Rim 87. International congress on the geology, structure, mineralisation and economics of Pacific Rim –, p. 321–324.

Meyer, J.M., Kokaly, R.F., Holley, E., 2022. Hyperspectral remote sensing of white mica: A review of imaging and point-based spectrometer studies for mineral

resources, with spectrometer design considerations. Remote Sensing of Environment 275, 113000. https://doi.org/10.1016/j.rse.2022.113000

Middleton, E.M., Campbell, P.K.E., Ong, L., Landis, D.R., Zhang, Q., Neigh, C.S., Huemmrich, K.F., Ungar, S.G., Mandl, D.J., Frye, S.W., Ly, V.T., Cappelaere, P.G., Chien, S.A., Franks, S., Pollack, N.H., 2017. Hyperion: The first global orbital spectrometer, earth observing-1 (EO-1) satellite (2000–2017), in: 2017 IEEE International Geoscience and Remote Sensing Symposium (IGARSS). Presented at the 2017 IEEE International Geoscience and Remote Sensing Symposium (IGARSS), pp. 3039–3042. https://doi.org/10.1109/IGARSS.2017.8127639

Mielke, C., Boesche, N.K., Rogass, C., Kaufmann, H., Gauert, C., De Wit, M., 2014. Spaceborne Mine Waste Mineralogy Monitoring in South Africa, Applications for Modern Push-Broom Missions: Hyperion/OLI and EnMAP/Sentinel-2. Remote Sensing 6, 6790–6816. https://doi.org/10.3390/rs6086790

Moenke, H.H.W., 1974. Vibrational Spectra and the Crystal-chemical Classification of Minerals, in: Farmer, V.C. (Ed.), The Infrared Spectra of Minerals. Mineralogical Society of Great Britain and Ireland, p. 0. https://doi.org/10.1180/mono-4.7

Mondillo, N., Boni, M., Balassone, G., Grist, B., 2011. In search of the lost zinc: A lesson from the Jabali (Yemen) nonsulfide zinc deposit. Journal of Geochemical Exploration 108, 209–219. https://doi.org/10.1016/j.gexplo.2011.02.010

Mondillo, N., Boni, M., Balassone, G., Joachimski, M., Mormone, A., 2014. The Jabali nonsulfide Zn–Pb–Ag deposit, western Yemen. Ore Geology Reviews 61, 248–267. https://doi.org/10.1016/j.oregeorev.2014.02.003

Monteiro, L.V., Xavier, R.P., de Carvalho, E.R., Hitzman, M.W., Johnson, C.A., de Souza Filho, C.R., Torresi, I., 2008. Spatial and temporal zoning of hydrothermal alteration and mineralization in the Sossego iron oxide–copper–gold deposit, Carajás Mineral Province, Brazil: paragenesis and stable isotope constraints. Mineralium Deposita 43, 129–159.

Montreuil, J.F., Corriveau, L., Grunsky, E.C., 2013. Compositional data analysis of hydrothermal alteration in IOCG systems, Great Bear magmatic zone, Canada: to

each alteration type its own geochemical signature. Geochemistry: Exploration, Environment, Analysis 13 (4), 229–247. https://doi.org/10.1144/geochem2011-101

Moroni, M., Rossetti, P., Naitza, S., Magnani, L., Ruggieri, G., Aquino, A., Tartarotti, P., Franklin, A., Ferrari, E., Castelli, D., Oggiano, G., Secchi, F., 2019. Factors Controlling Hydrothermal Nickel and Cobalt Mineralization—Some Suggestions from Historical Ore Deposits in Italy. Minerals 9, 429. https://doi.org/10.3390/min9070429

Morra, V., Secchi, F.A., Assorgia, A., 1994. Petrogenetic significance of peralkaline rocks from Cenozoic calc-alkaline volcanism from SW Sardinia, Italy. Chemical Geology 118, 109–142. https://doi.org/10.1016/0009-2541(94)90172-4

Mpodozis, C., and Ramos, V., 1990. The Andes of Chile and Argentina: Circum-Pacific Council for Energy and Mineral Resources Earth Science Series,v. 11, p. 59–90.

Munizaga, F., Huete, C., Hervé, F., 1985. Geocronología K-Ar y razones iniciales 87Sr/86Sr de la Franja Pacífica de Desarrollos Hidrotermales. Presented at the Proceedings IV Congreso Geológico Chileno, Antofagasta, p. 4.

Murray, H.H., Lyons, S.C., 1955. Correlation of Paper-Coating Quality with Degree of Crystal Perfection of Kaolinite. Clays Clay Miner. 4, 31–40. https://doi.org/10.1346/CCMN.1955.0040105

Mustard, J.F., 1992. Chemical analysis of actinolite from reflectance spectra. American Mineralogist 77, 345–358.

NASA JPL, 2013. NASA Shuttle Radar Topography Mission Global 1 arc second. https://doi.org/10.5067/MEASURES/SRTM/SRTMGL1.003

Niroumand-Jadidi, M., Bovolo, F., Bruzzone, L., 2020. Water Quality Retrieval from PRISMA Hyperspectral Images: First Experience in a Turbid Lake and Comparison with Sentinel-2. Remote Sensing 12, 3984. https://doi.org/10.3390/rs12233984

Noble, D.C., and McKee, E.H., 1999. The Miocene metallogenic belt of central and northern Peru: Society of Economic Geologists Special Publication 7, 155–193.

Norman, D.K., Parry, W.T., Bowman, J.R., 1991. Petrology and geochemistry of propylitic alteration at Southwest Tintic, Utah: Economic Geology, 86, 13–28.

Oliver, N.H., Cleverley, J.S., Mark, G., Pollard, P.J., Fu, B., Marshall, L.J., Rubenach, M.J., Williams, P.J., Baker, T., 2004. Modeling the role of sodic alteration in the genesis of iron oxide-copper-gold deposits, Eastern Mount Isa block, Australia. Economic Geology 99, 1145–1176.

Ossandón, C.G., Fréraut C, R., Gustafson, L.B., Lindsay, D.D., Zentilli, M., 2001. Geology of the Chuquicamata mine: A progress report. Economic Geology 96, 249–270.

Ostendorf, J., Henjes-Kunst, F., Mondillo, N., Boni, M., Schneider, J., Gutzmer, J., 2015. Formation of Mississippi Valley–type deposits linked to hydrocarbon generation in extensional tectonic settings: Evidence from the Jabali Zn-Pb-(Ag) deposit (Yemen). Geology 43, 1055–1058. https://doi.org/10.1130/G37112.1

Oviedo L., 2017. Technical report for the Marimaca Copper Project, Antofagasta Province, Region II, Chile: technical report prepared by NCL Ingeniería y Construcción SpA for Marimaca Copper Mining, effective date 24 February 2017, 99 p.

Oviedo, L., 2022: Updated Mineral Resource Estimation for the Marimaca Copper Project, Antofagasta Province, Region II, Chile: technical report prepared by NCL Ingeniería y Construcción SpA for Marimaca Copper Mining, effective date 26 November 2022, 217 p.

Pacey, A., Wilkinson, J. J., & Cooke, D. R., 2020. Chlorite and epidote mineral chemistry in porphyry ore systems: A case study of the Northparkes district, New South Wales, Australia. *Economic Geology*, *115*(4), 701-727.

Padilla-Garza, R.A., Titley, S.R., and Eastoe, C.J., 2004, Hypogene evolution of the Escondida porphyry copper deposit, Chile: Society of Economic Geologists Special Publication 11, p. 141–165.

Paoletti, M.E., Haut, J.M., Plaza, J., Plaza, A., 2018. A new deep convolutional neural network for fast hyperspectral image classification. ISPRS Journal of Photogrammetry and Remote Sensing, Deep Learning RS Data 145, 120–147. https://doi.org/10.1016/j.isprsjprs.2017.11.021

Paoletti, M.E., Haut, J.M., Plaza, J., Plaza, A., 2019. Deep learning classifiers for hyperspectral imaging: A review. ISPRS Journal of Photogrammetry and Remote Sensing 158, 279–317. https://doi.org/10.1016/j.isprsjprs.2019.09.006

Park, S.C., Park, M.K., Kang, M.G., 2003. Super-resolution image reconstruction: a technical overview. IEEE Signal Processing Magazine 20, 21–36. https://doi.org/10.1109/MSP.2003.1203207

Pasci S., Carmignani L., Pisanu G. & Sale V., 2015. Note Illustrative della Carta Geologica d'Italia alla scala 1:50.000, Foglio 564, Carbonia. APAT -Dipartimento Difesa del Suolo-Servizio Geologico d'Italia, 1-272, Roma.

Pepe, M., Pompilio, L., Gioli, B., Busetto, L., Boschetti, M., 2020. Detection and Classification of Non-Photosynthetic Vegetation from PRISMA Hyperspectral Data in Croplands. Remote Sensing 12, 3903. https://doi.org/10.3390/rs12233903

Perelló, J., Martini, R., Arcos, R., Muhr, R., 2003. Buey Muerto: porphyry copper mineralization in the Early Cretaceous arc of northern Chile. Presented at the Proceedings 10th Geol Congress, Chile, p. 203.

Perotto, A., Salino, C., Pognante, U., Genovese, G., Gosso, G., 1983. Assetto geologico-strutturale della falda piemontese nel settore dell'alta Valle di Viù (Alpi occidentali). Mem. Soc. Geol. Ital 26, 479–483.

Pettke, T., Diamond, L.W., Kramers, J.D., 2000. Mesothermal gold lodes in the north-western Alps : A review of genetic constraints from radiogenic isotopes. European Journal of Mineralogy 12, 213–230. https://doi.org/10.1127/0935-1221/2000/0012-0213

Pettorelli, N., Safi, K., Turner, W., 2014. Satellite remote sensing, biodiversity research and conservation of the future. Philosophical Transactions of the Royal

Society B: Biological Sciences 369, 20130190. https://doi.org/10.1098/rstb.2013.0190

Peyghambari, S., Zhang, Y., 2021. Hyperspectral remote sensing in lithological mapping, mineral exploration, and environmental geology: an updated review. JARS 15, 031501. https://doi.org/10.1117/1.JRS.15.031501

Piana, F., Fioraso, G., Irace, A., Mosca, P., d'Atri, A., Barale, L., Falletti, P., Monegato, G., Morelli, M., Tallone, S., Vigna, G.B., 2017. Geology of Piemonte region (NW Italy, Alps–Apennines interference zone). Journal of Maps 13, 395–405. https://doi.org/10.1080/17445647.2017.1316218

Pignatti, S., Palombo, A., Pascucci, S., Romano, F., Santini, F., Simoniello, T., Umberto, A., Vincenzo, C., Acito, N., Diani, M., Matteoli, S., Corsini, G., Casa, R., De Bonis, R., Laneve, G., Ananasso, C., 2013. The PRISMA hyperspectral mission: Science activities and opportunities for agriculture and land monitoring, in: 2013 IEEE International Geoscience and Remote Sensing Symposium - IGARSS. Presented at the 2013 IEEE International Geoscience and Remote Sensing Symposium - IGARSS, pp. 4558–4561. https://doi.org/10.1109/IGARSS.2013.6723850

Piquer, J., Skarmeta, J., Cooke, D.R., 2015. Structural Evolution of the Rio Blanco-Los Bronces District, Andes of Central Chile: Controls on Stratigraphy, Magmatism, and Mineralization. Economic Geology 110, 1995–2023. https://doi.org/10.2113/econgeo.110.8.1995

Pires, F., 1995. Textural and mineralogical variations during metamosphism of the proterozoic itabira iron formation in the quadrilatero Ferrifero, minas gerais, Brazil. Anais da Academia Brasileira de Ciências 67, 77–106.

Pollard, P.J., 2000. Evidence of a magmatic fluid and metal source for Fe oxide Cu-Au mineralization. Hydrothermal iron oxide copper-gold and related deposits: A global perspective 1, 27–41.

Post, J.L., Noble, P.N., 1993. The Near-Infrared Combination Band Frequencies of Dioctahedral Smectites, Micas, and Illites. Clays Clay Miner. 41, 639–644. https://doi.org/10.1346/CCMN.1993.0410601

Pouchou, J. L., Pichoir, F., & Newbury, D. E., 1988. A simplified version of the "PAP" model for matrix corrections in EPMA. Microbeam analysis, 315-318.

Pour, A.B., Hashim, M., 2012. The application of ASTER remote sensing data to porphyry copper and epithermal gold deposits. Ore Geology Reviews 44, 1–9. https://doi.org/10.1016/j.oregeorev.2011.09.009

PRISMA data portal, n.d. Available online: https://prisma.asi.it/.

Price, P., 1953. Wall-rock alteration in northwestern Quebec: Geological Society of America Bulletin, v. 64, p. 1464

Quang, C.X., Clark, A.H., W. Lee, J.K., Hawkes, N., 2005. Response of supergene processes to episodic Cenozoic uplift, pediment erosion, and ignimbrite eruption in the porphyry copper province of southern Peru. Economic Geology 100, 87–114.

Ramírez, L.E., Palacios, C., Townley, B., Parada, M., Sial, A., Fernandez-Turiel, J., Gimeno, D., Garcia-Valles, M., Lehmann, B., 2006. The Mantos Blancos copper deposit: an upper Jurassic breccia-style hydrothermal system in the Coastal Range of Northern Chile. Mineralium Deposita 41, 246–258.

Renger, F.E., Noce, C.M., Romano, A.W., Machado, N., 1994. Evolução sedimentar do supergrupo minas: 500 ma. De registro geológico no Quadrilátero Ferrífero, Minas Gerais, Brasil. Geonomos. https://doi.org/10.18285/geonomos.v2i1.227

Rhodes, A.L., Oreskes, N., and Sheets, S., 1999. Geology and rare earth element geochemistry of magnetite deposits at El Laco, Chile: Society of Economic Geologists Special Publication, 7, 299–332.

Ricardo, V.R., Gustafson, L.B., Vukasovic, M., Enrique, T.F., and Skewes, M.A., 1999. Ore Breccias in the Rio Blanco-Los Bronces Porphyry Copper Deposit, Chile, in Skinner, B.J. ed., Geology and Ore Deposits of the Central Andes: Society of Economic Geologists, p. 0.

Richards, J.P., 2009. Postsubduction porphyry Cu-Au and epithermal Au deposits: Products of remelting of subduction-modified lithosphere. Geology 37, 247–250. https://doi.org/10.1130/G25451A.1

Richards, J.P., Mumin, H., 2013. Magmatic-hydrothermal processes within an evolving Earth: Iron oxide-copper-gold and porphyry Cu Mo Au deposits. Geology 41, 767–770. https://doi.org/10.1130/G34275.1

Ridley, J., 2013. Ore Deposit Geology. Cambridge University Press.

Riley, D., Cudahy, T., Hewson, R., Jansing, D., Hackwell, J., 2007. SEBASS imaging for copper porphyry and skarn deposits, Yerington, NV. Presented at the Proceedings of exploration.

Rodger, A., Fabris, A., Laukamp, C., 2021. Feature Extraction and Clustering of Hyperspectral Drill Core Measurements to Assess Potential Lithological and Alteration Boundaries. Minerals 11, 136. https://doi.org/10.3390/min11020136

Romaniello, V., Buongiorno, M.F., Spinetti, C., Silvestri, M., 2022. Analysis of Volcanic Carbon Dioxide Emissions by Means of Prisma Hyperspectral Data and in Situ Measurements, in: IGARSS 2022 - 2022 IEEE International Geoscience and Remote Sensing Symposium. Presented at the IGARSS 2022 - 2022 IEEE International Geoscience and Remote Sensing Symposium, pp. 7268–7271. https://doi.org/10.1109/IGARSS46834.2022.9884650

Romaniello, V., Spinetti, C., Silvestri, M., Buongiorno, M.F., 2021. A Methodology for CO_2 Retrieval Applied to Hyperspectral PRISMA Data. Remote Sensing 13, 4502. https://doi.org/10.3390/rs13224502

Ronneberger, O., Fischer, P., Brox, T., 2015. U-Net: Convolutional Networks for Biomedical Image Segmentation. https://doi.org/10.48550/arXiv.1505.04597

Rosière, C.A., Chemale, F., 1996. Genesis of banded iron-formations; discussion. Economic Geology 91, 466–468. https://doi.org/10.2113/gsecongeo.91.2.466

Rosière, C.A., Spier, C.A., Rios, F.J., Suckau, V.E., 2008. The Itabirites of the Quádrilátero Ferrífero and Related High-Grade Iron Ore Deposits: An Overview. https://doi.org/10.5382/Rev.15.09

Rossi, M., Gattiglia, A., 2013. Terre rosse, pietre verdi e blu cobalto: miniere a Usseglio: seconda raccolta di studi. Museo civico alpino" Arnaldo Tazzetti.

Rowland, M., Clark, A.H., 2001. Temporal overlap of supergene alteration and high-sulfidation mineralization in the Spence porphyry copper deposit, II Región, Chile [abs.]. Presented at the Geological Society of America, Abstracts with Programs, p. A-358.

Sabins, F.F., 1999. Remote sensing for mineral exploration. Ore Geology Reviews 14, 157–183. https://doi.org/10.1016/S0169-1368(99)00007-4

Salehi, T., Tangestani, M.H., 2020. Per-pixel analysis of ASTER data for porphyry copper hydrothermal alteration mapping: A case study of NE Isfahan, Iran. Remote Sensing Applications: Society and Environment 20, 100377. https://doi.org/10.1016/j.rsase.2020.100377

Sanches, I.D., Filho, C.R.S., Kokaly, R., 2014. Spectroscopic remote sensing of plant stress at leaf and canopy levels using the chlorophyll 680 nm absorption feature with continuum removal. https://doi.org/10.1016/J.ISPRSJPRS.2014.08.015

Santoro, L., Putzolu, F., Mondillo, N., Herrington, R., Najorka, J., Boni, M., Dosbaba, M., Maczurad, M., Balassone, G., 2021. Quantitative mineralogical evaluation of Ni-Co laterite ores through XRPD-QPA- and automated SEM-based approaches: The Wingellina (Western Australia) case study. Journal of Geochemical Exploration 223, 106695. https://doi.org/10.1016/j.gexplo.2020.106695

Santoro, L., Rollinson, G.K., Boni, M., Mondillo, N., 2015. Automated Scanning Electron Microscopy (QEMSCAN®)-based mineral identification and quantification of the Jabali Zn-Pb-Ag nonsulfide deposit (Yemen). Economic Geology 110, 1083–1099. https://doi.org/10.2113/econgeo.110.4.1083

Sarker, Y., Fahim, S.R., Hosen, Md.S., Sarker, S.K., Mondal, Md.N.I., Das, S.K., 2020. Regularized Singular Value Decomposition Based Multidimensional Convolutional Neural Network for Hyperspectral Image Classification, in: 2020 IEEE Region 10 Symposium (TENSYMP). Presented at the 2020 IEEE Region 10 Symposium (TENSYMP), pp. 1502–1505. https://doi.org/10.1109/TENSYMP50017.2020.9230701

Savitzky, A., Golay, M.J.E., 1964. Smoothing and Differentiation of Data by Simplified Least Squares Procedures. Anal. Chem. 36, 1627–1639. https://doi.org/10.1021/ac60214a047

Scharrer, M., Kreissl, S., Markl, G., 2019. The mineralogical variability of hydrothermal native element-arsenide (five-element) associations and the role of physicochemical and kinetic factors concerning sulfur and arsenic. Ore Geology Reviews 113, 103025. https://doi.org/10.1016/j.oregeorev.2019.103025

Scheinost, A.C., Schulze, D.G., Schwertmann, U., 1999. Diffuse reflectance spectra of A1 substituted goethite: a ligand field approach. Clays and Clay Minerals 47, 156–164.

Scheuber, E., Andriessen, P.A., 1990. The kinematic and geodynamic significance of the Atacama fault zone, northern Chile. Journal of Structural Geology 12, 243–257.

Scott, K.M. and Yang, K., 1997 Spectral Reflectance Studies of White Micas; CSIRO Report 439R AMIRA Project P435; CSIRO: Canberra, Australia, 35 p.

Sekandari, M., Masoumi, I., Beiranvand Pour, A., M Muslim, A., Rahmani, O., Hashim, M., Zoheir, B., Pradhan, B., Misra, A., Aminpour, S.M., 2020. Application of Landsat-8, Sentinel-2, ASTER and WorldView-3 Spectral Imagery for Exploration of Carbonate-Hosted Pb-Zn Deposits in the Central Iranian Terrane (CIT). Remote Sensing 12, 1239. https://doi.org/10.3390/rs12081239

Serrano, L., Vargas, R., Stambuk, V., Aguilar, C., Galeb, M., Holmgren, C., Contreras, A., Godoy, S., Vela, I., Skewes, M., 1998. The late Miocene to early Pliocene Río Blanco-Los Bronces copper deposit, central Chilean Andes: Society of Economic Geologists Special Publication 5, p. 119–130.

Sharma, V.K., Azad, R.K., Chowdary, V.M., Jha, C.S., 2022. Delineation of Frequently Flooded Areas Using Remote Sensing: A Case Study in Part of Indo-Gangetic Basin, in: Pandey, A., Chowdary, V.M., Behera, M.D., Singh, V.P. (Eds.), Geospatial Technologies for Land and Water Resources Management, Water Science and Technology Library. Springer International Publishing, Cham, pp. 505–530. https://doi.org/10.1007/978-3-030-90479-1_27

Shaw, G.A., Burke, H.K., 2003. Spectral Imaging for Remote Sensing 14.

Sherman, D.M., Waite, T.D., 1985. Electronic spectra of Fe3+ oxides and oxide hydroxides in the near IR to near UV. American Mineralogist 70, 1262–1269.

Sillitoe, R.H., 2003. Iron oxide-copper-gold deposits: an Andean view. Miner Deposita 38, 787–812. https://doi.org/10.1007/s00126-003-0379-7

Sillitoe, R.H., 1972. A Plate Tectonic Model for the Origin of Porphyry Copper Deposits. Economic Geology 67, 184–197. https://doi.org/10.2113/gsecongeo.67.2.184

Sillitoe, R.H., 1988. Epochs of intrusion-related copper mineralization in the Andes. Journal of South American Earth Sciences 1, 89–108. https://doi.org/10.1016/0895-9811(88)90018-1

Sillitoe, R.H., 2010. Porphyry Copper Systems. Economic Geology 105, 3–41. https://doi.org/10.2113/gsecongeo.105.1.3

Sillitoe, R.H., Jaramillo, L., Damon, P.E., Shafiqullah, M., Escovar, R., 1982. Setting, characteristics, and age of the Andean porphyry copper belt in Colombia. Economic Geology 77, 1837–1850.

Sillitoe, R.H., McKee, E.H., 1996. Age of supergene oxidation and enrichment in the Chilean porphyry copper province. Economic Geology 91, 164–179.

Sillitoe, R.H., Perelló, J., 2005. Andean Copper Province: Tectonomagmatic Settings, Deposit Types, Metallogeny, Exploration, and Discovery, in: Hedenquist, J.W., Thompson, J.F.H., Goldfarb, R.J., Richards, J.P. (Eds.), One Hundredth

Anniversary Volume. Society of Economic Geologists, p. 0. https://doi.org/10.5382/AV100.26

Sillitoe, R.H., Porter, T., 1998. Major regional factors favouring large size, high hypogene grade, elevated gold content and supergene oxidation and enrichment of porphyry copper deposits. Porphyry and hydrothermal copper and gold deposits: A global perspective: Adelaide, Australian Mineral Foundation 21–34.

Silva Rotta, L.H., Alcântara, E., Park, E., Negri, R.G., Lin, Y.N., Bernardo, N., Mendes, T.S.G., Souza Filho, C.R., 2020. The 2019 Brumadinho tailings dam collapse: Possible cause and impacts of the worst human and environmental disaster in Brazil. International Journal of Applied Earth Observation and Geoinformation 90, 102119. https://doi.org/10.1016/j.jag.2020.102119

Sonntag, I., Laukamp, C., Hagemann, S.G., 2012. Low potassium hydrothermal alteration in low sulfidation epithermal systems as detected by IRS and XRD: An example from the Co–O mine, Eastern Mindanao, Philippines. Ore Geology Reviews, Primary Geochemical Characteristics of Mineral Deposits: Implications for Exploration 45, 47–60. https://doi.org/10.1016/j.oregeorev.2011.08.001

Souza, A.H. de, Krüger, F.L. von, Araújo, F.G. da S., Mendes, J.J., 2021. Mineralogical Characterization Applied to Iron Ore Tailings from the Desliming Stage with Emphasis on Quantitative Electron Microscopy (QEM). Mat. Res. 24. https://doi.org/10.1590/1980-5373-MR-2019-0677

Spatz, D., 1996. Remote Sensing Strategies for Mineral Exploration and Development. International Archives of Photogrammetry and Remote Sensing 31, 638–649.

Spier, C.A., de Oliveira, S.M.B., Rosière, C.A., 2003. Geology and geochemistry of the Águas Claras and Pico Iron Mines, Quadrilátero Ferrífero, Minas Gerais, Brazil. Miner Deposita 38, 751–774. https://doi.org/10.1007/s00126-003-0371-2

Stern, C., Skewes, M., 2003. Generation of giant Miocene and Pliocene copper deposits in Central Chile: Role of ridge subduction, decreased subduction angle, increased subduction erosion, crustal thickening, and mafic and adakite-like dacitic

magma within long-lived, batholith size, open system magma chambers. Presented at the X Congreso Geológico Chileno, Actas CD, Concepción.

Stuart, B.H., 2004. Infrared Spectroscopy: Fundamentals and Applications. John Wiley & Sons.

Sunshine, J.M., Pieters, C.M., Pratt, S.F., 1990. Deconvolution of mineral absorption bands: An improved approach. Journal of Geophysical Research: Solid Earth 95, 6955–6966. https://doi.org/10.1029/JB095iB05p06955

Syifa, M., Park, S.J., Achmad, A.R., Lee, C.-W., Eom, J., 2019. Flood Mapping Using Remote Sensing Imagery and Artificial Intelligence Techniques: A Case Study in Brumadinho, Brazil. Journal of Coastal Research 90, 197–204. https://doi.org/10.2112/SI90-024.1

Tangestani, M., Moore, F., 2002. Porphyry copper alteration mapping at the Meiduk area, Iran. International Journal of Remote Sensing 23, 4815–4825.

Tappert, M.C., Rivard, B., Giles, D., Tappert, R., Mauger, A., 2013. The mineral chemistry, near-infrared, and mid-infrared reflectance spectroscopy of phengite from the Olympic Dam IOCG deposit, South Australia. Ore Geology Reviews 53, 26–38. https://doi.org/10.1016/j.oregeorev.2012.12.006

Taranik, J.V., and Aslett, Z.L., 2009. Development of Hyperspectral Imaging for Mineral Exploration, in Bedell, R., Crósta, A.P., and Grunsky, E. eds., Remote Sensing and Spectral Geology: Society of Economic Geologists, p. 0.

Tarquini, S., Isola, I., Favalli, M., Mazzarini, F., Bisson, M., Pareschi, M.T., Boschi, E., 2007. TINITALY/01: a new Triangular Irregular Network of Italy.

Taylor, R., 2011. Gossans and Leached Cappings: Field Assessment: Springer Science & Business Media, 165 p.

Tempfli, K., Huurneman, G.C., Bakker, W.H., Janssen, L.L.F., Feringa, W.F., Gieske, A.S.M., Grabmaier, K.A., Hecker, C.A., Horn, J.A., Kerle, N., Meer, F.D. van der, Parodi, G.N., Pohl, C., Reeves, C.V., Ruitenbeek, F.J.A. van, Schetselaar, E.M., Weir, M.J.C., Westinga, E., Woldai, T., 2009. Principles of remote sensing: an

introductory textbook. International Institute for Geo-Information Science and Earth Observation.

The Spectral Geologist [WWW Document], n.d.. The Spectral Geologist. URL https://research.csiro.au/thespectralgeologist/ (accessed 1.26.23).

Thiele, S.T., Lorenz, S., Kirsch, M., Cecilia Contreras Acosta, I., Tusa, L., Herrmann, E., Möckel, R., Gloaguen, R., 2021. Multi-scale, multi-sensor data integration for automated 3-D geological mapping. Ore Geology Reviews 136, 104252. https://doi.org/10.1016/j.oregeorev.2021.104252

Thompson, A.J.B., Scott, K., Huntington, J., and Yang, K., 2009a, Mapping Mineralogy with Reflectance Spectroscopy: Examples from Volcanogenic Massive Sulfide Deposits, in Bedell, R., Crósta, A.P., and Grunsky, E. eds., Remote Sensing and Spectral Geology: Society of Economic Geologists, p. 0.

Thompson, A.J.B., (SEG 1990), Hauff, P.L., and Robitaille, A.J., 2009b, Alteration Mapping in Exploration: Application of Short-Wave Infrared (SWIR) Spectroscopy, in Bedell, R., Crósta, A.P., and Grunsky, E. eds., Remote Sensing and Spectral Geology: Society of Economic Geologists, p. 0.

Thompson, F., de Oliveira, B.C., Cordeiro, M.C., Masi, B.P., Rangel, T.P., Paz, P., Freitas, T., Lopes, G., Silva, B.S., S. Cabral, A., Soares, M., Lacerda, D., dos Santos Vergilio, C., Lopes-Ferreira, M., Lima, C., Thompson, C., de Rezende, C.E., 2020. Severe impacts of the Brumadinho dam failure (Minas Gerais, Brazil) on the water quality of the Paraopeba River. Science of The Total Environment 705, 135914. https://doi.org/10.1016/j.scitotenv.2019.135914

Toro, J.C., Ortúzar, J., Zamorano, J., Cuadra, P., Hermosilla, J., Spröhnle, C., 2012. Protracted Magmatic-Hydrothermal History of the Río Blanco-Los Bronces District, Central Chile: Development of World's Greatest Known Concentration of Copper, in: Hedenquist, J.W., Harris, M., Camus, F. (Eds.), Geology and Genesis of Major Copper Deposits and Districts of the World: A Tribute to Richard H. Sillitoe. Society of Economic Geologists, p. 0. https://doi.org/10.5382/SP.16.05

Tuddenham, W.M., Lyon, R.J.P., 1959. Relation of Infrared Spectra and Chemical Analysis for Some Chlorites and Related Minerals. Anal. Chem. 31, 377–380. https://doi.org/10.1021/ac60147a014

U.S. Geological Survey, 2020. Mineral commodity summaries 2020: U.S. Geological Survey, 200 p. https://doi.org/10.3133/mcs2020

Vaccaro, A., 2017. Il telerilevamento iperspettrale: messa a punto e calibrazione di una camera iperspettrale: Master Thesis. https://doi.org/10.13140/RG.2.2.32558.41288

van der Meer, F.D., 1995. Spectral reflectance of carbonate mineral mixtures and bidirectional reflectance theory: Quantitative analysis techniques for application in remote sensing. Remote Sensing Reviews 13, 67–94. https://doi.org/10.1080/02757259509532297

van der Meer, F.D., 2004. Analysis of spectral absorption features in hyperspectral imagery. Int j appl earth obs 5, 55–68. Https://doi.org/10.1016/j.jag.2003.09.001

van der Meer, F.D., van der Werff, H.M.A., van Ruitenbeek, F.J.A., Hecker, C.A., Bakker, W.H., Noomen, M.F., van der Meijde, M., Carranza, E.J.M., Smeth, J.B. de, Woldai, T., 2012. Multi- and hyperspectral geologic remote sensing: A review. International Journal of Applied Earth Observation and Geoinformation 14, 112–128. https://doi.org/10.1016/j.jag.2011.08.002

van der Meer F.D., van der Werff, H.M.A., van Ruitenbeek, F.J.A., 2014. Potential of ESA's Sentinel-2 for geological applications. Remote sensing of environment 148, 124–133. https://doi.org/10.1016/j.rse.2014.03.022

van der Werff, H.M.A., Van der Meer, F. D.., 2015. Sentinel-2 for Mapping Iron Absorption Feature Parameters. Remote Sensing 7, 12635–12653. https://doi.org/10.3390/rs71012635

van Ruitenbeek, F.J.A., Cudahy, T., Hale, M., van der Meer, F.D., 2005. Tracing fluid pathways in fossil hydrothermal systems with near-infrared spectroscopy. Geology 33, 597–600. https://doi.org/10.1130/G21375.1

Vangi, E., D'Amico, G., Francini, S., Giannetti, F., Lasserre, B., Marchetti, M., Chirici, G., 2021. The New Hyperspectral Satellite PRISMA: Imagery for Forest Types Discrimination. Sensors 21, 1182. https://doi.org/10.3390/s21041182

Vedder, W., 1964. Correlations between infrared spectrum and chemical composition of mica. American Mineralogist 49, 736–768.

Vedder, W. & McDonald, R.S., 1963. Vibrations of the OH Ions in Muscovite. J. Chem. Phys. 38, 1583–1590. https://doi.org/10.1063/1.1776925

Velde, B., 1965. Phengite micas; synthesis, stability, and natural occurrence. American Journal of Science 263, 886–913.

Vergilio, C. Dos S., Lacerda, D., Oliveira, B.C.V. de, Sartori, E., Campos, G.M., Pereira, A.L. de S., Aguiar, D.B. de, Souza, T. Da S., Almeida, M.G. de, Thompson, F., Rezende, C.E. de, 2020. Metal concentrations and biological effects from one of the largest mining disasters in the world (Brumadinho, Minas Gerais, Brazil). Sci Rep 10, 5936. https://doi.org/10.1038/s41598-020-62700-w

Vidal, C.E., Injoque-Espinoza, J., Sidder, G.B., Mukasa, S.B., 1990. Amphibolitic Cu-Fe skarn deposits in the central coast of Peru. Economic Geology 85, 1447–1461. https://doi.org/10.2113/gsecongeo.85.7.1447

Vila, T., Richard, Z., Lindsay, N., 1998. Geology of the Manto Verde Copper Deposit, northern Chile: A specularite-rich, hydrothermal-tectonic breccia related to the Atacama fault zone: in Camus, F., Sillitoe, R. M., & Petersen, R., 1996). Andean copper deposits: New discoveries, mineralization, styles and metallogeny (No. 5). Society of Economic Geologists.

Vincent, R.K., Hunt, G.R., 1968. Infrared Reflectance from Mat Surfaces. Appl. Opt., AO 7, 53–59. https://doi.org/10.1364/AO.7.000053

Walther, J.V., Woodland, A.B., 1993. Experimental determination and interpretation of the solubility of the assemblage microcline, muscovite, and quartz in supercritical H_2O. Geochimica et cosmochimica acta 57, 2431–2437.

Wambugu, N., Chen, Y., Xiao, Z., Tan, K., Wei, M., Liu, X., Li, J., 2021. Hyperspectral image classification on insufficient-sample and feature learning using deep neural networks: A review. International Journal of Applied Earth Observation and Geoinformation 105, 102603. https://doi.org/10.1016/j.jag.2021.102603

Wang, R., Cudahy, T., Laukamp, C., Walshe, J.L., Bath, A., Mei, Y., Young, C., Roache, T.J., Jenkins, A., Roberts, M., Barker, A., Laird, J., 2017. White Mica as a Hyperspectral Tool in Exploration for the Sunrise Dam and Kanowna Belle Gold Deposits, Western Australia*. Economic Geology 112, 1153–1176. https://doi.org/10.5382/econgeo.2017.4505

Warnaars, F.W., Holmgren D, C., Barassi F, S., 1985. Porphyry copper and tourmaline breccias at Los Bronces-Rio Blanco, Chile. Economic Geology 80, 1544–1565.

White, A.J.R., Laukamp, C., Stokes, M.A., Legras, M., Pejcic, B., 2017. Vibrational spectroscopy of epidote, pumpellyite and prehnite applied to low-grade regional metabasites. GEEA 17, 315–333. https://doi.org/10.1144/geochem2016-007

Whitney, D.L., Evans, B.W., 2010. Abbreviations for names of rock-forming minerals. American Mineralogist 95, 185–187. https://doi.org/10.2138/am.2010.3371

Williams, Patrick J., Barton, M.D., Johnson, D.A., Fontboté, L., Haller, A. de, Mark, G., Oliver, N.H.S., Marschik, R., 2005. Iron Oxide Copper-Gold Deposits: Geology, Space-Time Distribution, and Possible Modes of Origin: in Hedenquist, J. W., Thompson, J. F., Goldfarb, R. J., & Richards, J. P. (2005). One Hundredth Anniversary Volume. https://doi.org/10.5382/AV100.13

Wilson, N., Zentilli, M., Reynolds, P., Boric, R., 2003. Age of mineralization by basinal fluids at the El Soldado manto-type copper deposit, Chile: 40Ar/39Ar geochronology of K-feldspar. Chemical Geology 197, 161–176.

Wokaun, A., 1996. B. Schrader: Infrared and Raman Spectroscopy - Methods and Applications. VCH, Weinheim, 1995, DM 298, -, ISBN 3-527-26446-9. Berichte der Bunsengesellschaft für physikalische Chemie 100, 1268–1268. https://doi.org/10.1002/bbpc.19961000733

Wong, S.C., Gatt, A., Stamatescu, V., McDonnell, M.D., 2016. Understanding Data Augmentation for Classification: When to Warp?, in: 2016 International Conference on Digital Image Computing: Techniques and Applications (DICTA). Presented at the 2016 International Conference on Digital Image Computing: Techniques and Applications (DICTA), pp. 1–6. https://doi.org/10.1109/DICTA.2016.7797091

Wu, J., Yan, W., Ni, W., Bian, H., 2013. Feature extraction for hyperspectral data based on MNF and singular value decomposition, in 2013 IEEE International Geoscience and Remote Sensing Symposium - IGARSS. Presented at the 2013 IEEE International Geoscience and Remote Sensing Symposium - IGARSS, pp. 1430–1433. https://doi.org/10.1109/IGARSS.2013.6723053

Yan, D., Zhang, H., Li, G., Li, X., Lei, H., Lu, K., Zhang, L., Zhu, F., 2022. Improved Method to Detect the Tailings Ponds from Multispectral Remote Sensing Images Based on Faster R-CNN and Transfer Learning. Remote Sensing 14, 103. https://doi.org/10.3390/rs14010103

Yang, K., Browne, P.R.L., Huntington, J.F., Walshe, J.L., 2001. Characterising the hydrothermal alteration of the Broadlands–Ohaaki geothermal system, New Zealand, using short-wave infrared spectroscopy. Journal of Volcanology and Geothermal Research 106, 53–65. https://doi.org/10.1016/S0377-0273(00)00264-X

Youssef, E.S.A.A., 1998. Sequence stratigraphy of the upper jurassic evaporite-carbonate: Sequence at the western area of Wadi Al-Jawf-Marib basin, Yemen. Carbonates Evaporites 13, 168–173. https://doi.org/10.1007/BF03176590

Zaini, N., van der Meer, F.D., van der Werff, H.M.A., 2012. Effect of Grain Size and Mineral Mixing on Carbonate Absorption Features in the SWIR and TIR Wavelength Regions. Remote Sensing 4, 987–1003. https://doi.org/10.3390/rs4040987

Zhang, T., Yi, G., Li, H., Wang, Z., Tang, J., Zhong, K., Li, Y., Wang, Q., Bie, X., 2016. Integrating Data of ASTER and Landsat-8 OLI (AO) for Hydrothermal Alteration Mineral Mapping in Duolong Porphyry Cu-Au Deposit, Tibetan Plateau, China. Remote Sensing 8, 890. https://doi.org/10.3390/rs8110890

Zucchetti, S., 1979. Remarks on the nickel deposits of the Western Alps (Italy). Presented at the Proceedings of the 3rd International Symposium on the Mineral Deposits of the Alps (ISMIDA), Loeben, pp. 355–360.

Data access

The project was carried out using PRISMA Products, © of the Italian Space Agency (ASI), delivered under an ASI License to use by visiting prisma.asi.it ("PRISMA data portal").

Acknowledgments

This work was supported by the Ph.D. scholarship Complementary Operational Program (POC) "Research and Innovation 2014–2020", co-financed by the Italian Ministry of University and Research and European Social Fund (ESF) 2014–2020, Project Supervisor: Prof. Nicola Mondillo. Scientific partners of the Project: CSIRO Mineral Resources and the British Geological Survey (BGS).

First and foremost, I would like to express my sincere gratitude to my supervisor, Prof. Nicola Mondillo, who has supported me throughout this project. His guidance and expertise have been invaluable, and I could not have completed this project without his help. His guidance over the last three years made me grow from personal, academic, and scientific points of view.

I thank Prof. Maria Boni for believing in me and for pushing me to pursue this path. Without her guidance, I would have never achieved these results. I am also so grateful to have had Dr. Carsten Laukamp, Prof. Giuseppina Balassone, Prof. Diego di Martire, and Dr. Alessandro Novellino, as co-tutors. Their feedback and encouragement have made all the difference, and I am so grateful for their support. I cannot forget Prof. Matteo Massironi and Dr. Sabrina Ferrari, as well as the Geoscience Department of the University of Padova. I thank them for warmly hosting me and guiding me to acquire further knowledge in the field of hyperspectral imaging.

I also thank the entire staff of the Department of Earth, Environmental and Resources Sciences (DiSTAR, Università degli studi di Napoli Federico II), mainly Prof. Domenico Calcaterra, as former Head of the Department of Earth, Environmental and Resources Sciences (DiSTAR), Prof. Vincenzo Morra e Prof. Rosa Di Maio, as former and present P.hD. coordinators, and Dr. Roberto De Gennaro and Dr. Sergio

Bravi for their work. I thank the Natural History Museum (NHM) of London, first and foremost, Dr. Francesco Putzolu and Dr. Jens Najorka, for their help, suggestions, and advice, and Prof. Richard Herrington for hosting me at the NHM.

I am grateful to the entire present and past team at AltaMin Ltd., Simone Zanin, Giulia Domenighini, Geraint Harris, Erika Belotti, Stefania Tiraboschi, Clara Raieri, Marcello De Angelis, and the whole Edilmac drillers team at the Gorno Zinc Project and the Oltre il Colle community. I am also thankful to C.U.G.R.I. (Consortium between the Federico II University of Naples and the University of Salerno for the Prediction and Prevention of Major Hazards) for supporting this research with hardware/software facilities. I would like to thank the Italian Space Agency (ASI) for having funded the PRISMA mission and for releasing free-of-charge hyperspectral images to the scientific community.

Dr. Cristian Carli (INAF – IAPS) and Dr. Licia Santoro (University of Turin) are also thanked for their careful evaluation and review of this Thesis. I also want to acknowledge all the reviews and editors who evaluated the papers published in the frame of this thesis.

I thank all my Ph.D. colleagues and friends, among others Rita, Anna, Filippo, Simone, Ilaria, Martina, Pietro, Antonio, Daniele, Giulia, all the present and past Ph.D. students of the "Ph.D. room 4.61" and of the XXXV and following cycles. I am grateful to the BeGEO scientists' association team, Rita, Antonio, Lorenzo, Ciro, Salvatore, Alessandro, Andrea B., Maria, Andrea I., Barbara, Felice, and Claudio, for the experiences and the hard work we shared, for the goals we achieved, and for the future that awaits us. I thank Cristian most sincerely for his love, for believing in me, for supporting me at every moment, even on the not-so-good days, for the moments we've shared, for being my "team" and for the life that awaits us. I am also so grateful to have had my family, Papà, Mamma, Sara, Marcella, and Vis, by my side every day. I will be grateful forever to my mother, Angela, and my father, Rosario, for having taught me so much and for having transmitted their principles to me: humility, sense of duty, and love, which guide me every day.